Optical Design for an Open Access Trapped Ion Quantum Processor

by

Nikolay Videnov

A thesis
presented to the University of Waterloo
in fulfillment of the
thesis requirement for the degree of
Master of Science
in
Physics (Quantum Information)

Waterloo, Ontario, Canada, 2021

Author's Declaration

I hereby declare that I am the sole author of this thesis. This is a true copy of the thesis, including any required final revisions, as accepted by my examiners.

I understand that my thesis may be made electronically available to the public.

Abstract

The future of quantum information is scaling to a ever larger number of qubits. Doing so will require advances in the approach for all aspects of current experimental systems. The QuantumION project is a large step in this direction. This project will provide an open-access trapped ion quantum processor for the research community. The necessary innovations for how QuantumION will be controlled and assembled represents a paradigm shift from ad-hock disparate systems running the experiment to a well engineered, integrated, quantum platform. These innovations will require coordinated work from many contributors, and this thesis covers a few specific aspects of QuantumION to which the author has contributed.

In this thesis laser cooling is numerically investigated with special attention paid to external heating rates, laser linewidths, power limitations, and laser direction. Considering all these imperfections a set of laser parameters are presented for both quenched resolved sideband cooling and electromagnetically induced transparency cooling that in concert will cool all motional modes to the ground state. A novel individual addressing (IA) scheme is presented with detailed simulation showing $< 10^{-5}$ intensity cross talk and the first attempt at realizing this IA scheme is presented. The design philosophy for opto-mechanical assemblies in QuantumION is discussed and an example assembly is walked through the design process.

Acknowledgements

Firstly I would like to thank my committee members for taking the time to review and preside over my thesis work: Professor Thomas Jennewein, Professor Hamed Majedi, and Professor Kyung Soo Choi. With a special heartfelt thank you to Prof. Majedi for discussing my PhD career path and offering support and kindness at a time of uncertainty for me.

The chapter on laser cooling was a particular challenge for me being a theoretical investigation so I would like to acknowledge Chung-You Shih for writing the initial time dependent code which served as a skeleton and template for my original code. Yi Hong Teoh who wrote the TrICal package which has been incredibly useful for our group. Professor Crystal Senko who jointly supervises the QuantumION project with Professor Rajibul; Thank you for running a course in trapped ion quantum computing, as a professor making the time for superfluous teaching is difficult and my understanding of the theory would be greatly diminished in the absence of this tutelage.

Throughout my degree Dr. Matthew Day has been a mentor to me. I am always impressed with his knowledge and his ability to balance work and life, something I'm hoping to emulate as we work together on my PhD project. As well thanks to the members of QuantumION: Noah Greenberg, Richard Rademacher, Ali Binai-Motlagh, Dr. Mahmood Sabooni, Dr. Virginia Frey, and Elijah Durso-Sabina for engaging conversations, design input, and being the medium in which QuantumION is built.

I would also like to acknowledge the COOP students I've had the joy of "playing" mentor to, it has given me a new appreciation of what it is like to be on the other side of the COOP experience, and they have all made impactful contributions to the final system. Chronologically they are Rachel DiTommaso, Nathan Snider, Mark Elliott Wallace, and Stephen Del Grosso Milek.

Finally someone with an outsized contribution to my development as a researcher and to this thesis is Professor Rajibul. I have had the pleasure of working with him through the setup of two labs: first as a COOP student for three terms helping build up the Quantum Information with Trapped Ions (QITI) lab, and again building up the QuantumION lab for my MSc. degree. I knew early on in my BSc. that I wanted to work in a Quantum Information lab, so I applied to a COOP position with Prof. Rajibul and did not make the first cut. I persisted by talking to Prof. Crystal Senko about a job placement and was again rebuffed. Entering the end of the term with only the prospect of a night shift monitoring hospital Roombas. I noticed that Prof. Rajibul's job posting had not been closed despite being late in the term. Having resigned to the night shift I send Prof. Rajibul a direct email asking if he was still searching for a student, and was overjoyed to receive an interview the same day. The accepted candidate had reconsidered and Prof. Rajibul took a chance on a persistent, somewhat unqualified, undergraduate. This series of events and the ensuing years of research has shaped my career, my experience, and my view of self. For this I'm truly grateful and can't thank my persistence and Prof. Rajibul's oversight enough.

Dedication

Foremost to my parents who's love, care, and support have made me.

На баба Диди и дядо Борис за незабравимото детство на Трапето. На леля Гека за всеотдайната подкрепа, както и за стажа в БАН, който ми помогна да си избера посока. На баба Нели и дядо Софрони, чийто път като инженери следвам. И на всички останали скъпи за мен хора в България и Австрия.

To Jill with my love.

Table of Contents

List of Figures

List of Tables

Chapter 1

Introduction

Trapped ions are a leading platform for quantum computing, with experiments demonstrating fully programmable 11 qubit computers[1], partially programmable 53 qubit quantum simulators[2], and a host of interesting single qubit sensing applications.[3] One advantageous feature which makes trapped ions a leading platform is long coherence times.[4][5] These are long coherence times even relative to the gate times, and better gate performance is still being pursued as an active area of research. Recent results have demonstrated high fidelity gates[6], and improvements in gate times.[7] This gives the trapped ion system a large gate volume, and the efficiency of each gate is aided by the fully connected interaction graph. Due to the long range Coulomb force arbitrary pairs of ions can be entangled in a single operation[1] which can be harnessed for speedup relative to only nearest neighbour interactions.[8][9]

More broadly quantum information is a worthwhile research direction for two reasons: it's a platform for investigating physics, and a host of near-term useful applications are within grasp. Knowledge for it's own sake is a pure motivation and what has driven many discoveries and paradigm shifts. However someone has to keep the lights on. Quantum information strikes a nice balance, and the prospect of performing classically difficult computations efficiently has applications to developing novel pharmaceuticals[10], optimizing logistics[11], and cryptography.[12][13] Atomic clocks have re-defined the way time is measured and sit at the heart of the GPS system ubiquitous in the modern interconnected world.[14] So quantum information is a test-bed both for human knowledge and for near term improvement in quality of life. For these reasons pushing quantum technology research towards greater understanding and greater availability is a worthwhile pursuit and should be carried out with great vigor.

[1]Within reason. For 20 ions this is true however there is drop-off in interaction strength and for a sufficiently long ion chain this claim is modified.

1.1 Thesis Outline

The remainder of this chapter is dedicated to providing a primer on quantum computing with trapped ions. The basic Hamiltonians which govern the system are derived and discussed. The construction of the QuantumION project and where it differs from a typical ion trap experiment are then discussed.

Chapter 2 motivates the need for cooling the trapped ions to near motional ground state. Doppler cooling as the first stage in two-step cooling is discussed with the limitations of this techniques setting the stage for sub-Doppler methods. Two techniques for reaching the ground state are investigated at length. External heating sources and laser linewidths specific to the Sandia trap and QuantumION lasers are factored into finding ideal cooling parameters for both techniques.

The next chapter discusses the challenges of individually controlling the quantum state of each ion in a chain using addressing lasers. These challenges are overcome using a unique guided light individual addressing system (GLIAS). This system makes use of a custom micro-lens array (MLA) and the considerations leading to this approach as well as it's implementation are covered.

Methods of building out opto-mechanical assemblies in accordance with the demands of the QuantumION system are discussed in Chapter 4. The design philosophy is applied to an example pegboard and initial results are discussed.

Finally Chapter 5 summarizes the thesis and discusses outstanding work for this project.

1.2 Quantum Computing with Trapped Ions

This section provides an introduction to the trapped ion quantum system. This background information will be particularly useful for understanding Chapter 2. The first subsection discusses the trapped ion system in the absence of any interaction with external fields. To perform interesting experiments the ions must interact with some external forces. Therefore the next section discusses the interaction Hamiltonian between a trapped ion and a laser.

1.2.1 The Trapped Ion Hamiltonian

Atoms are a collection of protons, neutrons, and electrons. With hydrogen being comprised of the fewest components and so the simplest. A remarkably accurate model of the hydrogen

atom can be made by considering an electron in a 3D confining Coulomb potential, and this model can be tackled analytically![15] An ion is an atom which does not have the same number of electrons as it does protons which gives it a net charge. Ionizing is most easily achieved by removing a valence electron through photo-ionization, where a laser is used to excite one of the valence electrons out of the confining potential. Ionizing hydrogen this way would give you just a proton, and that system does not have the convenient hydrogen-like energy structure so it's not a good candidate for trapped ion quantum computing. Instead an atomic species is chosen which when singly ionized has a hydrogen-like energy structure. Most easily achieved by taking an alkaline earth metal (group 2) species, which have 2 valence electrons, and ejecting one of the electrons. Since the valence shell is at a higher energy than the occupied orbitals, and all shells below are closed, this system is now hydrogen-like.[2]

The energy levels below the valence shell are occupied by the remaining electrons and as a fermion the valence electron can't fall below the valence shell, instead all the manipulations of the electron are between different excited energy levels above the valence shell. The nearest available excited energy levels are typically drawn as the right portion of Figure 1.1 shows. The Rutherford-Bohr model is shown to the left for pedagogical purposes.

There are a host of useful numbers also listed in the diagram. The vertical axis is a not-to-scale representation of energy where the $S_{1/2}$ level is taken to be the ground state, above it are all higher energy levels with the energy spacing between levels defined by the wavelength of light needed to bridge the energy gap. This is useful for ion trappers because laser color is an in-lab distinction with a convenient scale. The "green laser" is more intuitive to say than the "563THz laser". Every excited energy level has a lifetime listed above it. Since excited energy levels in atomic systems spontaneously emit photons and decay to lower energy levels the rate at which decays occur has an associated time constant, and this is the lifetime of the energy level. The $D_{3/2}$ and $D_{5/2}$ are deemed metastable because their lifetime is so long that in experimental timescales the decay can be ignored. The lifetime is also inversely proportional to the line-width of that energy level. Spontaneous decay is subject to some selection rules which determine to which energy levels decay is permitted, and even for allowed decay paths the likely-hood of going one way or the other is not uniform. So the percentage on the figure indicates what percent of the decay from the excited state goes which way. Finally each energy level has a label in spectroscopic notation, basically a compact notation borrowed from the spectroscopy community which indicates all the quantum number information of that level (See Appendix A).

[2]In addition to this story there are some features which are critical for *serious* experiments, top among them are a closed-loop cooling transition for laser cooling and F=0, F=1 hyperfine levels in the ground state for use as qubit energy levels.

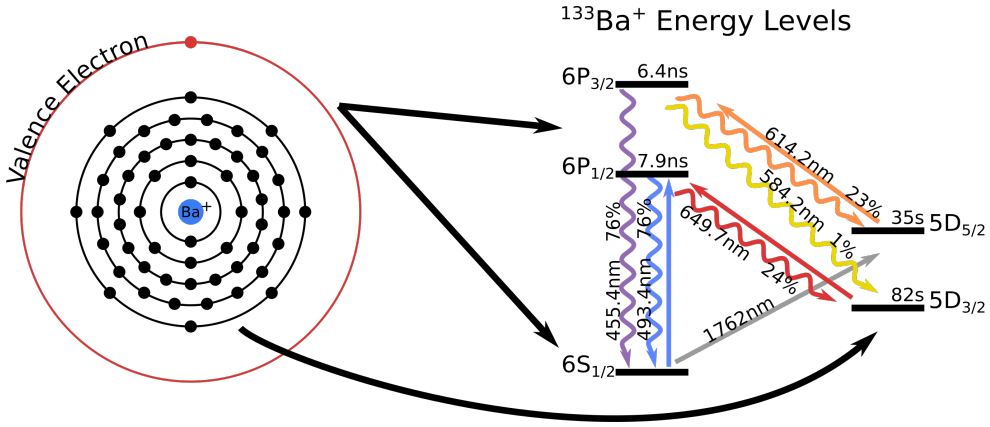

Figure 1.1: On the left there is the Rutherford-Bohr model of an atom. This model essentially shows just the principle quantum number and how many electrons can fit into each principle quantum number. The diagram is illustrative but not technically correct since all the n=6 energy levels would be in the valence level and the $D_{3/2}$ and $D_{5/2}$ levels are below the valence level. There's a reason this model fell out of favour! On the right is the typical method of drawing the atomic energy levels, all the occupied levels are omitted and only the available (excited) energy levels are depicted.

Because the depicted energy levels are occupied by the electron they are called the electronic energy levels and for identical ion species and isotopes all ions will have identical electronic Hamiltonians. Keep in mind that each ion has it's own set of electronic levels so for a chain of n ions there will be n copies of the atomic Hamiltonian. See:

$$H_e = \sum_n \sum_i E_i \left|i\right\rangle\!\left\langle i\right| = \sum_n \frac{E_q}{2}(\left|n,e\right\rangle\!\left\langle n,e\right| - \left|n,g\right\rangle\!\left\langle n,g\right|) = \sum_n \frac{\hbar\omega_q}{2}\sigma_z^{(n)} \tag{1.1}$$

with the most prevalent simplification of the electronic Hamiltonian into a qubit also shown. If the ion chain is being used as a chain of qubits in a gate model of quantum computing then only the two levels being designated as spin-up and spin-down are relevant, and the remainder can be omitted from the Hamiltonian. These two levels are separated by a qubit frequency (ω_q) and can even be written with the Pauli operator formalism. Note that the electronic levels of adjacent qubits do not interact and so the Pauli operators for different qubits commute.

The trapped ions are not flying through space unabated though, they are trapped in a potential, hence the name. This is a benefit of using ions over atoms, that they interact with electric fields strongly through the Coulomb force and so can be "trapped". The

trapping potential is approximated as a harmonic confining potential which brings in the second part of the unperturbed trapped ion Hamiltonian—the harmonic oscillator:

$$H_m = \sum_k^{3n} \hbar\omega_k (a_k^\dagger a_k + 1/2) \tag{1.2}$$

This again is a well studied problem of a particle confined in a harmonic well and so all the familiar ladder operators make an appearance.[15] For a single ion in a 1D potential there is a single quantum harmonic oscillator (HO) with frequency ω_{trap}. However ions are trapped in a 3D confining potential[3] so for a single ion there are three harmonic oscillators each with a characteristic frequency. For n ions each of them are confined in three dimensions so there are 3n harmonic oscillators, again each with their own characteristic frequency. The trapping parameters are chosen to have these systems be non-degenerate.

Since the motion of one ion affects the motion of the others through the Coulomb force, the ion motion is written in terms of collective motional modes for the whole chain.[16] The operators for one motional mode commute with those for another and with the Pauli operators, but critically all ions see all motional modes. The coupling strength to the motional modes is dependent on how much displacement a given mode induces on a given ion. For an idea of the frequency range and structure of these motional mode frequencies see Appendix C.

The full trapped ion Hamiltonian is the combination of these two well studied systems,

$$H_{bare} = \sum_n \frac{\hbar\omega_q}{2}\sigma_z^{(n)} + \sum_k^{3n} \hbar\omega_k (a_k^\dagger a_k + 1/2) \tag{1.3}$$

Where the sum over n is a sum over n ions, and the sum over k is a sum over the 3 confining directions for the n ions. It's interesting how much depth can be added simply by combining the two systems.

1.2.2 The Interaction Hamiltonian

The previous section was in the absence of any perturbations to the ion system. Since the ions are in vacuum it's very difficult to get at them with a screwdriver and instead lasers are used for nearly every function needed in a trapped ion experiment.[4] The laser field will

[3] A time averaged 3D confining potential not in violation of Earnshaw's theorem.

[4] Transitions with far-field microwaves work largely the same way but can only drive carrier transitions. Near-field microwave transitions are somewhat different.[17]

interact with the ion and the interaction Hamiltonian is engineered to drive the trapped ion system through laser cooling, quantum gates, state readout, and most every thing else.

The laser field will couple pairs of energy levels. To determine which pairs "see" the laser, the ion is written as a multi-pole expansion and the interaction between the laser and a dipole, quadrupole, octupole, etc., can separately be investigated. The interaction strength drops off rapidly as higher poles are considered so for typical configurations only the first contributing term is considered. This is the distinction between dipole-allowed transitions, ones which have a non-zero dipole term, and dipole-forbidden terms which must have their quadrupole term considered.[18]

For this derivation only the dipole term is considered and the energy levels which are coupled by the dipole operator are taken as a given. The interaction term is then written as the dot product of the dipole operator and the electric field,

$$H_I = \hat{r}_d \cdot \vec{E} = \hat{r}_d \cdot \vec{E}_0 \cos\left(\vec{k} \cdot \vec{r} - \omega t + \phi\right) \tag{1.4}$$

Where $\hat{r}_d$ is the dipole operator and $\vec{E}$ is the electric field. A plane wave is assumed, which is accurate at the focus of a beam over the spatial extent of an ion. The wave propagates along the k vector ($\vec{k}$) direction and is evaluated at the ion position, $\vec{r}$. The light oscillates with angular frequency ω and ϕ is the laser phase. For a dipole-allowed two level system this can be simplified to[19]

$$H_I = \Omega \sigma_x \cos\left(\vec{k} \cdot \vec{r} - \omega t + \phi\right). \tag{1.5}$$

where σ_x is a Pauli operator and Ω is the Rabi-rate, the rate at which oscillations from ground state to excited state occur when the laser is tuned directly on frequency, defined as

$$\Omega = \frac{e|E|}{\hbar}\sqrt{\frac{5A_{ge}^{E1}\lambda^3}{64\pi^3 c\alpha}} \tag{1.6}$$

All the constants follow their usual definition and A_{ge}^{E1} is the Einstein-A coefficient for the specific transition.[16]

Since Chapter 2 is explicitly concerned with the geometric constraints on laser beam direction the derivation is carried through without assuming a laser direction. Typically the laser is implicitly assumed to be in the trap direction which makes calculations neater. The bare Hamiltonian can the be written as

$$H_0 = \frac{\hbar\omega_q}{2}\sigma_z + \sum_d^{x,y,z} \hbar\omega_{trap}^d (a_d^\dagger a_d + 1/2) \tag{1.7}$$

where σ_z is the standard Pauli operator, ω_{trap} is the trap frequency, and $a^\dagger$, a are the standard ladder operators for the HO. $\hbar$ has been set to 1 for convenience. The first step is to move to the interaction picture,

$$\begin{aligned} H_I &= e^{iH_0 t}\,\Omega\sigma_x \cos\left(\vec{k}\cdot\vec{r} - \omega t + \phi\right) e^{-iH_0 t} \\ &= \Omega\Big(e^{i\omega_q\sigma_z t}\sigma_x e^{-i\omega_q\sigma_z t}\Big)\Big(e^{i\sum_d a_d^\dagger a_d \omega_{trap}^d}\,\cos\left(\vec{k}\cdot\vec{r} - \omega t + \phi\right) e^{-i\sum_d a_d^\dagger a_d\omega_{trap}^d}\Big) \\ &= \frac{\Omega}{2}\Big(\sigma^+ e^{i\omega_q t} + \sigma^- e^{-i\omega_q t}\Big)\Big(e^{i\sum_d k_d \hat{R}_d(t)} e^{i(\phi-\omega t)} + e^{-i\sum_d k_d\hat{R}_d(t)} e^{-i(\phi-\omega t)}\Big) \end{aligned} \tag{1.8}$$

where in the interaction picture the $\hat{r}$ vector becomes a generalized position operator. In the position agnostic derivation this is just $\hat{X}(t) = X_0(ae^{-i\omega_{trap}t} + a^\dagger e^{i\omega_{trap}t})$, the position operator in the Heisenberg picture, but keeping the laser direction information produces three position operators for the three directions.

$$k_d\hat{R}_d(t) = k_d R_0^d(a_d e^{-i\omega_d t} + a_d^\dagger e^{i\omega_d t}) = \eta_d(a_d e^{-i\omega_d t} + a_d^\dagger e^{i\omega_d t}) \tag{1.9}$$

It is also convenient at this point to define the Lamb-Dickie (LD) parameter,

$$\eta_d = \vec{k}\cdot\hat{e}_d R_0^d = \cos\theta\left|\vec{k}\right|\sqrt{\frac{\hbar}{2m\omega_d}} \tag{1.10}$$

which is the ratio of the spatial extent of the ion over the wavelength of the interacting laser.

The product of the spin and motional parts of Equation 1.8 produces terms at the sum and difference of the qubit frequency and the laser frequency. By taking a rotating wave approximation (RWA) only the terms at the difference between the laser and qubit frequency are left, with the rest averaging out and being omitted.

$$\begin{aligned} H_I &= \frac{\Omega}{2}\Big(\sigma^+ e^{\sum_d ik_d\hat{R}_d(t)} e^{i(\phi-\delta t)} + H.c\Big) \\ H_I &= \frac{\Omega}{2}\Big(\sigma^+ e^{i(\phi-\delta t)}\prod_d (e^{ik_d\hat{R}_d(t)}) + H.c\Big) \end{aligned} \tag{1.11}$$

Define δ=$\omega_q - \omega$ the difference between the qubit and laser frequency. $H.c$ indicates that there is the Hermitian conjugate of the previous term in the Hamiltonian as well.

Since the ion is well localized, especially after undergoing cooling, the Lamb-Dickie (LD) parameter is small and the motional mode exponential can be expanded as a Taylor series to first order in the LD parameter. If the ion species is too light, or the temperature

is high, then the LD parameters would not be small enough to take the approximation to first order. In this case higher order terms are needed which would result in $n \pm 2, 3, \ldots$ sidebands being possible. Similarly if the LD parameter is too small, like in the case of microwave radiation, then terms even to first order in the LD parameter would not significantly contribute to the system.

The result of this approximation is

$$\begin{aligned} H_I &= \frac{\Omega}{2}\Big(\sigma^+ e^{i(\phi-\delta t)} \prod_d (1 + i\eta_d(a_d e^{-i\omega_d t} + a_d^\dagger e^{i\omega_d t})) + H.c\Big) \\ H_I &= \frac{\Omega}{2}\Big(\sigma^+ e^{i(\phi-\delta t)} (1 + \sum_d i\eta_d(a_d e^{-i\omega_d t} + a_d^\dagger e^{i\omega_d t})) + H.c\Big) \end{aligned} \tag{1.12}$$

When considering that the laser direction is not well specified there are three expansions. Multiplying out these three expansions will produce mostly terms to second and higher order in the LD parameter. These higher order terms are omitted.

There are three cases where applying another RWA produces a useful result. First with no detuning (δ=0) the laser is on resonance with the bare transition and off resonance from any motional modes. A RWA then eliminates all η terms and gives the interaction Hamiltonian for a carrier transition.

$$H_c = \frac{\Omega}{2}(\sigma^+ e^{i\phi} + \sigma^- e^{-i\phi}) \tag{1.13}$$

Alternatively the laser detuning can be equated to $\pm\omega_{\{x,y,z\}}$ in which case an application of the RWA will remove the carrier Hamiltonian and instead produce a Hamiltonian which couples the spin and motional modes.

$$\begin{aligned} H_{rsb} &= \cos\theta \frac{\Omega\eta_d}{2}(a\sigma^+ e^{i\phi} + a^\dagger \sigma^- e^{-i\phi}) \\ H_{bsb} &= \cos\theta \frac{\Omega\eta_d}{2}(a^\dagger\sigma^+ e^{i\phi} + a\sigma^- e^{-i\phi}) \end{aligned} \tag{1.14}$$

The two types of sideband transition are then revealed with the red sideband exciting the spin and removing a quanta of motion, while the blue sideband excites the spin and adds a quanta of motion. Critically notice that this RWA also removes the excess directions, only the motional mode which the laser is tuned to will see the laser and undergo sideband transitions.

The conclusion of painstakingly carrying the laser direction through the calculations can be see as only modifying the value of η by the overlap between the laser direction

and the trap direction. Since the Rabi-rate for driving sideband transitions is scaled by η effectively the overlap between the trap and laser modifies how strongly sidebands can be driven. This valuable information is used in Chapter 2. As well it's notable that the carrier transition is not modified by the laser direction because it does not see the trap direction. If moving the laser relative to the magnetic field changes the selection rules for the transition however this is accounted for in the dipole or quadrupole operator and will also modify the Rabi-rate.

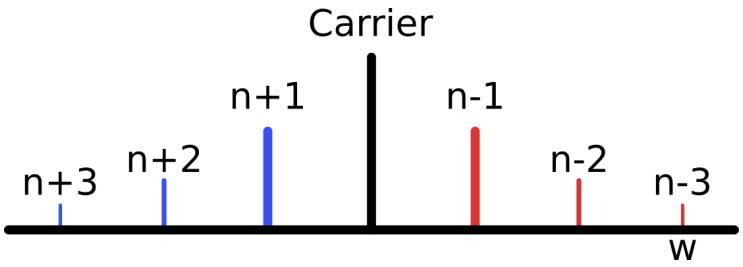

(a) Frequency space plot showing the three key types of transitions. There are carrier transitions directly at the transition frequency. These do not change the HO state when absorbing a photon. To the left (right) there are the blue (red) sidebands which represent a heating (cooling) transition. While there are $n \pm 2, 3, \ldots, j$ transitions available, their strength of being driven scales as η^j which means in the Lamb-Dickie regime only ± 1 and carrier transitions contribute significantly.

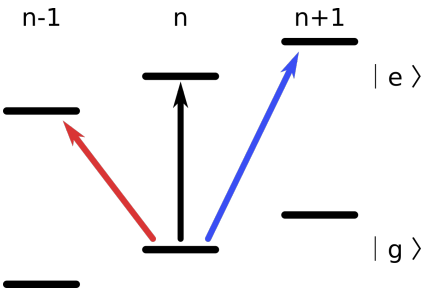

(b) Ladder diagram showing the effect carrier and sideband transitions have. The horizontal axis is the harmonic oscillator energy levels, and the vertical axis is electronic levels.

Figure 1.2

1.2.3 Putting it Together

So far it's been established that trapped ions have a number of internal electronic states and harmonic oscillator states. The electronic states can be manipulated by applying laser pulses with controlled phase, frequency, and intensity. Crucially the interaction Hamiltonian also describes how addressing the electronic states can be used to interact with the harmonic oscillator states. This will be important when considering laser cooling in Section 2, but how are these concepts utilized for quantum information?

A gate model of quantum computing can be straightforwardly realized with just the tools previously discussed. First a pair of electronic energy levels are designated as spin up

and spin down. For instance the hyperfine levels in the $S_{1/2}$ manifold are most commonly used. State preparation is done by optical pumping into the ground state.[20] Single quibt gates are done by controlling the phase of the laser and driving carrier transitions.[5] Following the classic paper by Cirac and Zoller entangling operations can be created.[21] The insight in this paper is to use the sideband Hamiltonian to transfer the spin state of the control qubit into a harmonic oscillator excitation, ie. if the system is spin down then a blue sideband transition will excite a quanta of motion, if it's spin up then the system is unaffected. Then this quanta can be used to flip the spin of a target qubit dependent on the HO state. The true procedure is a little more complicated but the concept is to use the harmonic oscillator to mediate a spin dependent flip of the target qubit based on the control qubit with the insight that in the ground state the HO allows spin dependent sideband transitions.

With a single entangling operation and the full compliment of single qubit rotations any quantum computation can be done. This method has the complication that the HO must be entirely in the ground state which is difficult and short-lived in the presence of external heating rates. More sophisticated methods of entangling qubits have been developed.[22] However the idea of the HO as a quantum bus persists in these approaches.

State readout of the ion chain is done by performing state dependent fluorescence similar to the optical pumping scheme. Simply put a laser is used to drive carrier transitions on a short-lived excited state from which spontaneous decay re-emits photons that are collected onto a camera. The trick is picking a set of energy levels where the spin up population fluoresces and the spin down population does not due to appropriate selection rules.

1.3 QuantumION

Separate from the trapped ion platform there has been a steady increase in interest for quantum computing with a commensurate increase in the potential applications of quantum computers. Many of these applications can be verified on Noisy Intermediate-Scale Quantum (NISQ) processors and this drives a demand for experimental validation.[23] Due to the prohibitive cost and man-power of building a NISQ processor cloud based quantum computing has emerged as an economical and low risk alternative.

QuantumION is a project which is jointly supervised by professors Crystal Senko and Rajibul Islam. This project aims to address the growing demand by providing an open-access quantum processor based on the trapped ion platform. While there have been a

[5] For the hyperfine levels Raman transitions are used.

handful of cloud based quantum computing platforms made available, to date they are all privately funded and operated. Thus researchers are not given access to the hardware level of these devices without a lengthy non-disclosure agreement (NDA) process. This is because most prospects of future profits for these firms are tied to their intellectual property—and so they cannot make their designs freely available.

In this aspect QuantumION is a first, with the aim of providing full design files to the public. This is only possible due to the public funding provided by TQT through the Canada First Research Excellence Fund. To make full use of the design files a user of QuantumION should also be allowed to control the full hardware stack. Building a control system capable of such a feat is a challenge in it's own right and this is one of two main areas of active research in QuantumION. For the progress the QuantumION team has made in this regard see Frey *et al.* which demonstrates the unique full-stack quantum experiment description language developed for QuantumION.[24] The other being the opto-mechanical design of the QuantumION system. These two problems are strongly coupled as the optical system must account for all the needed controls, and the electrical system should be able to integrate all these controls. Designing for such an application imposes some additional challenges which need to be addressed. These are summarized below.

- **Open-access:** Full system design in made freely available and any person can submit experiments to QuantumION without completing an NDA or lengthy back-and-forth. Their submitted experiment will be queued and autonomously executed.
- **High-availability:** Stemming from open-access to have a useful machine it must be operational 24-7, with very limited down time for maintenance. This means heavy control system integration and that graduate students can't be poking their heads in every morning to tune mirrors!
- **Utility:** The team building QuantumION is not in a position to say what controls users will or won't want to use. One person's bad gate is another's PhD dissertation.[6] Thus the goal is to let users decide for themselves what controls are useful and the design team's goal is to build in as many controls as feasible.

1.3.1 Major Systems

The QuantumION experimental setup in broad strokes is not too different from a typical ion trapping experiment. There is a central vacuum chamber which must be pumped

[6] Credit to Richard Rademacher who coined this phrase and has repeatedly used it as a cudgel to keep the design teams in line with this philosophy.

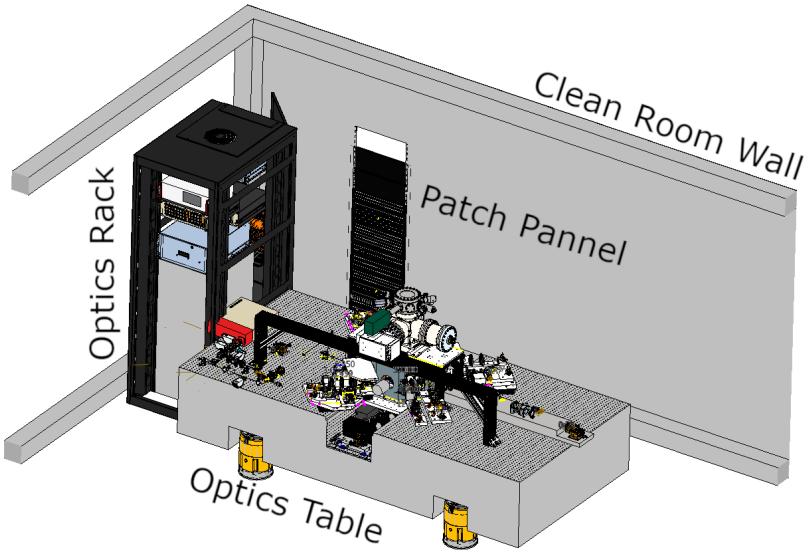

Figure 1.3: Render of the QuantumION experiment room.

to ultra-high vacuum (UHV) to suppress collisions between the ions and gas molecules. The Vacuum chamber sits on a custom Newport optics table which has been modified to include a slot down the center of the table for housing the ion fluorescence collection optics. Surrounding the vacuum chamber there is an urban sprawl of optics for beam shaping and delivering the half dozen wavelengths needed for trapped ion experiments. The optics are housed on optical "pegboards" the design philosophy of which is described in Chapter 4. These pegboards primarily receive light from optical fibres which in turn are supplied light from an adjacent high-rise—the optics rack—which houses in standard rack drawers laser heads, laser controllers, and a handful of other items which must be as close as possible to the optics table. All of this is contained within a modular clean room manufactured by ESC. Lining the outside wall of the clean room are the multiple electronics racks needed for controlling the experiment. A patch panel approach has been implemented allowing easy insertion of test or monitoring equipment between electronics racks, clean room, optics rack, and optics table.

Sandia HOA 2.0

A difference of providence between typical trapped ion setups and the QuantumION configuration is the use of a Sandia HOA 2.0 chip-trap instead of a "classical" Paul trap or

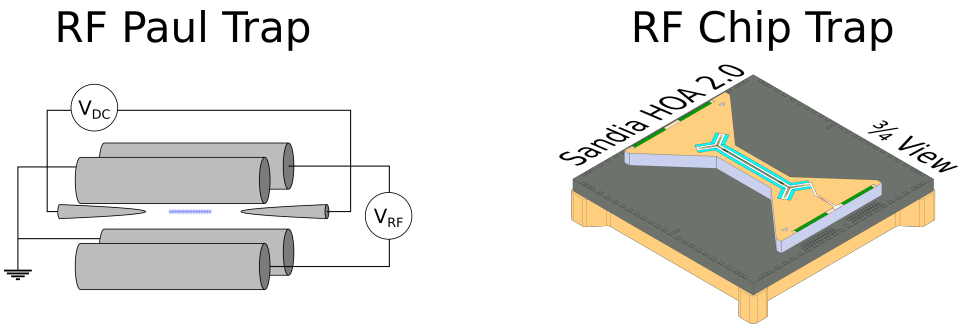

Figure 1.4: Two types of RF trap. To the left a symbolic image of a 4-rod Paul trap. To the right a render of the Sandia HOA 2.0 RF chip trap used in QuantumION

blade trap.[25] Ions are confined using a combination of static and time varying electric fields. Both types of field are needed as a consequence of Earnshaw's Theorem which forbids confining a charged particle using only electrostatic fields. Since the time dependent field usually oscillates in the radio-frequency (RF) these types of traps are referred to as RF traps. The most conceptually straightforward implementation of a RF trap is a 4-rod Paul trap, shown on the left in Figure 1.4. Chip traps operate on the same principle as Paul traps, however the geometry is flat making the electric fields difficult to visualize. The benefit of a chip trap is that they have more electrodes allowing greater control over the potential especially along the axial direction (See Appendix B for explanation on the distinction between axial and radial directions). Having more control along the axial direction helps produce a uniformly spaced ion chain and allows study of ion shuttling which may become very important for scaling trapped ions. An image of the Sandia HOA 2.0 trap and the electrode pattern for the trap is shown in Figure 1.5.

1.4 Author's Contributions

In Chapter 2 a code base was developed based on the cooling theory developed by Reiß *et al.*.[27] This code built on Reiß *et al.* by including laser linewidths following Sawamura *et al.* and including external heating rates as a new contribution.[28] The code is all original tailor written to the task of producing the results detailed in this thesis. Extensive simulations were done to rigorously ensure the QuantumION layout and limitations would produce near ground state cooling.

Chapter 3 details the QuantumION individual addressing approach with a particular focus on the limitations to different approaches and design of a working micro-lens array

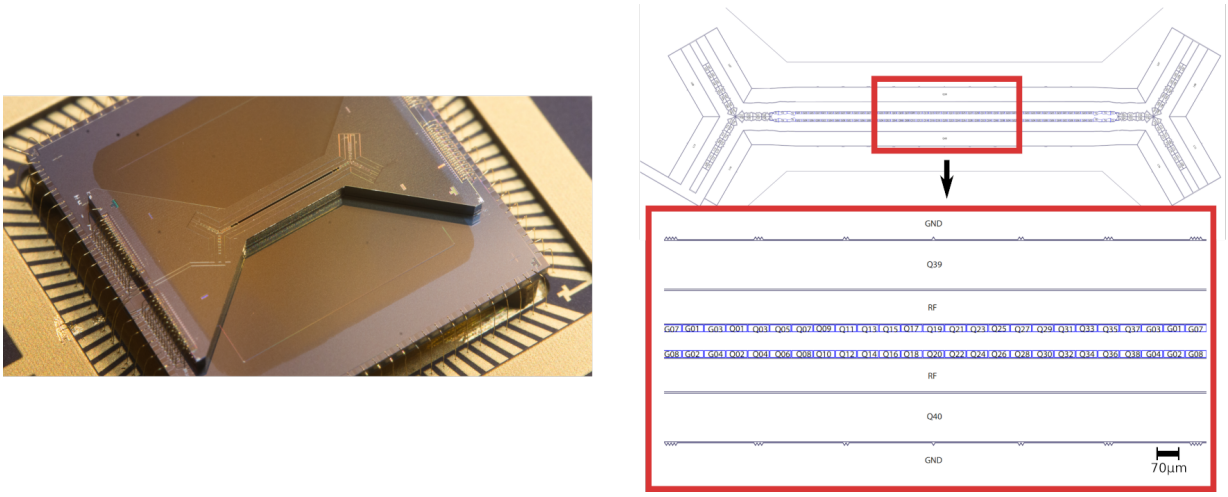

Figure 1.5: On the left is an image of the Sandia HOA 2.0 trap. On the top right is a sketch of all the electrodes on the surface of the trap. The zoom view at the bottom right is an image of just the quantum zone. The Y-junctions at the edges of the trap are for re-ordering the ion chain.[26]

(MLA) solution. Extensive Zemax simulation was performed to design a MLA and bulk telescope. In addition to the work documented in the thesis the author made significant contributions to the overall beam path design outside of the specifics detailed in the thesis. The inciting idea for the QuantumION individual addressing scheme was conceived by Dr. Matthew Day, the post-doctoral fellow overseeing much of the optical design for QuantumION. The author's contribution was initially validating Dr. Day's approach, then making the necessary modifications as different aspects of the initial approach became infeasible or otherwise had to be altered. The work of whittling down a concept into a fully specified design through intense scrutiny was the primary contribution of the author.

Finally Chapter 4 describes a design philosophy for making optical assemblies in QuantumION and an example pegboard built with this approach is presented. As a COOP student in Professor Islam's QITI group the author built the very first pegboard optical assembly. This assembly displayed excellent stability even through a relocation of the lab space. This performance has motivated further investment into pegboard optical assemblies. The work in this Chapter is entirely the author's contribution from part selection to design and assembly. The machining was performed by an external machine shop.

Chapter 2

Cooling

The electronic energy levels of a trapped $^{133}Ba^{+}$ ion, shown in Figure 2.1, begs the question: why do the ions need additional cooling? Temperature fluctuations with the same energy as the 1762nm transition would need the room to be at ≈8000K. The key is to realize that there are two energy scales: the internal electronic states and the motional modes which behave like harmonic oscillators. The latter is used to mediate interactions between ions in the chain. The equivalent temperature between adjacent HO energy levels for a 1MHz motional mode is ≈50μK. To make these states behave as the quantum bus it's crucial to have a sufficiently low temperature. Fortunately trapped ions can be cooled to below this threshold using only lasers. It is these techniques which will be investigated in this chapter.

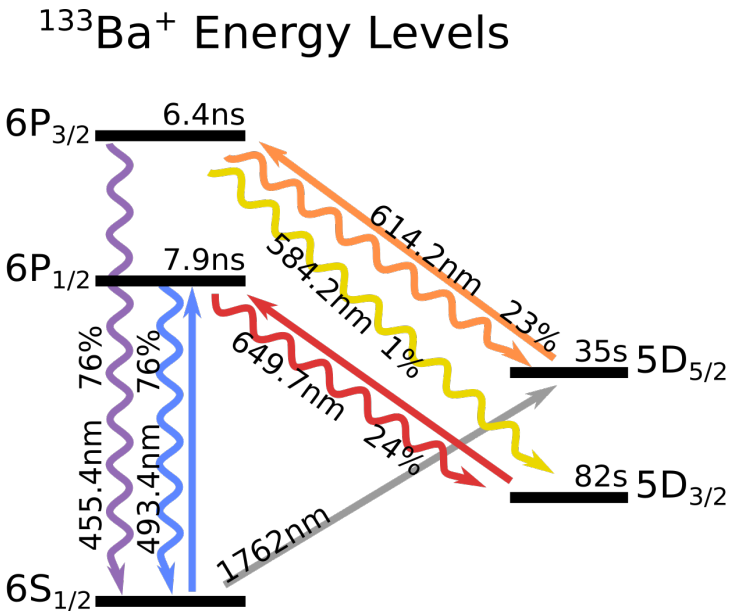

Figure 2.1: Full barium energy level structure with branching ratios and lifetimes. As well the lasers which are available for driving resonant transitions are shown in the figure as arrows. For instance the lab does not have a 585nm laser.

Two ground state cooling methods are investigated for the QuantumION configuration. Before they can be investigated the tools for executing this investigation are developed in Section 2.1. These tools are used to investigate quenched resolved sideband cooling (QRSC) in Section 2.2 and electromagnetically induced transparency (EIT) cooling in Section 2.3. For both methods first the specifics of the cooling mechanism are described, then expected cooling rates and cooling times are investigated. Finally a set of optimized cooling parameters are presented which in both cases achieve suitably low temperatures for the intended motional modes.

2.0.1 Typical Cooling Sequence

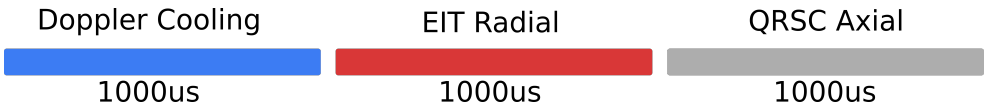

Figure 2.2: An example cooling sequence for QuantumION. Hot ions are subjected to extended Doppler cooling which will bring all motional modes to the Doppler limit. Subsequently EIT cooling is applied to the radial modes then QRSC is applied to the axial modes. At the conclusion all directions will be in the motional ground state.

The required final temperature for successful experiments has progressed somewhat over the past 30 years. The first paper to suggest a two ion entangling operation required those ions to be in the ground state.[21] The next major step forward presented a method of entangling ions without cooling to the ground state[22], however when the authors said "hot" they meant around 5 quanta of thermal energy. Far from room temperature, and farther still from the starting temperature of the atoms after being loaded into the trap. Whether the ions are being loaded from a "classic" thermal oven or from an ablation oven the "just caught" ions will be in the 500-3000K range.[29]

To address this essentially all trapped ion experiments require a cooling sequence ahead of the actual experiment. There are a handful of cooling methods with varying levels of obscurity, but the standard is a two step process. First the ions are Doppler cooled from their "very hot" starting temperature down to the Doppler limit,[1] after which a ground state cooling technique is used to bring the temperature down to the final temperature. Cooling beyond the Doppler limit is necessary for contemporary experiments. The cooling sequence which QuantumION will be using as a result of this work is to first Doppler cool,

[1]For the QuantumION configuration and $^{133}Ba^{+}$ this corresponds to temperatures between 3 and 50 quanta of thermal energy. See Table 2.1 for more on the Doppler limit for this system.

then apply EIT cooling on the radial modes, and finally use QRSC on the axial modes, this sequence is shown in Figure 2.2. QRSC is used on the axial motional modes for two reasons: firstly the axial mode frequency span (from 206kHz to 1.8MHz) encourages sequential cooling of the modes. Secondly the existing QuantumION laser layout only supports ground state cooling of the axial modes through QRSC, all other considered cooling techniques have no cooling power along the axial direction. EIT cooling is well suited to the radial modes (2.6MHz to 3.3MHz) because laser parameters exist which will cool all these modes simultaneously.

Doppler Cooling

Doppler cooling is a versatile technique which can cool a trapped ion system efficiently along all three principle axis using only a single laser beam. The cooling can be realized on any short-lived transition for which a closed loop can be created. Closed loop meaning that the electron will not be trapped in a long-lived energy level which does not interact with the cooling laser. Typically the hardware requirements for Doppler cooling are lesser than those needed for the intended experiment after cooling, and so Doppler cooling truly is a workhorse in most experiments. The only drawback of this technique is that the temperature limit for Doppler cooling, the so called Doppler limit, is usually too hot for cutting edge experiments.

Deriving the Doppler Limit

A hot ion can be treated as a classical object undergoing harmonic motion which is described by

$$v(t) = v_0 \cos \omega_{trap} t \tag{2.1}$$

Where v(t) is the velocity as a function of time, and ω_{trap} is the characteristic frequency of the harmonic motion, also frequently referred to as the trapping frequency. In the limit $\omega_{trap} \ll \Gamma$ cooling is much faster than the motion of the ion, and so the radiation pressure can be modeled as a continuous friction force for each instantaneous velocity. Where Γ is the spontaneous decay rate from the excited energy level.[19]

Since the cooling is fast relative to the motion the momentum kick can be taken as a derivative:

$$\frac{\Delta p}{\Delta t} \overset{\omega_{trap} \ll \Gamma}{\approx} \frac{\mathrm{d}p}{\mathrm{d}t} \approx F_a = \hbar \vec{k} \Gamma \rho_{ee} \tag{2.2}$$

The rate of change in the momentum is then straightforwardly equal to the change in momentum for a single cooling event ($\hbar\vec{k}$) scaled by the rate of decay from the excited

state (Γ) times the likelihood of finding the system in the excited state (ρ_{ee}). For a simple two level system with a single driving laser the excited state population is

$$\rho_{ee} = \frac{s/2}{1 + s + 2(\delta_{eff}/\Gamma)^2} \tag{2.3}$$

where δ_{eff}=$\Delta - \vec{k} \cdot \vec{v}$, the laser detuning ($\Delta$) minus the Doppler shift of the light in the ion frame, and s is the saturation parameter defined as s=$2|\Omega|^2/\Gamma^2$. Where Ω is the Rabi-rate as defined in Section 1.2.2.

As the ion approaches it's final temperature the velocity is small enough that the friction force can be approximated (F_a) as a Taylor series to the first order,

$$F_a = \sum_n \frac{F_a^{(n)}(v)}{n!} v^n \approx F_0(1 + \kappa v). \tag{2.4}$$

Note the velocity entered this expression from ρ_{ee}. The zeroth order term is

$$F_0 = \frac{\hbar k \Gamma}{2} \frac{s}{1 + s + (2\Delta/\Gamma)^2} \tag{2.5}$$

this is the radiation pressure which displaces the ion from the tap center. The first order term is scaled by

$$\kappa = \frac{8k}{\Gamma^2} \frac{\Delta}{1 + s + (2\Delta/\Gamma)^2} \tag{2.6}$$

which is called the friction coefficient, and is the term which produces the cooling effect by dampening the motion of the ion analogous to adding a friction term to a classical object in harmonic motion. Notice that the F_0 term can never be negative, meaning the zeroth order term can never contribute to cooling. Meanwhile the first order term (labeled F_1) can be tuned to be cooling by having a negative Δ. So the cooling rate ($\dot{E}_c$), modeled as viscous drag, is the product of the velocity and friction force:

$$\dot{E}_c = \langle F_a v \rangle = F_0(\langle v \rangle + \kappa \langle v^2 \rangle) = F_0 \kappa \langle v^2 \rangle, \tag{2.7}$$

The zeroth order term can be set to zero by observing that over many oscillation cycles it will average to zero. An equivalent statement is that the zeroth order term is linear in velocity so will average to zero as the ion moves back and forth, while the first order term is quadratic in velocity so will not average out.

As alluded to earlier, there is a limit to the achievable temperature through Doppler cooling and a primary limitation is the momentum kick each spontaneous emission imparts

on the ion. This effect manifests as a heating rate ($\dot{E}_h$) which works against the cooling rate.

$$\dot{E}_h = (1+\alpha)\frac{\hbar^2 k^2}{2m}\Gamma\rho_{ee}\Big|_{v=0} \tag{2.8}$$

Notice this heating rate is proportional to the momentum kick from a single photon ($\hbar^2k^2/2m$) scaled by the scattering rate from the excited state ($\Gamma\rho_{ee}$) where ρ_{ee} is evaluated at zero velocity. α comes from the spontaneous emission angular distribution; since the ion will scatter light in all directions, but considered here is a 1D trap, only a portion of the scattered light will contribute to heating in this one direction. For dipole allowed transitions α=2/5.[30]

By equating the heating and cooling rates an expression for $m\langle v^2\rangle$ can be extracted. The average kinetic energy expressed as an expectation value for the number operator is then:

$$\bar{n}_{min} = \frac{\Gamma\sqrt{1+s}}{4\omega_{trap}}(1+\alpha). \tag{2.9}$$

However the Doppler limit is more commonly written as

$$\bar{n} = \frac{7\sqrt{2}\Gamma}{20\omega_{trap}} \approx \frac{\Gamma}{2\omega_{trap}} \tag{2.10}$$

where the "ideal" parameters, which maximize the friction force, have been substituted into the more general expression. These are $\Omega = \Gamma$ and $\Delta = -\Gamma/2$.

Using the simplest form of Equation 2.10 the Doppler limit for the expected trapping frequencies in the QuantumION trap can be tabulated in Table 2.1. These numbers are crucially important since this will be the starting temperature for all subsequent sub-Doppler cooling techniques. See Appendix C for more on the expected trapping frequencies.

Motional Mode (MHz)	Doppler Limit ($\bar{n}$)
3.000	3.358
2.690	3.744
3.300	3.052
3.021	3.334
1.886	5.340
0.206	48.902

Table 2.1: The Doppler limit calculated on the $S_{1/2}$ - $P_{1/2}$ transition in the $^{133}Ba^{+}$ ion where Γ=20.1MHz. Values listed for the highest and lowest frequency modes along all three directions. See also Appendix C.

The Doppler cooling Hamiltonian after transforming to an appropriate rotating frame is

$$H = \begin{bmatrix} 0 & \Omega/2 \\ \Omega/2 & \Delta \end{bmatrix} \tag{2.11}$$

where Δ is the detuning from the carrier frequency, and Ω is the Rabi-rate. This Hamiltonian can be plugged into the tools developed in Section 2.1 and the analytical results above can be verified. The Doppler limit in the numerical simulations matched the analytical prediction and the optimum cooling parameters did in fact correspond to the location with the fastest cooling rate. As foreshadowing of the following sections the coldest temperature was not for the same parameters which maximize cooling rate. External heating rates were added to the simulation and it was found that Doppler cooling is still effective. See Figure 2.3.

These types of plots will be used throughout this chapter, especially for parameters scans, so it's worthwhile to review how they are intended to be read. To the left is a contour plot of the *log* of the steady state temperature, so a contour labeled 0 would correspond to an expectation value of 1 for the harmonic oscillator, or one quanta of heat energy in the system. In the top right of the plot is the *external* heating rate for the calculations, more on this in Section 2.1. The large swaths of white-space are areas where cooling was not possible; the heating rate is greater than the cooling rate. And finally along the axis are the parameters being scanned in Hertz, in this case it is the power in the cooling beam as a Rabi-rate, and the detuning of the cooling beam (with an implied negative sign). The plot on the right has the same structure, however instead shows the cooling *rate*. These two parameters largely define how cooling behaves and often are inversely related. Especially in the absence of external heating tuning the lasers to lower power usually improves the

steady state temperature at the cost of cooling rate, conversely increasing power increases the cooling rate at the cost of steady state temperature.

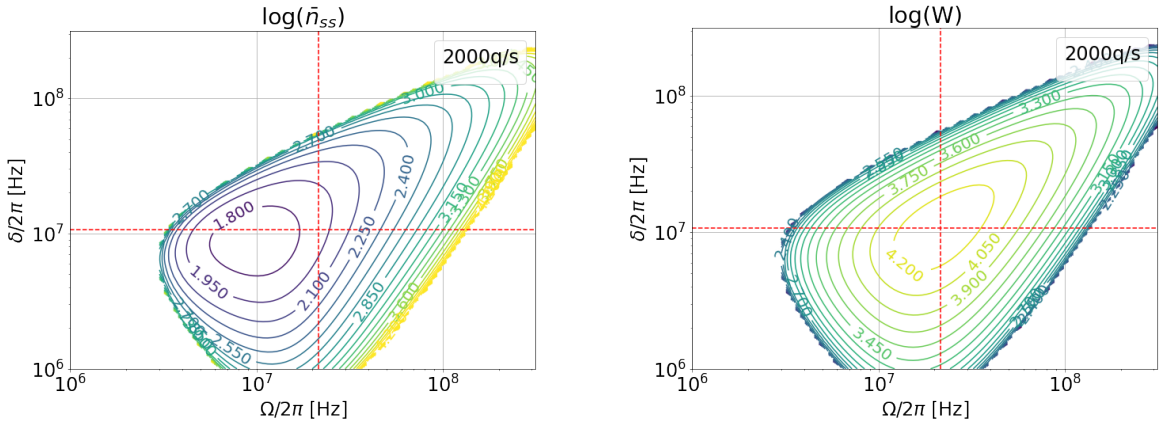

(a) Average phonon number for the 206kHz motional mode through scanning the cooling laser detuning (δ) and power (Ω). Dashed red lines at Ω=Γ and δ=$\Gamma/2$.

(b) Cooling rate for the 206kHz motional mode with the same parameter scan as Figure 2.3a.

Figure 2.3

Sub Doppler Methods

Table 2.1 shows that under ideal cooling conditions many of the motional modes would be too hot for even the entangling operations proposed by Mølmer and Sørensen.[22] Thus cooling techniques which can go below the Doppler limit must be investigated. The primary contribution to the Doppler limit that the ions continue to absorb and emit photons after being cooled; This process produces an excited state population which contributes to heating through diffusion. To reach the ground state a cooling technique needs to scatter less light at lower temperatures reducing the diffusion coefficient's contribution to the final temperature.

The two techniques investigated in this thesis which achieve this are electromagnetically induced transparency cooling (EIT Cooling) and quenched resolved sideband cooling (QRSC). The EIT effect is when an electromagnetic field pumps a medium into a coherent dark state. This is observed by a greatly diminished absorption profile using a second "probe" field at specific detunings. By engineering the transparency location to suppress

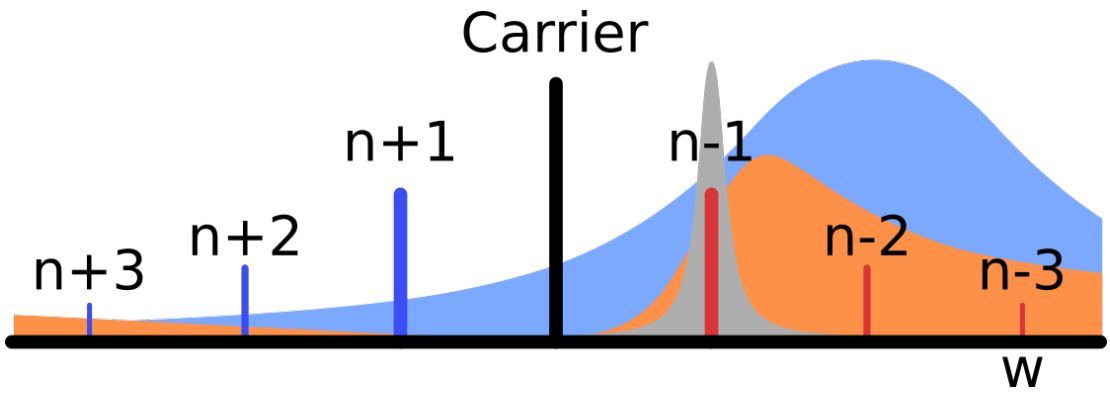

Figure 2.4: Frequency space plot showing the three key types of transitions. There are carrier transitions directly at the transition frequency. These do not change the HO state when absorbing a photon but can decay into any of $\{n-1, n, n+1\}$. To the left (right) there are the blue (red) sidebands which represent a heating (cooling) transition. While there are $n \pm 2, 3, \ldots, j$ transitions available, their Rabi-rate scales as η^j which means in the Lamb-Dickie regime only ± 1 and carrier transitions contribute significantly. See Section 1.2.2 for details. Superimposed on these transitions are absorption profiles which represent the three types of cooling investigated in this thesis. In light blue is Doppler cooling with a very broad peak, this broadness leads to excitation of heating and carrier transitions which leads to the Doppler limit. QRSC (grey) and EIT cooling (orange) both suppress unwanted transitions by being narrow linewidth and engineering a transparency respectively.

carrier transitions the same $S_{1/2}$ to $P_{3/2}$ transition which was too broad in a Doppler configuration can be used to cool to the motional ground state. Resolved sideband cooling instead addresses specifically the cooling transition with a laser narrow enough to be far detuned from carrier and heating transitions. Notice that the red sideband transition is impossible when the HO is in ground state since it requires $n \to n-1$, so RSC reduces the diffusion by ceasing to absorb photons if the HO is in the ground state.

2.0.2 Cooling Direction

A final nuance of cooling which has recently come into the forefront of trapped ion quantum computing is the question of which motional directions need to be cooled. Previously it had been thought that only the directions which will be used for quantum operations need to be cold. Only the quantum bus needs special care, the other directions don't couple

strongly to the ions during computation and so don't affect quantum operations. This turns out to not be the case for some individual addressing schemes. Specifically, Cetina *et al.* show that excessive motion in the axial direction can cause decoherence if tightly focused addressing beams are used, like the beams used in the QuantumION individual addressing scheme (See Chapter 3).[31] The ion will move in and out of the addressing beam's focus as it experiences thermal motion causing fluctuations in Rabi-rate and decoherence. Along the same theme West *et al.* demonstrate that if the ions are seeing a gradient in laser intensity along an axis, for instance if the ions were shifted perpendicular to the addressing laser direction, then they can have motional modes along the gradient direction excited.[32] These two factors can play off each other, with the axial motion moving the ion out of the beam focus that then excites further motion which further displaces the ion forming a feedback loop. For this reason QuantumION needs to have the capability to cool in the axial direction. (For the definition of radial and axial directions see Appendix B)

Doppler cooling makes use of a single beam at 45° to all principle axis which ensures that the Doppler limit will be reached for all directions. A question investigated in this thesis is whether the ground state can then be reached in all three directions given the laser beam configuration in QuantumION, and what techniques will have to be employed to reach the ground state in all directions?

2.1 Cooling Model for Calculating Useful Parameters

Some tools need to be developed to extract useful parameters for the QuantumION cooling scheme. Of particular importance are expected final temperatures, cooling times, and laser parameters needed to achieve this. Fortunately all of this can be found using the method presented in Reiß *et al.*, which is reproduced here.[27]

For trapped ion systems cooling is a stochastic process in which the population density of the motional modes are driven towards the ground state. This action has many caveats and complications, however this analysis begins with a simple single trapped ion in a 1D harmonic potential and in the resolved sideband regime. Generalizing to n ions in a 3D harmonic potential is straightforward. For now the resolved sideband regime is taken to mean that the harmonic oscillator energy levels are well resolved. The ion will start with some thermal distribution of population. In the density matrix formalism this can be written as

$$\rho_0 = \sum_n c_n \left|n\right\rangle\!\left\langle n\right| \tag{2.12}$$

where $|n\rangle$ are the harmonic oscillator number states.

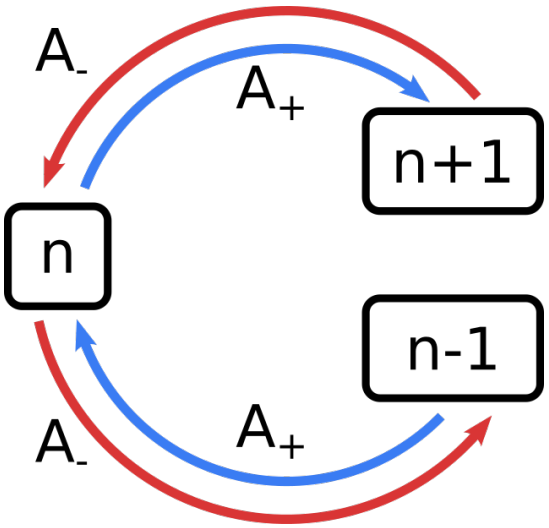

(a) For each energy level there are two quantum channels available. A cooling and a heating channel.

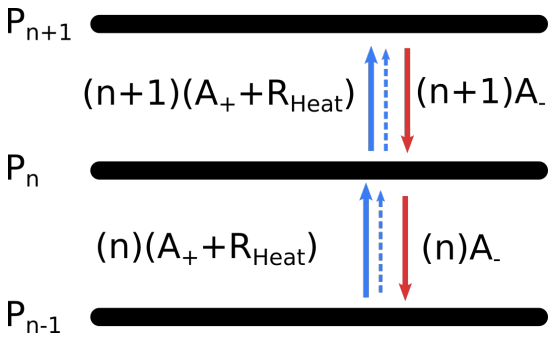

(b) Alternative view showing the same concept. Note that there are two arrows driving heating. The bold is from A_+ due to off resonant scattering and effects dependent on laser configuration, the second, R_{Heat}, is due to external heating effects.

Figure 2.5

For each HO level during the cooling process there are two quantum channels available: a heating channel, and a cooling channel. A diagram of this is shown in Figure 2.5. The rate at which the cooling (heating) channel is taken is captured by the A_- (A_+) parameter. The result of taking either channel is

$$\begin{aligned}
\rho_{A_+} &= a^\dagger \rho a = \sum_n a^\dagger \left|n\right\rangle\!\left\langle n\right| a & \rho_{A_-} &= a \rho a^\dagger = \sum_n a \left|n\right\rangle\!\left\langle n\right| a^\dagger \\
&= \sum_n \sqrt{n+1}\left|n+1\right\rangle\!\left\langle n+1\right|\sqrt{n+1} & &= \sum_n \sqrt{n}\left|n-1\right\rangle\!\left\langle n-1\right|\sqrt{n} \\
&= \sum_n (n+1)\left|n+1\right\rangle\!\left\langle n+1\right| = (n+1)\rho_{n+1} & &= \sum_n (n)\left|n-1\right\rangle\!\left\langle n-1\right| = (n)\rho_{n-1}
\end{aligned} \tag{2.13}$$

where the cooling (heating) channel is on the right (left).

Figure 2.5a shows the channels available to any HO level, however the useful parameters for cooling are aggregate parameters. The average temperature, the time to reach this average, the average cooling rate. So Figure 2.5b shows the same process but instead looking at the probability density for each energy level. Equation 2.13 shows where the n+1 and n prefactors in Figure 2.5b come from. With this in mind the change in average

occupation of any HO level can be read off the figure as

$$\dot{P}_n = (n+1)A_- P_{n+1} + nA_+ P_{n-1} - ((n+1)A_+ + nA_-)P_n \tag{2.14}$$

which is dictated by the rate of population entering and leaving a given level.[2]

[2]Note this is an application of a continuity equation which maintains conservation of probability current.

The equation can further be re-written to describe the change in expectation value of the number operator—the measure of temperature for HO systems:

$$\begin{aligned}
\langle n\rangle &= \sum_n nP_n \\
\langle \dot{n}\rangle &= \sum_n n\dot{P}_n \\
&= \sum_n n[(n+1)A_-P_{n+1} + nA_+P_{n-1} - ((n+1)A_+ + nA_-)P_n] \\
&= \sum_n A_-(n(n+1)P_{n+1} - n^2P_n) + \sum_n A_+(n^2P_{n-1} - n(n+1)P_n) \\
&= \sum_n A_-n(n+1)P_{n+1} - \sum_n A_-n(nP_n) \\
&\quad + \sum_n A_+((n+1)(n-1)+1)P_{n-1} - \sum_n A_+(n+1)(nP_n)
\end{aligned} \tag{2.15}$$

Adjusting the index of each sum to line up terms of matching n

$$\begin{aligned}
&= \sum_n A_-(n-1)(nP_n) - \sum_n n(nP_n) \\
&\quad + \sum_n A_+(n+2)(n)P_n + \sum_n P_n - \sum_n A_+(n+1)(nP_n) \\
&= \sum_n A_-[(n-1)\langle n\rangle - n\langle n\rangle] + A_+[(n+2)\langle n\rangle + 1 - (n+1)\langle n\rangle] \\
\langle \dot{n}\rangle &= -(A_- - A_+)\langle n\rangle + A_+
\end{aligned}$$

From this DE two useful regimes can be considered. First the steady state temperature which is simply found by setting the time derivative to zero

$$\langle n\rangle_{ss} = \bar{n}_{ss} = \frac{A_+}{A_- - A_+} = \frac{A_+ + R_{Heat}}{A_- - A_+ - R_{Heat}} \tag{2.16}$$

The second is to solve the DE for intermediate times producing the time dependent temperature function

$$\begin{aligned}
\langle n\rangle_t &= \langle n\rangle_0 e^{-(A_- - A_+)t} + \langle n\rangle_{ss}(1 - e^{-(A_- - A_+)t}) \\
&= \langle n\rangle_0 e^{-(A_- - A_+ - R_{Heat})t} + \langle n\rangle_{ss}(1 - e^{-(A_- - A_+ - R_{Heat})t}) \\
&= \langle n\rangle_0 e^{-(W - R_{Heat})t} + \langle n\rangle_{ss}(1 - e^{-(W - R_{Heat})t})
\end{aligned} \tag{2.17}$$

The steady state temperature is the primary metric of interest. Sufficiently low temperatures must be reached and this is the first check of whether that's even possible given enough time. The time dependent function instead gives an idea of what cooling *looks* like, but a more compact measure of cooling times would be the time constant, which is the inverse of the cooling rate:

$$W = A_- - A_+ = A_- - A_+ - R_{Heat}. \tag{2.18}$$

Notice the cooling rate (W) has the very intuitive form; the cooling rate minus the heating rate, with an additional external heating term. The addition of external heating rates is typically[3] omitted from cooling papers and is not mentioned by Reiß *et al.*, but for experimentalists is incredibly salient!

External Heating

This is a good time to discuss the difference between A_+ and R_{Heat}. The former is due to heating effects inherent to the laser configurations, the latter is due to external heating effects. Shortly a method for calculating A_+ will be discussed and this parameter enter into optimization for optimal cooling. The external heating in contrast is independent of the laser configuration, is always present, and is primarily due to electric field noise from the trap.[33] By recognizing that heating can be divided into these two types, and that external heating can be appended to the atomic simulations by modifying $A_+ \to A_+ + R_{Heat}$ more realistic simulations can be achieved with minimal alteration of the method.

Adding external heating also makes the simulation more robust. Reducing laser power is often an easy way to improve steady state temperature. This is because lower powers reduce off resonant effects and minimize A_+. Intuitively it's clear that this can't be done indefinitely. Eventually the power will approach zero and the time to reach temperature will approach infinity. By including external heating rates reducing laser power below an optimal amount is discouraged. Since A_- is also diminished by reducing laser power and if there is a fixed R_{Heat} which A_- has to compete with, then a timescale is naturally introduced to the problem.

Until the full experimental setup is assembled, ions trapped, and QuantumION operational, a true heating rate can't be known. An advantage of using the Sandia HOA 2.0 trap however, is that other groups have used the trap and reported heating rates. This allows an estimate of heating rates to be made based on available literature. This is shown in Table 2.2. Based on this survey heating rates of 2000q/s in the axial and 100q/s in the radial directions look like reasonable, conservative, placeholder external heating rates.

[3]The author has not seen it in any published paper on cooling.

Heating (q/s)	Direction	Species	Details
188±10	Radial	$^{171}Yb^{+}$	Perpendicular to trap[34]
88±6	Radial	$^{171}Yb^{+}$	Parallel to trap[34]
40	Radial	$^{171}Yb^{+}$	ω_{trap}=2.8MHz, ω_{RF}=50MHz [35]
100	unspecified	$^{171}Yb^{+}$	unspecified [36]
780±50	axial	$^{171}Yb^{+}$	ω_{axial}=2.5-5.2MHz, ω_{radial}=12.7MHz[37]
≈ 2000	axial	$^{88}Sr^{+}$	ω_{trap}=600kHz[38]

Table 2.2: Literature survey of heating rates for chip traps. As mentioned in Section 2.0.2 the axial heating rates have not been critical parameters until very recently and so it is challenging to find published heating rates for this direction. Above the horizontal bar are results for the Sandia HOA 2.0 trap, below the line is first a result for a Sandia National Labs trap but not the HOA 2.0 model, and finally a trap not manufactured by Sandia.

Calculating A_- and A_+

From Equations 2.16 and 2.18 it's clear that the primary cooling metrics are dependent on $A_\pm$. So calculating key cooling parameters is a matter of calculating the rates at which heating and cooling transitions are driven by the laser configuration under test. $A_\pm$ are the rates at which the ion system gains or loses energy from the environment. The master equation formalism allows any coupled open system be written as

$$\frac{d\rho}{dt} = \frac{1}{i\hbar}[H, \rho] + \mathcal{L}^d\rho \tag{2.19}$$

where ρ is the density operator of the atom and trap system, H is the full Hamiltonian for the atom and $\mathcal{L}^d$ is the Liouvillian super-operator which couples the atomic system to the environment through spontaneous emission.[39] H can be further divided into three terms

$$H = H_{trap} + H_{atom} + H_{int} \tag{2.20}$$

where H_{trap} is the harmonic oscillator Hamiltonian associated with the motional modes of the ions confined by the trapping potential of the RF trap. H_{atom} is the internal Hamiltonian of the atom where the energy level structure of the atom is captured. Finally H_{int} is the interaction term which couples the trap Hamiltonian to atomic Hamiltonian.

For this analysis the interaction term is expanded using the multipole expansion of the

electric field.

$$H_{int} = H_{dipole} + H_{quadrupole} + \dots \tag{2.21}$$

For dipole allowed transitions this expansion can be terminated at the dipole term. However for dipole forbidden transitions, like the $S_{1/2}$ to $D_{5/2}$ transition, the dipole term is zero and the expansion must be taken a term further. These are quadrupole transitions.[40]

For now we will only take the expansion to the dipole limit.[27].

$$H_{int} \approx H_{dipole} = \sum_{i,j} \hbar\Omega_{i,j}(\vec{x})(R_{ij} + R_{ji}) \tag{2.22}$$

Where

$$R_{ij} = R_{ji}^{\dagger} = |j\rangle\langle i|\, e^{i\vec{k}_{ij}\cdot\vec{x}} \tag{2.23}$$

In the Lamb-Dicke regime defined by $1 \gg \eta = \cos\theta\left|\vec{k_{ij}}\right|\sqrt{\frac{\hbar}{2m\omega_t}}$ the ion is well localized. Because of this the dipole interaction operator can be further approximated as a Taylor series around the center of the trap.

$$H_{dp}(x) \approx H_{dp}(0) + x\Big(\frac{\partial}{\partial x}H_{dp}(x)\Big)_{x=0} = H_{dp}(0) + xF(0) \tag{2.24}$$

Note for convenience $\frac{\partial}{\partial x}H_{dp}(x)_{x=0}$ will be written as $F(0)$. This form of the dipole operator is simple enough to work with. The specific operator will be dependent on the laser configuration and which transitions are allowed by selection rules. Taking this abstract form as a given, the cooling and heating rates are

$$A_{\pm} = 2\,\mathrm{Re}\{S(\mp\omega_{trap}) + D\} \tag{2.25}$$

where S is the auto-correlation of the dipole force and D is the diffusion coefficient. The auto-correlation is simply a convenient method of calculating the rate at which a transition at $\mp\omega_{trap}$ is excited. The diffusion coefficient is identical in function to the Doppler cooling case, and has a generalized definition:

$$\begin{aligned} D &= \sum_{i,j} \Gamma_{ij}\alpha_{ij}\frac{\hbar k_{ij}^2}{2M\omega_T}\,\langle|i\rangle\langle i|\rangle_{SS,In} \\ &= \sum_{i,j} \alpha_{ij}\,\langle\rho_{ii}\rangle\,\Gamma_{ij}\eta_{ij}^2 \end{aligned} \tag{2.26}$$

$\Gamma_{i,j}$ is the decay rate from the energy levels i and j, $\alpha_{i,j}$ is the angular distribution of the spontaneous emission, and $\langle \rho_{ii,ss} \rangle$ is the steady state expectation value of the excited level. While this term is suppressed with QRSC and EIT cooling it does still contribute to the final temperature as it did for the Doppler cooling case.

The auto-correlation is typically expressed in the integral form however it's far easier to perform matrix computations for numerical simulations which is why it's re-written like:[27]

$$\begin{aligned} S(\pm\omega_T) &= \frac{\hbar}{2M\omega_T} \int_0^\infty e^{\pm i\omega_{trap} t} \langle F(t)F(0) \rangle_{ss,atom} \\ &= \frac{\hbar}{2M\omega_T} \mathrm{Tr}\big\{ F(-i\omega_T - \mathcal{L})^{-1} (F\rho_{ss,atom}) \big\} \end{aligned} \tag{2.27}$$

With this definition written in terms of system parameters the key cooling parameters can be calculated for arbitrary laser configurations. The nice thing about this method is it's generality. Once the code for making these calculations is written it can be applied to a vast number of different Hamiltonians.

2.1.1 Quadrupole Transition

The method above focused on dipole allowed transitions, however the proposed QRSC scheme in the following section uses a laser at 1762nm to drive quadrupole transitions so at first glance it appears there is some conflict here. However since quadrupole transitions can be folded into the same framework as dipole transitions the difference can be fully captured by the Rabi-rate, so there is no conflict. The major difference between the two types of transitions is the Einstein-A coefficient[41] which scales the Rabi-rate,

$$\Omega = \frac{e|E|}{\hbar} \sqrt{\frac{5A_{ge}^{E2}\lambda^3}{64\pi^3 c\alpha}} \tag{2.28}$$

where all the physical constants follow their usual definitions, note α here is the fine structure constant not the angular spontaneous emission distribution discussed above, and A_{ge}^{E2} is the Einstein-A coefficient.[16]

2.2 Quenched Resolved Sideband Cooling (QRSC)

Resolved sideband cooling straightforwardly addresses a sideband transition reducing the temperature by coherently driving a $n \rightarrow n-1$ transition. By working in the resolved

sideband regime the Doppler limit can be surpassed, as off resonant excitation of carrier transitions are significantly detuned from the narrow linewidth laser. Repeatedly driving the cooling transition more than the heating transition is on average cooling the ion.

The catch however is finding a pair of energy levels which have the suitable linewidth for RSC. If the transition is too broad, like the $S_{1/2}$ to $P_{3/2}$, then the sidebands will not be resolved since the carrier linewidth is much greater than the trapping frequency. If the selected energy level is too narrow on the other hand, like the $S_{1/2}$ to $D_{5/2}$ then the cooling times would take too long. So long in fact that the external heating would be greater than the achievable cooling.

This is where the "Quenched" comes in; a narrow transition can be broadened by utilizing an auxiliary short-lived energy level. For QuantumION this is the 1762nm transition which is broadened by the 614nm laser. Adjusting the coupling strength between the narrow and broad energy levels creates an effective two level system with tailored linewidth.[42] This is shown in the ladder diagram picture in Figure 2.6b.

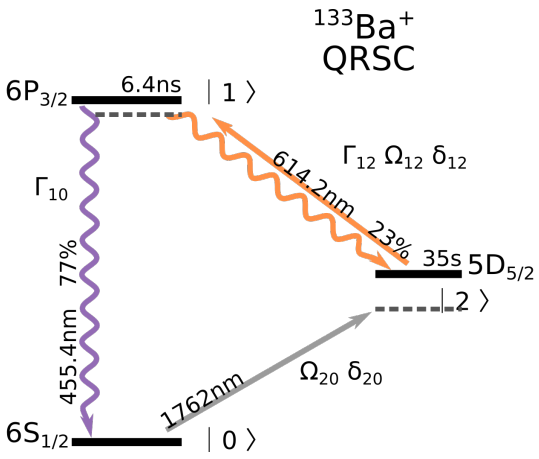

(a) The relevant energy levels for quenched resolved sideband cooling. The $D_{3/2}$ energy level is not relevant since the branching ratio into that level is small and can be re-pumped into the $S_{1/2}$ rapidly relative to the cooling rate.

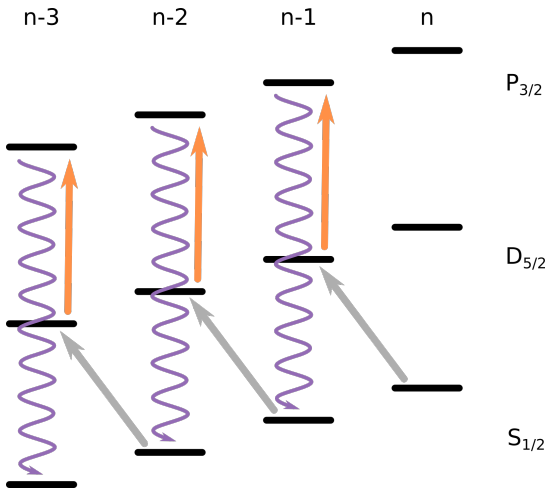

(b) Ladder diagram picture of quenched resolved sideband cooling. The $S_{1/2}$ to $D_{5/2}$ transition performs the cooling function while the orange light at 614nm quenches the transition to the short-lived $P_{3/2}$ energy level allowing for improved cooling rates.

Figure 2.6

2.2.1 Involved Energy Levels

QRSC was investigated for the QuantumION system. The available transitions and lasers are shown in Figure 2.1. The only transition which could feasibly serve as the narrow linewidth energy level is the 1762nm transition which couples $S_{1/2}$ to $D_{5/2}$. In turn the 614nm transition which couples $D_{5/2}$ to $P_{3/2}$ must be the quenching transition used to broaden the $D_{5/2}$ level. The $P_{3/2}$ level decays to the $D_{3/2}$ level with a small likely-hood, by applying a re-pump laser at 650nm the contribution of the $D_{3/2}$ level can be adiabatically eliminated.

2.2.2 Calculating Heating and Cooling Rates

For the case of QRSC the atom and lasers are configured according to Figure 2.6a. This configuration corresponds to this Hamiltonian

$$H_{rot} = \begin{bmatrix} 0 & 0 & \frac{\Omega_{20}}{2} \\ 0 & -\delta_{12} - \delta_{20} & \frac{\Omega_{12}}{2} \\ \frac{\Omega_{20}}{2} & \frac{\Omega_{12}}{2} & -\delta_{20} \end{bmatrix} \tag{2.29}$$

which has had the rotating wave approximation applied and has been transformed by unitary operator into a frame which eliminates time dependence.

Likewise F defined in Section 2.1 was found to be

$$F = \begin{bmatrix} 0 & 0 & -\frac{\hbar}{2} i k_{20} \Omega_{20} \\ 0 & 0 & -\frac{\hbar}{2} i k_{12} \Omega_{12} \\ \frac{\hbar}{2} i k_{20} \Omega_{20} & \frac{\hbar}{2} i k_{12} \Omega_{12} & 0 \end{bmatrix} \tag{2.30}$$

With H and F in hand the steady state temperature and cooling rate can be calculated from Equations 2.16 and 2.18 respectively.

2.2.3 Expected Steady State Temperatures

Having developed the necessary tools ideal cooling parameters can be searched for. Here is where the parameter space for QuantumION comes into effect, while the tools allow for arbitrary laser configurations there are constraints due to the limitations of the physical hardware. In fact these limitations were a motivating force for developing the tools. Since the 1762nm transition is an odd wavelength and needs to be a very narrow linewidth the

transition can only be driven at around 10kHz. This limitation is based on the expected losses and power available at 1762nm. The 614nm transition is a less demanding wavelength and easier to find laser diodes for, consequently the available Rabi-rate for this transition is easily into the MHz.

To make the most of the limited power at 1762nm, the laser should be tuned on resonance with the $n-1$ cooling transition. This will be ω_{trap} detuned from the carrier transition. However the presence of an intense laser, primarily at 614nm, will shift the energy level spacing due to a "light shift". This has to be accounted for to remain on resonance with the cooling transition and this condition is summarized as

$$\delta_{20} = -\omega_{trap} + \tilde{\delta}_{20} + \tilde{\delta}_{12}, \tag{2.31}$$

where

$$\begin{aligned} \tilde{\delta}_{20} &= \omega_{trap} - \sqrt{\omega_{trap}^2 - \Omega_{20}^2} \\ \tilde{\delta}_{12} &= \frac{\Omega_{12}^2}{(\Gamma_{10}^2 + \Gamma_{12}^2) + 4\delta_{12}^2}\delta_{12} \end{aligned} \tag{2.32}$$

By constraining the detuning on 1762nm according to these equations the light shift is corrected for.[28] In practice due to the limitations on laser power the light shifts are largely minimized and the final detunings are not significantly different from the bare sideband detuning. Equation 2.32 shows this to be true in the case where the Rabi rate for 1762 is much smaller than the trapping frequency and that the detuning of the 614 is much larger than the Rabi rate. This is almost always true for the parameter space investigated.

The detuning of the pump laser is ostensibly a free parameter, however in truth it does not have a large effect on the cooling rate. This is because the pump laser does not participate in the cooling process except to expedite spontaneous decay. Thus the detuning and Rabi-rate at 614nm can be seen as one parameter which controls an effective line width;[28]

$$\Gamma_{eff} = \frac{\Omega_{12}^2}{(\Gamma_{12} + \Gamma_{10})^2 + 4\delta_{12}^2}\Gamma_{10} \tag{2.33}$$

For this reason it's appropriate to fix the detuning and focus on finding the ideal pair of Rabi-rates for both lasers which produces the lowest temperature at a given external heating rate.

Fixing the quench laser detuning to 300MHz and adjusting the 1762nm laser frequency according to Equation 2.31 reduces the parameter space to just the two laser Rabi-rates.

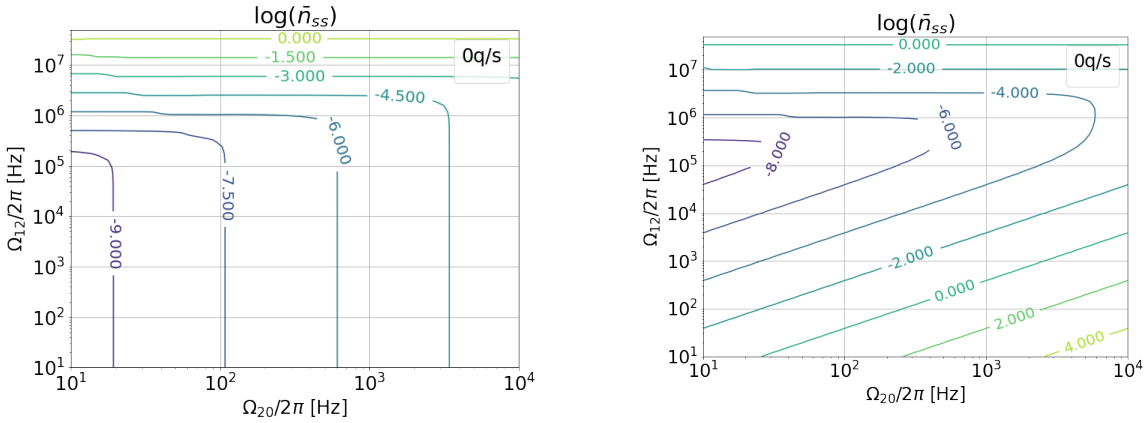

(a) Simulation excludes laser linewidths and only spontaneous emission from the $P_{3/2}$ state (25MHz) enters the Liouvillian.

(b) Expected laser linewidths of 1Hz for the 1762nm laser and 500kHz for the 614nm laser added to Liouvillian.

Figure 2.7: Steady state temperature for QRSC with δ_{12}=-300MHz and δ_{20} following Equation 2.31. Calculations were done for the axial direction common mode which is the lowest frequency motional mode at 206kHz. Consequently this mode will start the hottest.

This allows a 2D contour plot to be drawn of the steady state temperatures achievable through the available laser powers. This is shown in Figures 2.7 and 2.8.

The first parameter sweep is of expected steady state temperature for the axial common mode (lowest frequency mode) for the ion chain with zero external heating. This is done without defining inherent laser linewidths (Figure 2.7a). Under these conditions there are two major observations. Firstly above a certain amount of power the effective linewidth is so broad that off resonant heating becomes significant, this is visible above 100kHz-1MHz on the quenching laser. Meanwhile below this cutoff the 1762nm laser is the dominant determinate of temperature and lowering 1762nm power produces lower temperatures by reducing off resonant excitation of the heating and carrier transitions. Under these conditions broadly reducing power in both lasers produces lower temperatures.

Adding inherent linewidths, which can be done as an addendum to the Liouvillian following Sawamura *et al.*, to the lasers modified these results with about an order of magnitude higher temperatures and a change in the low quenching power behaviour (Figure 2.7b).[28] At high quench powers the effective linewidth is dominant and matches the previous plot. At low quench powers the transition linewidth is partially determined by the laser linewidth, with increasing contribution at lower powers.

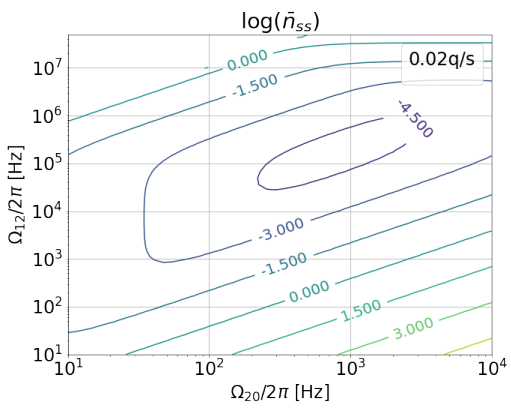

(a) 0.02q/s external heating rate; far less than expected.

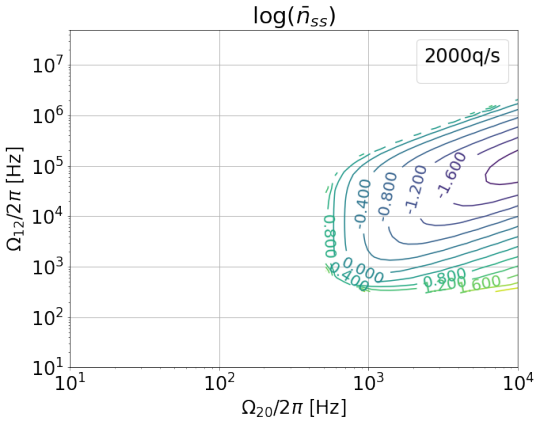

(b) 2000q/s external heating rate, expected heating rate from Table 2.2.

Figure 2.8: Steady state temperature for QRSC with δ_{12}=-300MHz and δ_{20} following Equation 2.31. Calculations were done for the axial direction common mode which is the lowest frequency motional mode at 206kHz. Laser linewidths of 1Hz for 1762nm, 500kHz for 614nm, and 25MHz $P_{3/2} - S_{1/2}$ linewidth form the collapse operators for the Liouvillian.

In Section 2.1 the value of including external heating rates was emphasized. These claims are validated by considering the dramatic effect adding even 0.02q/s of external heating has on expected temperatures. Adding this small external heating rate shifted the optimal Rabi-rate from 10Hz to ≈1kHz, seen in Figure 2.8a. The 0.02q/s heating rate is orders of magnitude better than what can be expected from modern chip traps and still has such an effect on the temperature plot. In the plots with no external heating temperature is minimized by optimally suppressing unwanted transitions. But if this is done at the cost of cooling *rate* then when external heating is introduced it diminishes the result.

Increasing the heating rate to 2000q/s, which was found to be a reasonable expectation, further shifts the optimal parameters to higher laser powers, seen in Figure 2.8b. Again this is because the cooling rate now has to compare and compete against a fixed heating rate, and optimal cooling under these conditions is found at the point where the cooling rate is maximized but not at the cost of broadening the transition beyond what is necessary.

2.2.4 Expected Cooling Rates

So instead of considering the steady state temperature, the cooling rate can directly be calculated. When doing so it's found that cooling rates are highest at large laser powers, an expected result. What is a little surprising is that the coldest steady state temperatures, in the absence of external heating, are found for the same parameters as some of the slowest cooling rates. See Figure 2.9a compared with Figure 2.7b. This is explained by moving to lower laser powers, off resonant effects are minimized as is the diffusion coefficient. Adding external heating rates adds an external timescale so now cooling has to be fast enough to compete, and in this context higher laser powers become critical. This is best argued by Figures 2.9b and 2.8b which show that cooling isn't even possible for a large swath of the parameter space. And the island of good steady state temperatures in the latter figure corresponds to the location of fastest cooling rates in the former.

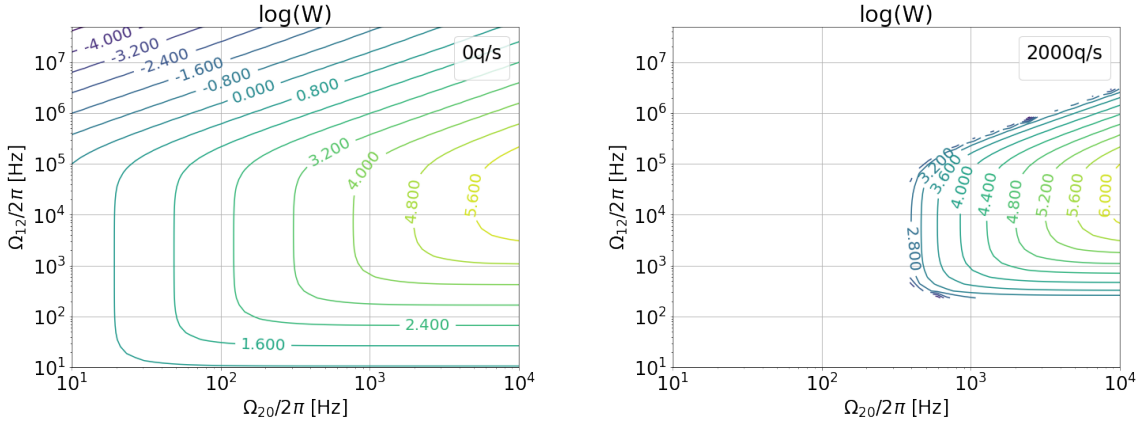

(a) No external heating present.

(b) 2000q/s external heating rate, expected heating rate from Table 2.2.

Figure 2.9: Cooling rates for QRSC with δ_{12}=-300MHz and δ_{20} following Equation 2.31. Calculations were done for the axial direction common mode which is the lowest frequency motional mode at 206kHz. Laser linewidths of 1Hz for 1762nm, 500kHz for 614nm, and 25MHz $P_{3/2}$ — $S_{1/2}$ linewidth form the collapse operators for the Liouvillian.

2.2.5 Expected Cooling Times

The final aspect of cooling which has importance in an experimental lab is the cooling times. This is especially critical in the QuantumION system which requires continuous

operation. Since each experiment is likely to need cooling, any improvement made from optimizing cooling will produce great time savings.

Solving Equation 2.15 yields the average phonon number as a function of time

$$\langle n \rangle (t) = \langle n \rangle_0 e^{-Wt} + \langle n \rangle_{ss} (1 - e^{-Wt}) \tag{2.34}$$

Based on the expected trapping parameters (see Appendix C) the motional mode frequencies can be calculated and used to find the starting temperature of each mode after applying Doppler cooling. The cooling curves of each of these modes can then be calculated and are plotted in Figure 2.10.

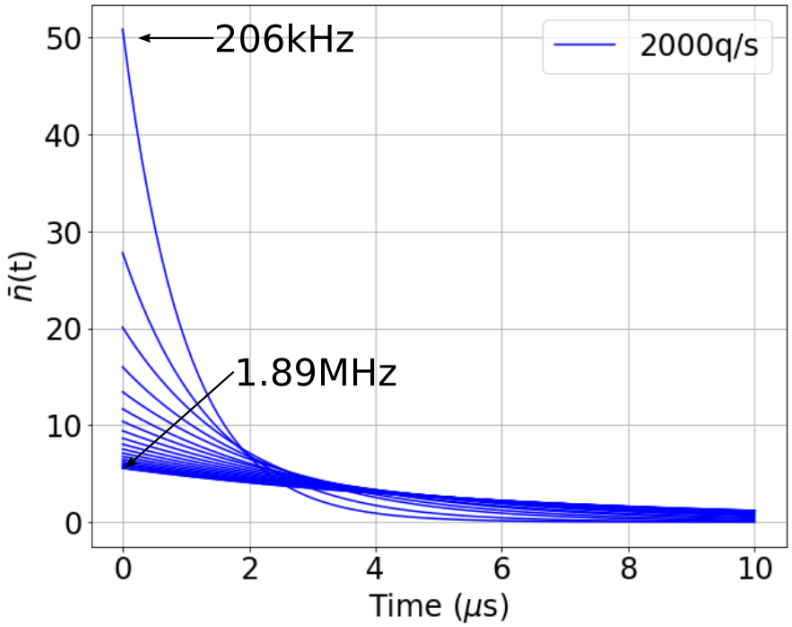

Figure 2.10: Expectation value of number operator for all axial direction motional modes. These span a frequency range from 206kHz to 1.89MHz. Laser parameters are optimized for each motional mode and listed in Table 2.3. Laser linewidths of 1Hz for 1762nm, 500kHz for 614nm, and 25MHz $P_{3/2}$ — $S_{1/2}$ linewidth form the collapse operators for the Liouvillian.

Importantly for QRSC only one mode can be cooled at a time. So while the plot shows all the motional modes being cooled simultaneously, each one would have to be cooled consecutively. This makes the total cooling time around 100μs instead of the 10μs plotted. Since each mode has to be individually cooled optimal parameters for each mode have

to be found; what works for the COM mode will not for the tilt mode. For the axial direction the COM mode is lowest frequency and all others sit at higher frequency, this reduces the LD parameter for higher frequency modes and therefore effectively reduces the available cooling power at that frequency. For this reason the cooling rate gets worse at higher frequencies, and in fact requires more time to reach steady-state. This effect actually accounts for a further increase in cooling times to a comfortable 1ms total QRSC time to give room for every mode to be thoroughly cooled.

To find optimal parameters two extreme cases were considered. Constrained optimization of only the laser Rabi-rates and unconstrained optimization of both Rabi-rates and detunings. It was found that, as was asserted earlier, only varying the Rabi-rates spans the parameter space. Allowing optimization of detunings did not show improved cooling rates or temperatures, increased compute times, and optimization settled on similar parameters to the artificial constraints which were lifted for this optimization. As well it was confirmed that the power and detuning in the quench laser were interchangeable. By decreasing the detuning the power requirements likewise decreased but no change in performance was seen, within reason. The numbers used to create Figure 2.10 are the result of constrained optimization, and are shown in Table 2.3.

2.2.6 Cooling Direction

The cooling direction was a critical experimental consideration. The beam must have good overlap with the principle axis which is to be cooled. This corresponds to the dot product of the laser and the trap direction, as was found in Section 1.2.2. Since QRSC is *not* a Raman process, the cooling is performed only by the 1762nm laser. The only beam which determines the cooling direction is therefore the 1762nm beam, and the way direction enters the Hamiltonian is through the Lamb-Dickie parameter

$$\eta = \cos\theta \left|\vec{k}\right| \sqrt{\frac{\hbar}{2m\omega_{trap}}} \tag{2.35}$$

where θ is the angle between the trap axis and the laser $\vec{k}$. The rate at which sideband transitions are driven is proportional to η so as the beam angle approaches $\pi/2$ the cooling rate approaches zero. Since the 1762nm laser makes a 45° angle with all trap axis, QRSC could be used to cool any of the motional modes. However η also has an inverse dependence on ω_{trap} which means that for the same laser power the cooling rate is diminished at higher trapping frequencies. Since the optimal parameters for the axial modes already make use

Frequency (kHz)	$\bar{n}_{ss}$	W (q/s)	Ω_{20} (kHz)	Ω_{12} (kHz)	δ_{20} (kHz)	δ_{12} (MHz)
206.0	0.00408	1041160	10.0	76.3	-205.7	-300.0
377.2	0.00455	699831	10.0	45.7	-377.0	-300.0
521.4	0.00495	519709	10.0	41.0	-521.3	-300.0
655.1	0.00625	441139	10.0	25.9	-655.0	-300.0
780.1	0.00640	365414	10.0	30.0	-780.1	-300.0
897.8	0.00713	321844	10.0	26.4	-897.7	-300.0
1008.7	0.00781	288765	10.0	24.0	-1008.6	-300.0
1113.4	0.00846	263205	10.0	22.1	-1113.3	-300.0
1212.2	0.00909	242824	10.0	20.6	-1212.1	-300.0
1305.3	0.00966	226047	10.0	19.8	-1305.2	-300.0
1392.8	0.01019	212154	10.0	19.3	-1392.7	-300.0
1474.6	0.01070	200572	10.0	18.9	-1474.6	-300.0
1550.7	0.01117	190855	10.0	18.7	-1550.7	-300.0
1620.8	0.01161	182745	10.0	18.4	-1620.7	-300.0
1684.4	0.01202	175951	10.0	18.2	-1684.4	-300.0
1739.8	0.01248	171367	10.0	15.5	-1739.8	-300.0
1791.7	0.01280	166444	10.0	15.4	-1791.7	-300.0
1816.2	0.01295	164224	10.0	15.4	-1816.2	-300.0
1885.0	0.01339	158280	10.0	15.3	-1885.0	-300.0
1886.3	0.01340	158163	10.0	15.3	-1886.3	-300.0

Table 2.3: Optimal cooling parameters found through constrained optimization. The detunings were fixed by picking δ_{12} to match the detuning in Sawamura *et al.* at 300MHz, and correcting for the light shift on δ_{20} following Equation 2.32.[28] The Rabi-rates were then optimized over the range available to QuantumION subject to laser power limitations. The single figure of merit for optimization was $\bar{n}_{ss}$ however the 2000q/s external heating rate set a timescale for cooling which ensured suitably fast rates.

of all the available 1762nm power, the possible rates and temperatures for the radial modes are sub-optimal.

2.2.7 Summary

QRSC was investigated for cooling the axial modes subject to the realistic constraints of the QuantumION system. Inherent laser linewidth, realistic external heating rates, and power limitations were all factored into searching for cooling parameters. A set of parameters was

found for each of the axial modes which would produce an average steady state temperature of less than 0.01 quanta for the axial direction. The highest frequency axial mode was left hottest with an steady state 0.013 quanta. The time to reach these temperatures was also considered and found that by cooling each mode sequentially around 1ms would be needed to cool *all* the axial modes. In short QRSC was found to be an effective cooling method for the axial modes which could be utilized to address the concerns with hot axial modes outlined in Section 2.0.2.

2.3 EIT Cooling

Electromagnetically Induced Transparency (EIT) is an interesting phenomenon where a three level[4] energy system is pumped into a "dark" state by a "pump" laser. The system will then not interact with a second "probe" laser at specific frequencies. In this way the medium becomes "transparent" to the probe laser hence the name.[44]

The additional insight needed to harness EIT for cooling is to realize that if the transparency is engineered to lie where the carrier transition would be, then off-resonant carrier transitions can be significantly suppressed. Thus the simplest implementation of EIT cooling can be realized. This thesis analyses the feasibility and expected results of EIT cooling for the QuantumION laser configuration. This analysis is done using the same formalism developed in Section 2.1. Using this analysis allows the consideration of realistic heating rates and finally optimum parameters are listed.

2.3.1 Involved Energy Levels

The specific energy levels in barium which are relevant to the QuantumION EIT cooling configuration are the $S_{1/2}$ to $P_{1/2}$ manifold, and the $D_{3/2}$ manifold is eliminated by a suitably fast repump laser at 650nm. This is shown in Figure 2.11a. EIT makes use of the hyperfine energy levels, unlike the QRSC technique. The cooling transition and laser for QRSC were so narrow that specific hyperfine levels could be resolved and with appropriate re-pumping the hyperfine structure could be ignored. For the EIT configuration since the broad $P_{1/2}$ energy level is the cooling transition a specific hyperfine level can not be picked solely by frequency. Instead the hyperfine levels have to be resolved by polarization.

Ideally the pump laser would have pure linear polarization perpendicular to the magnetic field which would pump equally from both $m_f = \pm 1$ levels. The probe laser would

[4]This effect can be observed in systems with more than three levels as well.[43]

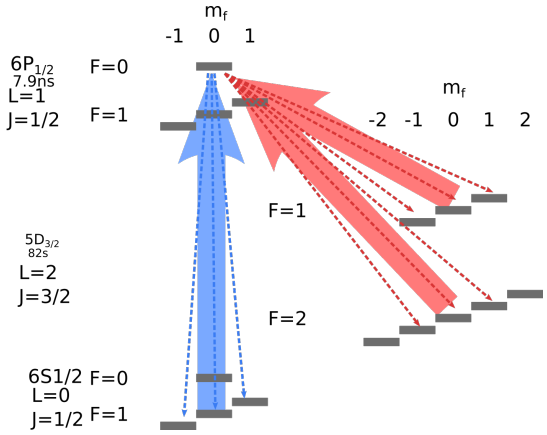

(a) All involved energy levels for EIT cooling. This includes the $D_{3/2}$ energy level where 24% of the excited population will decay to. However an application of a repump laser at 650nm with sufficiently fast Rabi-rates will effectively remove the $D_{3/2}$ energy level from the Hamiltonian.

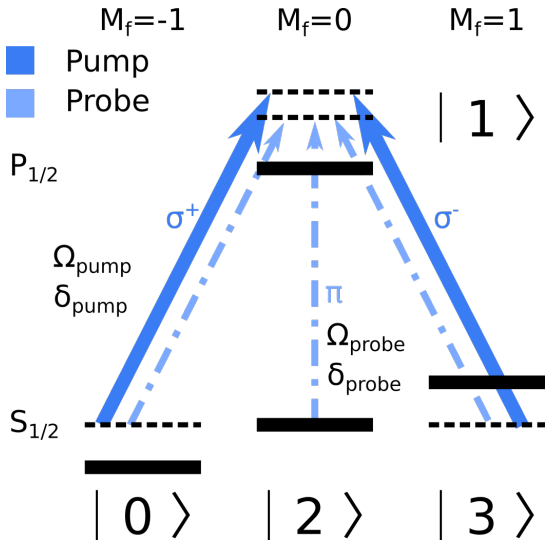

(b) The remaining energy levels after adiabatically eliminating the $D_{3/2}$ energy levels. Note that due to the beam layout depicted in Figure 2.12b a pure polarization is not available in the probe laser.

Figure 2.11

then have pure π polarization (linear parallel with the magnetic field). This configuration would make a nice time independent Hamiltonian. Due to the geometry constraints of the Sandia HOA trap it was not possible to produce pure polarization for the EIT configuration. The QuantumION beam layout is shown in Figure 2.12b, with the closest achievable polarization being both pump and probe beams linearly polarized, pump perpendicular to the trap surface producing pure $\sigma_{\pm}$ polarization, while the probe is forced to be polarized parallel to the trap. The lab frame polarization is related to the ion frame polarization by[41]

$$\hat{e}_{rad} = A_{\sigma_-}\frac{\hat{e}_x - i\hat{e}_y}{\sqrt{2}} + A_{\pi}\hat{e}_z + A_{\sigma_+}\Big(-\frac{\hat{e}_x + i\hat{e}_y}{\sqrt{2}}\Big) \tag{2.36}$$

For the configuration described in the probe beam the ion will see this polarization:

$$\hat{e}_{rad} = \frac{A_{\sigma_-}}{2} + \frac{A_{\pi}}{\sqrt{2}} + \frac{A_{\sigma_+}}{2} \tag{2.37}$$

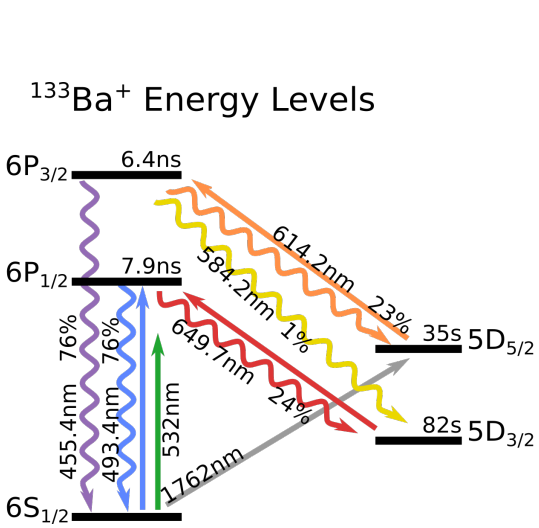

(a) Barium energy level structure and available lasers.

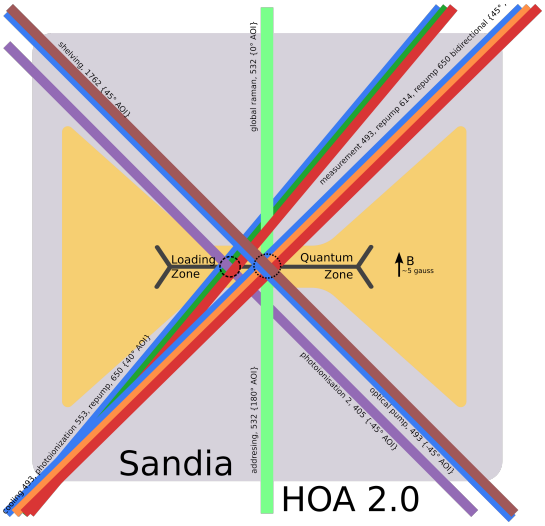

(b) The QuantumION beam layout overlaid above the Sandia trap.

Figure 2.12: The two beams used for producing an EIT configuration are the perpendicular 493nm beams incident on the quantum zone. Notice the limitations on polarization achievable relative to the magnetic field.

Accounting for Sub-Optimal Polarization

Due to the mixed polarization in the probe beam the interaction Hamiltonian has time dependent coupling terms which can not be removed by going to a rotating frame.

$$H_{total} = \begin{bmatrix} -\omega_B - \omega_{sp} & 0 & 0 & \frac{\Omega_{pump}}{2} e^{i\omega_{pump}t} \\ 0 & -\omega_{sp} & 0 & \frac{\Omega_{pump}}{2} e^{i\omega_{pump}t} + \frac{\Omega_{probe}}{2} e^{i\omega_{probe}t} \\ 0 & 0 & \omega_B - \omega_{sp} & \frac{\Omega_{pump}}{2} e^{i\omega_{pump}t} \\ \frac{\Omega_{pump}}{2} e^{-i\omega_{pump}t} & \frac{\Omega_{pump}}{2} e^{-i\omega_{pump}t} + \frac{\Omega_{probe}}{2} e^{-i\omega_{probe}t} & \frac{\Omega_{pump}}{2} e^{-i\omega_{pump}t} & 0 \end{bmatrix} \tag{2.38}$$

This poses a serious computational problem when applying the approach outlined in Section 2.1. Of course as Reiß *et al.* outline the method developed is still applicable, however it would be convenient if the system could be treated as a time independent Hamiltonian.[27] This way the code base developed for Section 2.2 could be re-used without alteration.

The Rabi-rate from the unwanted polarization is much smaller than the rate from the pump beam, and the probe power is split half into the π and a quarter of power into each of $\sigma_{\pm}$. The pump beam is about an order of magnitude more powerful; it was found empirically that the off polarization terms can be dropped without significantly altering the accuracy of the results. The match between time dependent and approximate excited state populations was found to be very robust in the fano-profile region, with mismatch at the broad peak. The mismatch there is likely due to the off polarization power being "missing" in the approximate term, and at the broad peak all beams are simply driving the population into the excited state. For the cooling simulations only the fano-profile region is of interest.

Figure 2.13 shows the agreement between full time dependent simulation and this ad-hock adjustment. The full time dependent Hamiltonian was simulated until steady state oscillations were observed, then the past 200 time-steps were averaged together to produce the dashed black curve. The averaging and judgment call on when to stop simulation are necessary since in the time dependent case there is no *true* steady state. In blue is the result of making the dropping the unwanted polarization. Doing this clearly matches the spectrum for the time dependent case over the region of interest.

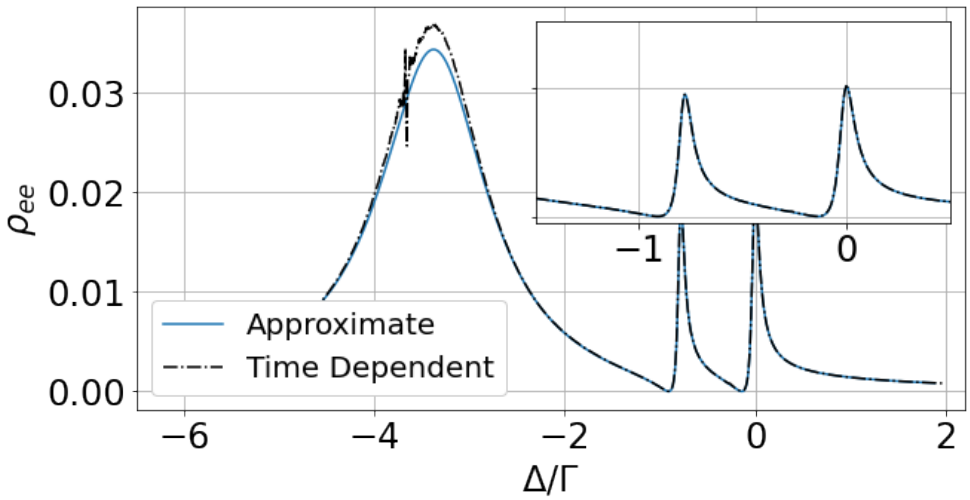

Figure 2.13: Both curves were produced using the parameters in Table 2.4 for 100q/s heat load (Ω_{pump}=34.420MHz, Ω_{probe}=4.5505MHz, δ_{pump}=2.1985MHz, δ_{probe}=9.598MHz). The time dependent code only includes the $P_{1/2}$ — $S_{1/2}$ collapse operator so the approximate code likewise only considers the natural linewidth. External heating does not enter this calculation.

This trick is used for the remaining calculations. After optimizing for ideal parameters the fano-profiles are compared with the time dependent method to confirm accuracy. The difference in compute times is over 10x which makes this approach very worthwhile. Optimizing over the parameter space requires thousands of function calls making the time dependent approach impractical.

2.3.2 EIT Advantages

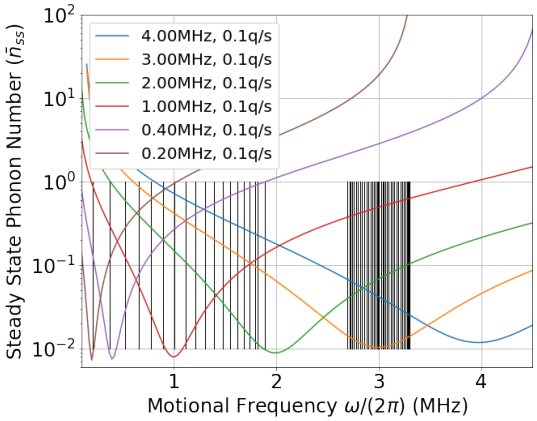

(a) Steady state temperature for EIT configuration. Parameters were chosen to center the cooling power at the listed series of frequencies. Superimposed in black are the motional mode frequencies. Laser linewidths are *not* included in the cooling profiles, and do have a significant effect below ≈2MHz

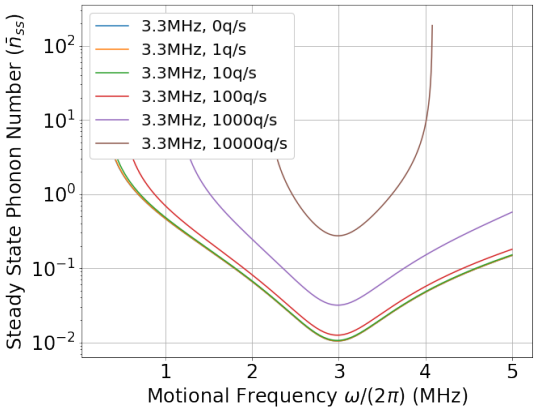

(b) A closer look at the steady state temperature centered at 3.3MHz with increasing heating rate. Laser parameters are Ω_{pump}=35.211MHz, Ω_{probe}=8.459MHz, δ_{pump}=51.837MHz, and δ_{probe}=59.569MHz. 20.1MHz $P_{1/2}$ — $S_{1/2}$ linewidth forms the collapse operator for the Liouvillian.

Figure 2.14

As trapped ion quantum computers have increased in number of qubits, EIT cooling has become more widely investigated and implemented. The reason for this is EIT cooling can cool to the motional ground state while still being a broadband technique. Doppler cooling is broadband, in that it can cool all the motional modes simultaneously, but can not reach the ground state. QRSC is narrow-band, where only a single motional mode is cooled at any given time, but can reach the motional ground state. EIT cooling can both cool multiple modes simultaneously and cool to the ground state. The advantage of

broadband cooling is not readily apparent for a single ion in a trap, but with 20 ions in the trap that can be up to a 40x improvement in cooling times. All of this achieved with only a single set of laser parameters.

This advantage is best shown by scanning the trap frequency with a fixed set of laser parameters, shown in Figure 2.14, where it's clear that for one set of parameters a wide range of trap frequencies reach the ground state. This was repeated for a number of laser parameters each optimized to have the center cooling frequency at the value listed in the legend. As the cooling frequency approaches 0Hz the cooling profile becomes increasingly narrow-band. Compounding this effect is the fact that the axial motional modes begin at the lowest frequency and have the greatest jumps in frequency between modes, spanning the greatest range of frequencies. This is shown as the first set of vertical lines in the plot. For these two reasons EIT does not have significant advantages over RSC for cooling the axial modes.

For the radial modes however the opposite is true. The cooling profile is broadband enough to cool both the X and Y radial directions where the COM frequencies (of X and Y) are offset by ≈300kHz. Here the small frequency steps between adjacent radial modes and the broadening EIT profile work in concert, and that is where a 40x cooling time improvement can be reaped. For 20 ions there are 60 motional modes and cooling 40 of those (the radial set) simultaneously is an advantage that will only become more pronounced as ion numbers increase.

EIT cooling is also remarkably robust against external heating. The radial modes already benefit from lower heating rates since they are higher frequency and require more energy to drive a $n+1$ transition, but even extreme heating rates can be effectively combated by EIT cooling. This is because the engineered transparency allows more power to be put into the cooling beams without worrying about off resonant transitions producing additional heating effects. This is demonstrated by Figure 2.14b which shows the effect of increasing heating rates on the cooling profile centered at 3MHz.

2.3.3 Expected Steady State Temperature

By making the approximation discussed in Section 2.3.1 the steady state temperature can be optimized for, searching through the power and detuning in both laser beams. This 4 variable optimization is not necessary for a three level EIT configuration, but adding an additional level (the three levels in the $S_{1/2}$ manifold) complicates the system and simple closed form analytical expressions which match the simulation are difficult to find.[45][46] The result of the optimization is summarized in Table 2.4.

Heating Rate	Ω_{pump} (MHz)	Ω_{probe} (MHz)	δ_{pump} (MHz)	δ_{probe} (MHz)	$\bar{n}_{ss}$
0.0	35.455	0.071	52.074	59.592	0.113
1.0	34.840	1.421	52.164	59.583	0.118
10.0	34.597	2.536	52.190	59.582	0.129
100.0	34.420	4.550	52.198	59.598	0.165
1000.0	34.431	8.472	52.124	59.641	0.296
10000.0	33.793	17.426	51.506	59.600	0.974

Table 2.4: Optimal parameters found by optimizing power and detuning in both lasers. For this table $\bar{n}_{ss}$ is the average of the all radial modes, so the average of $\langle n \rangle$ for each mode. This simulation includes the expected laser linewidth of ≈500kHz

2.3.4 Expected Cooling Times

As mentioned in Section 2.1 by optimizing in the presence of external heating the found parameters naturally find the optimal cooling *rate* relative to the heating rate. If the cooling rate produces an excessively long cooling time it would be detrimental to running QuantumION experiments in quick succession, however this is not a concern based on the results in Figure 2.15, where cooling times are found to be ≈1ms. RSC achieves better cooling rates, however the technique is employed for the lower energy axial modes and benefits from this. The achieved rate for QRSC at the highest frequency axial mode is significantly slower than for the lowest frequency (see Table 2.3).

2.3.5 Cooling Direction

A quick aside on cooling direction; the EIT cooling direction is equal to the difference of the two cooling laser's k-vectors because EIT cooling is a Raman process[45][19]

$$\eta = \left|\hat{e}_{trap} \cdot (\vec{k}_{pump} - \vec{k}_{probe})\right| \sqrt{\frac{\hbar}{2m\omega_{trap}}}. \tag{2.39}$$

Based on this equation two conclusions were made for the QuantumION system: that there would be insufficient overlap between the EIT cooling direction and the axial direction to effectively cool that direction, and that there would be plenty of overlap with the radial direction.

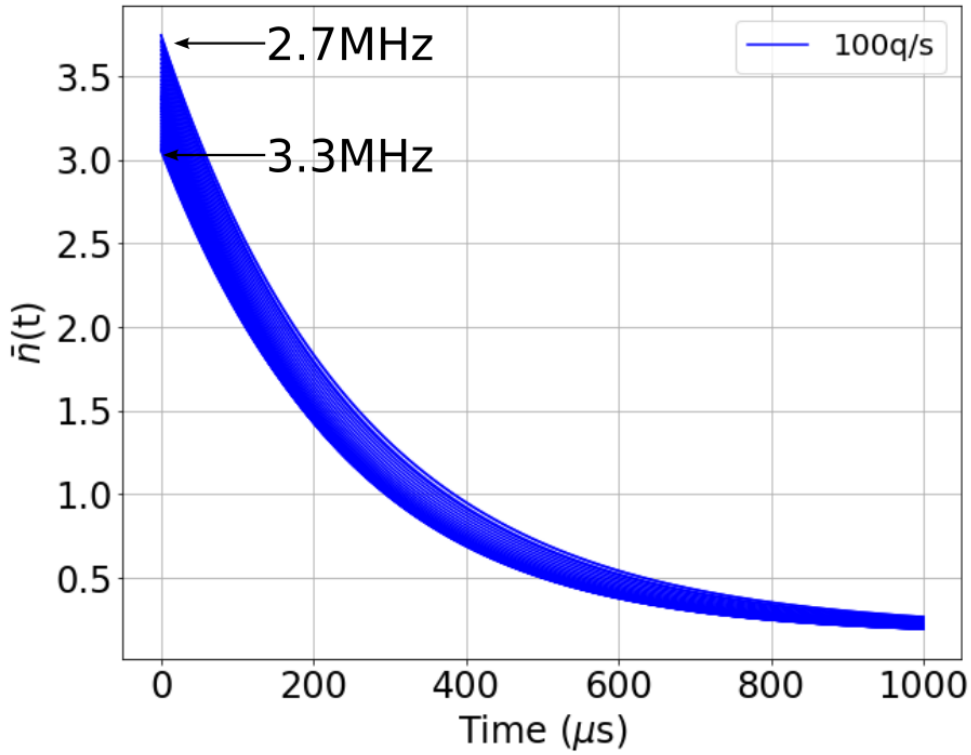

Figure 2.15: Expectation value of number operator for all 40 radial direction motional modes. These span a frequency range from 2.69MHz to 3.30MHz. Laser parameters are from Table 2.4 for 100q/s heat load (Ω_{pump}=34.420MHz, Ω_{probe}=4.5505MHz, δ_{pump}=2.1985MHz, δ_{probe}=9.598MHz). Laser linewidths of 500kHz for both 493nm lasers and 20.1MHz $P_{1/2}$ — $S_{1/2}$ linewidth form the collapse operators for the Liouvillian.

2.3.6 Summary

EIT cooling was investigated for the QuantumION beam configuration. Axial cooling was made impractical by the wide spectrum of the axial modes, and impossible by a lack of overlap with the cooling direction. For the radial direction however an effective approximation to improve computing times was implemented and ideal parameters were calculated. With these parameters ground state cooling was found to be possible for all radial modes simultaneously producing an average phonon number of <0.3 quanta for heating rates between 0 and 1000q/s which spans the range of reasonably expected heating rates. Better figures could be achieved by cooling X and Y separately. This was possible with a single set of laser parameters offering a simpler cooling setup.

Chapter 3

Ion Individual Addressing

A fundamental challenge which all quantum computing architectures must overcome is achieving a scalable way of performing arbitrary quantum operations. It is sufficient to demonstrate a two qubit entangling gate in concert with arbitrary single quibt gates to have a universal quantum computer.[47] Yet even this small set of operations proves a challenge with increasing system sizes. The QuantumION system will perform it's single and two qubit operations through Raman gates, using a pair of 532nm beams from a mode locked laser.[1] By using visible wavelength light to perform these gates it's possible to focus the light onto a single ion in the chain, this way only that ion has it's quantum state affected and individual control is achieved. The challenge in the QuantumION system is then to find a method of controlling the intensity, phase, and frequency of the light field at each ion individually. Since the ions will be spaced 4μm apart this becomes a demanding optical problem. The solution found for the QuantumION system is presented in this chapter.

3.1 Raman Gates Primer

These gates are a two photon process which has been demonstrated in a number of trapped ions systems[48], and state of the art fidelities have been shown for both single qubit and entangling operations.[6] This makes it a reliable and proven approach for QuantumION. The idea behind Raman transitions is to use two lasers to drive a two photon process through an auxiliary energy level. By detuning both lasers far from the excited level the electron will spend negligible time in the excited state and it can be adiabatically eliminated.[49]

Individual addressing is achieved by controlling the intensity profile of one of the two lasers, shining light on the ions to induce an interaction and leaving the rest dark so their quantum state is unaffected. This distinguishes the two lasers into a "global" beam which always illuminates all ions, but is far off resonance for any ion not also illuminated by the second "individual addressing" (IA) beam which performs the ion dependent operations by

[1] Purchased from NKT Photonics.

manipulating the phase, frequency, and intensity of the second laser at each ion. Raman gates fit into the interaction Hamiltonian formalism described in Section 1.2.2 with two major caveats: there is an effective k-vector and effective laser frequency,

$$\vec{k_{eff}} = \vec{k_1} - \vec{k_2}, \quad \text{and} \quad \omega_{eff} = \omega_1 - \omega_2 \tag{3.1}$$

Second that the Rabi-rate is instead defined by:

$$\Omega = \frac{\sqrt{I_1 I_2}}{6\epsilon_0 c\hbar^2}(\hat{e}_1^{\sigma^-}\hat{e}_2^{\sigma^-} - \hat{e}_1^{\sigma^+}\hat{e}_2^{\sigma^+})\frac{\omega_F}{\Delta(\Delta - \omega_F)}\text{Hz} \tag{3.2}$$

where both laser's intensities ($I_1 I_2$), the detuning from the excited state (Δ), and the $P_{1/2}$-splitting (ω_F) are the determining factors for the Rabi-rate. These definitions are further elucidated in Figure 3.1. Finally $\hat{e}_i^k$ is the k polarization component for the i^{th} beam in the ion frame.[41] This is maximized by having the two laser's polarization perpendicular to each-other and to the magnetic field, the so called lin-perp-lin configuration.[2]

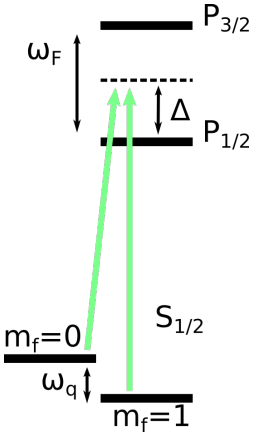

Figure 3.1: Two photon Rabi-rate.

Looking at this equation the Rabi-rate goes as the root of the product of the two beam intensities. This is convenient since the global beam which shines on all the ions can be high intensity for fast Rabi-rates, and the IA beams are free to focus on addressing. Typically the power handling of the IA beams is lower due to the demands of producing N beams each specifically focused on a specific ion.

Any light intended for ion j which spills over to an adjacent ion then has a relative error in Rabi-rate proportional to $\sqrt{I_{j+1}/I_j}$, where the intensity in the global beam is assumed to be uniform so the only cross-talk error comes from the IA beam. Simple calculation shows that an intensity cross-talk of 1% is a 10% Rabi-rate error which would be unacceptable. Modern addressing schemes are able to achieve $<10^{-4}$ intensity error corresponding to 1% rabi-rate errors.[50] This is just at the <1% single qubit error threshold for fault tolerant quantum computing.[51] There are clever tricks which can be applied to minimize the effect of cross-talk errors, but optimizing nominal performance is always preferable to managing an under-performing system. The target for the QuantumION system is to be at or below the 10^{-4} intensity cross-talk figure.

[2] Great appreciation to Frankie Fung, a COOP, who performed these calculations for the barium qubit and generated an indispensable internal document on this topic.

3.2 QuantumION IA Approach

The abstract challenge of high quality control over the n ions in the trap has now been translated into a straightforward optical challenge; Control the intensity, phase, and frequency of a light field at the n ion locations. There are a handful of methods for achieving this the strengths and weaknesses of which are summarized now. The first demonstrated method is using an acousto-optic modulator (AOM) to deflect a single addressing beam between ion locations.[52] This approach has a critical limitation of only being able to address a single ion at a time, precluding simultaneous application of single qubit rotations at multiple ion locations. A marked improvement on this approach is using a single multi-channel AOM, where a single beam is split into n beams and each is fed into the n^{th} channel of the AOM. The AOM provides phase, frequency, and intensity control over each beam.[48] Due to using a single acousto-optic crystal in the multi-channel AOM this approach suffers from high cross-talk.

An alternative method which forgoes using an AOM as the primary control is using a digital micro-mirror device (DMD) to create an arbitrary intensity profile on the ion plane. The DMD can also be used to control the phase profile at the ion plane arbitrarily. This approach has the advantage that non-uniform ion spacing can be corrected for, as can any optical aberrations by applying the opposite phase mask. A drawback is the DMD can not provide an arbitrary frequency profile.[50][53] The major reason for not using a DMD system in QuantumION is the difficulty of control system integration and this approach would be re-visited and re-evaluated for future versions of QuantumION.

The second category of IA control approach is using microwaves instead of visible wavelength light. The qubit transition can be addressed directly using a microwave frequency, and this is a common step in the bring-up of some ion systems. However using far-field microwaves, with for example a microwave horn, can not spatially resolve the ions and so does not have IA capability.[3] This limitation is overcome by using near-field microwaves.[17] This approach was not investigated in detail and is mentioned for completeness.

The QuantumION IA design is a modification of the multi-channel AOM approach which aims to resolve the cross-talk issue. The big picture of how this is achieved is shown in Figure 3.2. Common to most IA methods a single laser beam must be split into n beams where n is the number of ions. In QuantumION this is achieved with a Femtosecond Laser Direct Write (FLDW) wave-guide. This wave-guide provides 1:16 splitting with an additional 1% power tap, all in a passive, path-length matched, and compact package. The output of the FLDW wave-guide is butt coupled into polarization maintaining single mode

[3] Far-field microwaves can not drive sideband transitions either.

fibre. Each of the 16 addressing beams have phase, frequency, and intensity control applied to them through commercial fibre AOMs. The fibre optic cables are then brought back together in another V-Groove Array (VGA). The VGA facet is imaged onto the ions using a Micro-Lens Array and a bulk telescope.

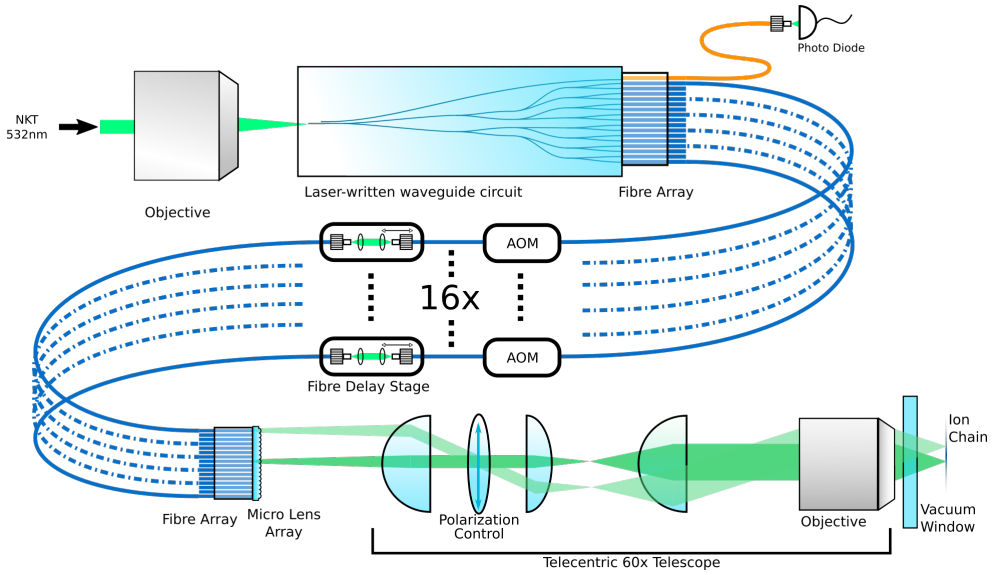

Figure 3.2: Overview of the individual addressing scheme in the QuantumION project.

The remainder of this chapter details the physical constraints which limit the IA design in Section 3.3. These constraints are applied to the idea of using a pitch reducing FLDW wave-guide in place of a micro-lens array (MLA). Which was found to be an inadequate solution for the QuantumION configuration. Section 3.4 then discusses the design of a MLA and IA telescope which meets the requirements of QuantumION. Finally in Section 3.7 the design of the global beam path is discussed.

3.3 Optical Challenge of Individual Addressing

To address each ion individually they must be spatially resolved. So each channel of the VGA must be imaged onto an ion and there must be minimal cross-talk to adjacent channels. These are two separate requirements. The first dictates that the VGA pitch (250μm) must be de-magnified to the ion pitch (4μm in QuantumION).

$$M = \frac{\text{Ion Pitch}}{\text{VGA Pitch}} = \frac{4\mu m}{250\mu m} = 0.016 \tag{3.3}$$

Simultaneously each beam must have a spot size small enough to only illuminate a single ion. This means a beam waist $\lesssim 2/5$ the ion pitch to achieve the target cross-talk based only on the Gaussian beam shape at the ions. So far this calls for a simple telescope which images the fibre facet onto the ions with a magnification that is equal to the ion's pitch over the VGA pitch.

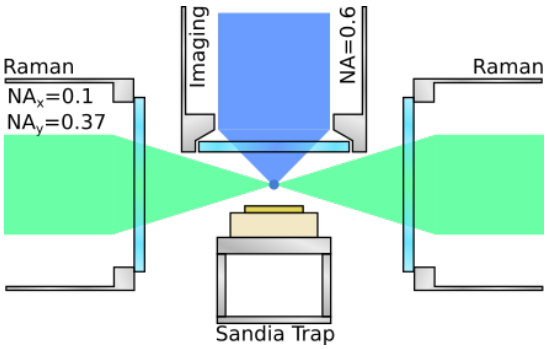

(a) Figure shows the side view of the re-entrant used to bring objectives maximally close to the ions. There are no re-entrants in the axis perpendicular to the page.

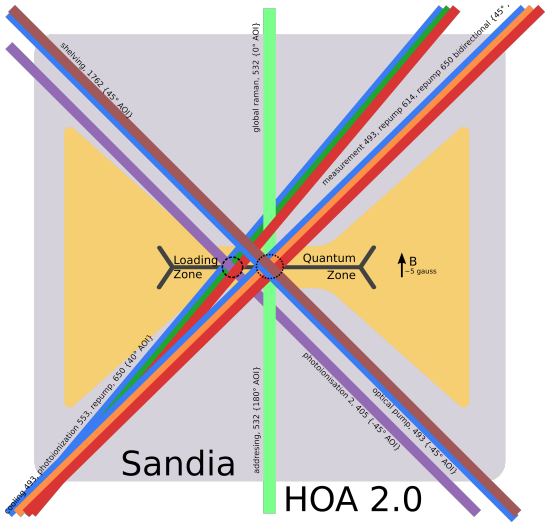

(b) Top view of the Sandia HOA 2.0 trap with all beams showing their location and relative orientation. A major limitation on the achievable NA for the Raman direction is that the 45° beams on either side have to clear. This puts a theoretical limit of 0.79 on the NA.

Figure 3.3

The beam waist at the VGA is set by the fibre core diameter. For single mode PM fibre the mode field diameter (MFD), or twice the beam waist, is 3.3μm. After de-magnification by the bulk telescope to get the correct pitch, the MFD is 53nm at the ions. This is smaller than the ratio needed for cross-talk and the MLA is therefor superfluous?

The missing piece of information is the numerical aperture of the system. This NA is limited by the geometry of the vacuum chamber, re-entrants, and trap with details in Figure 3.3a. The imaging re-entrant collects light for quantum state detection of the ion chain. The fidelity of state readout is strongly dependent on NA so the imaging re-entrant is as close to the ion chain as possible. Optimizing for imaging however means that the

Raman NA is limited by how close the Raman re-entrant can get to the imaging re-entrant safely.

In addition to the imaging re-entrant, the necessity of additional beams at 45° to the trap further limits the NA to a theoretical maximum of 0.79. These additional beams are used for optical pumping, state readout, and cooling. Each of these functions are vital and so the result is that the maximum NA which could be allocated to the IA beam is 0.37. For more on the design of the QuantumION vacuum chamber and to see further the source of this limitation see Noah Greenberg's thesis.[54]

Returning to the 53nm spot size needed to get the correct pitch. The diffraction limited spot size as a function of NA is

$$d = \frac{\lambda}{2NA} = \frac{532nm}{2 * 0.37} \approx 700nm \tag{3.4}$$

so it's clear that attempting to focus each beam down that tightly will naively attempt to make a sub-diffraction limited spot. This is not possible and in earnest what will be observed is a very severe diffraction pattern, with the diffraction fringes contributing to excess cross-talk.

This observation is a consequence of violating the Lagrange invariant for optical systems (ℋ).

$$\begin{aligned} \mathcal{H} &= n(\theta_m h_c - \theta_c h_m) = \theta_m h_c \\ \mathcal{H} &= 0.1 * 250\mu m = 25\mu m \neq .37 * 4\mu m = 1.48\mu m \end{aligned} \tag{3.5}$$

where $h_{c,m}$ is the chief (c) and marginal (m) ray heights and $\theta_{c,m}$ is the chief (c) and marginal (m) ray angles. At the object and image plane the invariant reduces to the product of the NA (θ_m) and the object or image height (h_c). For the definition of marginal and chief ray and some other common optical terms see Appendix D. At the fibre the Lagrange invariant is 25μm while at the ion plane it's 1.48μm. If the system uses less than the full NA of the system there is no problem, an aperture stop in the system can limit the NA to make the invariant at the ions any value smaller than 1.48μm but there is no way to increase the NA. This invariant must be conserved throughout an optical system and can be thought of similar to a conservation of information theorem. The optical system can always degrade, but can't improve beyond what is contained at the object.[55]

So no matter how the optical system is designed, even looking at non-imaging systems in an attempt to scrape out a working system, it's not possible to achieve the desired magnification for the correct pitch and simultaneously having a low cross-talk spot size.

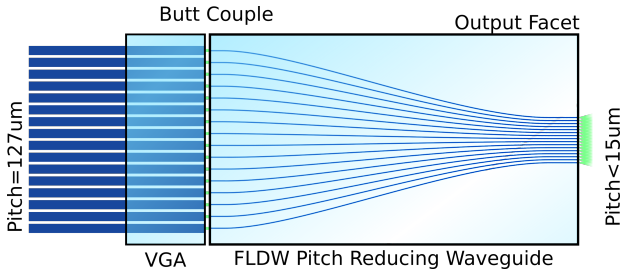

Figure 3.4: Pitch reducing FLDW wave-guide. Extensive simulation was done of the final straight portion, and some simulation was done on the "reducing" portion of wave-guide.

To build a feasible system either the NA or the object height has to be adjusted to comply with the invariant. Re-arranging the invariant it can be shown that reducing the pitch at the object to be $\approx 15\mu$m would bring the system into compliance.

3.3.1 FLDW Wave-guide approach

The NA of the fibre tip is determined by the optical modes which it must support, this is largely set by the core diameter in conventional fibre, which gives the appearance that there is only one free parameter. This is the pitch of the VGA. How close can two adjacent fibres be brought to reduce the invariant? VGA manufacturers[4] offer a variety of pitch dimensions with the smallest being 127μm limited by the diameter of the bare fibre. This is not close enough. Motivated by the expertise already present in the lab developing the FLDW splitter network, a similar device was investigated as a pitch reducing wave-guide. Similar applications of FLDW wave-guides have been demonstrated in a trapped ion context.[56]

A FLDW wave-guide is a created by dragging the focus of a high power pulsed laser through a piece of glass. The power is delivered faster than the glass can thermalize which creates a permanent localized change in refractive index. The achieved change is primarily determined by the composition of the glass and the laser parameters. An optimal index profile creates a similar mode size as a single mode fibre which makes butt coupling into these devices very efficient.

The pitch reducing FLDW wave-guide was simulated in BeamPROP a wave-guide solver from RSoft which solves the Helmholtz equation for a given refractive index geometry

[4]The VGAs in the QuantumION system are purchased from OzOptics. VGA core positions are accurate to 1μm according to the spec sheet, however the measured accuracy of VGAs received from OzOptics has been around 100nm.

and input beam. The critical parameter for accurate simulation was the refractive index contrast and profile achievable. Empirical measurement of these profiles was done by Dr. Matthew Day during his PhD work, where the profile was found to be Gaussian following

$$n(r) = n_0 + \Delta_n e^{-2r^2/a^2} \tag{3.6}$$

where the fitting parameters were found in the course of measurement.[57] The value for n_0 is 1.51872 for 546.706nm light and BK7 glass, $\delta_n = 10^{-3}$, and a=3μm. Matching this profile in beamPROP is key to accurate simulations. In beamPROP the Gaussian index of refraction profile definition differs from the above equation by a factor of two in the exponent. Since matching the profile is so critical a plot was generated to compare the measured and simulated profile which can be seen in Figure 3.5a.

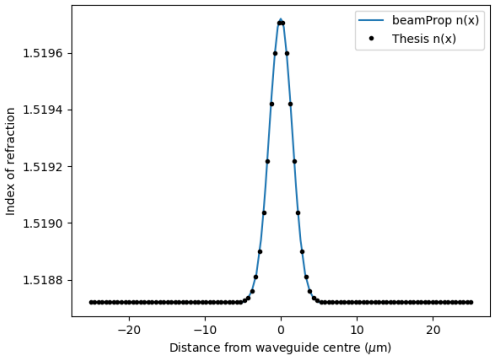

(a) Refractive index profile reconstruction in BeamPROP matching measured data.[57]

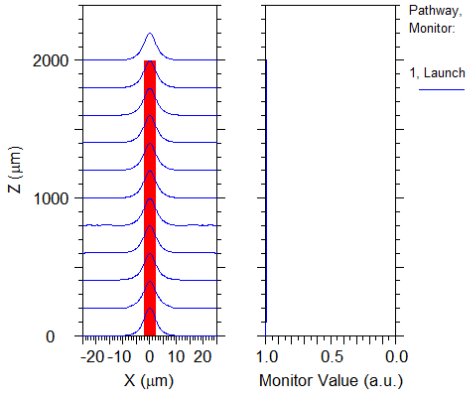

(b) 2mm section of straight FLDW waveguide. Index of refraction follows Equation 3.6. Notice all power is in waveguide 1 (leftmost sub-figure) indicated by the blue trace running vertical along the plot boarder.

Figure 3.5

The first simulation confirms expected behaviour for a single wave-guide, where all power was contained within the wave-guide. Shown in Figure 3.6b. This type of plot shows the wave-guide geometry in red. In this case a 2mm straight wave-guide segment. Plotted on the same axis are periodic slices of beam intensity across the x axis in blue. The y-axis for these slices is not pictured (the pictured y-axis is for the wave-guide geometry) and the units are AU normalized to the starting intensity. On the right there is a plot

which shows the portion of total power in each wave-guide. For this example all power is contained within the single wave-guide making this plot un-eventful.

To characterize the expected cross-talk at a given pitch a series of simulations were conducted changing the pitch for a fixed length of wave-guide. An example simulation at 10μm pitch can be seen in Figure 3.6a. Over the 2mm of pitch there was significant evanescent coupling which led to the power oscillating between the two wave-guides several times. By carefully selecting the length of coupling track this effect is used to produce the evanescent couplers in the splitter network FLDW wave-guide, but in this context this effect is detrimental. Furthermore placing 16 wave-guides adjacent to each other with this pitch would result in the power oscillating all the way across the chip amplifying the cross-talk problem dramatically.

By repeating this two wave-guide simulation for a handfull of different pitches the cross-talk as a function of pitch could be investigated. The main finding was that the coupling had an exponential relationship to the pitch, which is emphasized in Figure 3.6b. For most pitch values investigated the cross-talk is greater than 10^{-4} in intensity however at 15μm pitch with a 250μm straight portion the cross-talk just edges below the target.

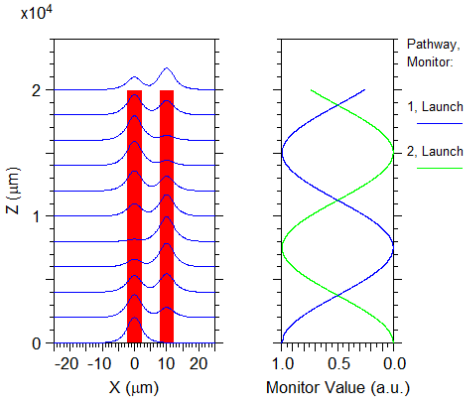

(a) Simulation with two wave-guides 10μm apart which shows significant evanescent coupling between the wave-guides which results in the power oscillating between wave-guides.

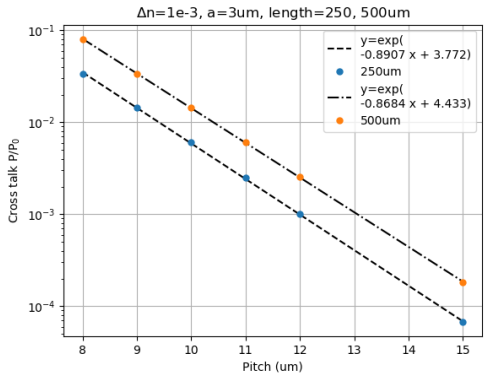

(b) Power cross-talk at an adjacent channel as a function of pitch. The amount of cross-talk is also dependent on the length of wave-guide at a given pitch so two lengths, 250μm and 500μm are plotted.

Figure 3.6

The next step is then to add the pitch reducing portion of wave-guide. This is 16 "S" shaped segments of wave-guide that reduce from 250μm pitch to 15μm. Unfortunately

there is another trade-off here; to keep the length of wave-guide at 15μm pitch as short as possible the pitch should be reduced very rapidly, but doing this leads to sharp bends in the wave-guide which leak light at the bends. Light lost at the bends will either exit the wave-guide as diffuse light, or couple to an adjacent wave-guide. The latter is a source of cross-talk which can't be corrected for. So there is a problem with no solution. Either there will be a lengthy portion of wave-guide at the final pitch, or there will be losses in the bends while reducing the pitch. This point is emphasized in Figure 3.7b where 8 of the 16 channels are simulated and two distinct power loss sections can be observed. One at the reducing stage, and one at the straight portion.

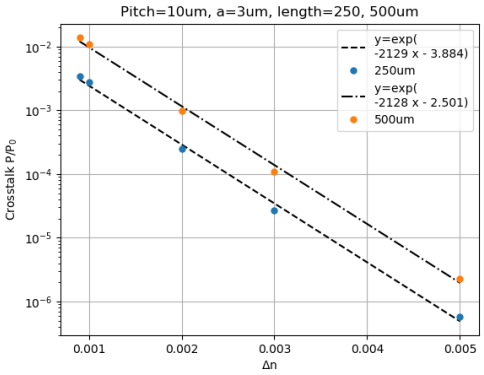

(a) Plot showing the effect of improving refractive index contrast on cross-talk for adjacent wave-guides.

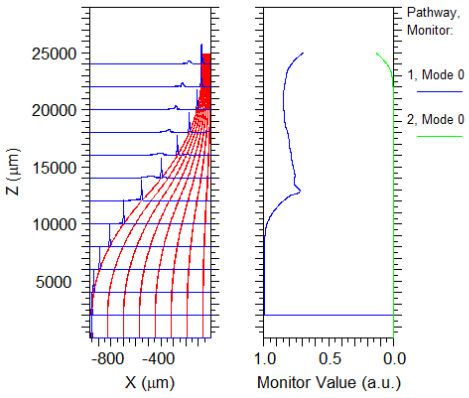

(b) Simulation of half the proposed pitch reducing FLDW wave-guide. There are 8 channels here and for 16 beams it would require mirroring this pattern across the vertical axis. Note there are two zones for power loss; the first is because the wave-guides are brought together too quickly, then the second zone is due to the evanescent coupling discussed above.

Figure 3.7

The last simulation done was to investigate the controls which would enable using a pitch reducing wave-guide. It was found that the refractive index contrast (Δ_n) was the critical parameter limiting the application. Having a greater contrast allows tighter confinement of the light in the wave-guide and subsequently a finer pitch. Developing higher contrast materials is a difficult materials problem and would require extensive research. For reference the effect of improving contrast on cross-talk is shown in Figure 3.7a. Changing

the size of the wave-guide, the a parameter in Equation 3.6, in the absence of improved contrast was found to have negligible improvement in cross-talk.

In conclusion it was found that a pitch reducing FLDW wave-guide which satisfies the optical invariant requirement would itself introduce significant cross-talk. The primary limitation on using this technology was the refractive index contrast achievable.

3.4 Micro-Lens Array Approach

If, as the simulations have born out, it's not possible to bring the two fibre tips close together enough to satisfy the optical invariant then the only other option is to change the NA coming out of the fibre. The actual NA of the fibre can not be changed since it is determined by the core diameter. For a conventional type of single mode PM fibre the NA can be taken as an immovable parameter. Instead a small optical element is placed in front of each fibre tip which affects the fibre NA without changing the pitch. It should be clear that no bulk optic which is placed in front of all of the fibre tips could affect only the fibre NA without changing the pitch simultaneously.

Since the object height for this optic would only be the extent of the fibre tip, the optical invariant for the subsystem comprised of a single fibre tip is different than for the VGA as a whole. In this case the object height is approximately the core radius, just 1.65μm, which makes the optical invariant 165nm, far smaller than the limit at the vacuum chamber (ЖK=1.48μm at vacuum chamber). This is the purpose of the Micro-Lens Array (MLA) in the IA imaging system. It gives a control of the fibre NA which is independent of pitch and allows the optical invariant to be tuned at the input to comply with the limit at the output.

3.4.1 MLA Requirements

Satisfying the optical invariant is just one consideration for the design of this optic. Working through the optical invariant dictates that the MLA should adjust the fibre NA from 0.1 to 0.006 which corresponds to a change in beam waist from 1.65μm to 28.6μm. This is only a ray-optics consideration and a good first check of any system, but all it guarantees is that a sub-diffraction limited spot is not being asked of the optical system. At the diffraction limit there is still significant intensity in diffraction fringes. Given that the invariant is satisfied, a measure of how much intensity is in diffraction fringes would be a

more useful metric. This is because a system can conform to ray optics limitations, resolve a spot of a particular size, and still leak significant power to adjacent ion sites.

To get an estimate for the amount of cross-talk due to diffraction a method based on a paper by Xiao *et al.* was followed.[58] The paper shows how diffraction of a Gaussian beam through an aperture can be calculated by decomposing the beam after the aperture into higher order Gaussian modes. This is similar to how the Huygens–Fresnel principle works however instead of writing the result of diffraction as a decomposition in terms of point light sources it's written in terms of higher order Gaussian modes. The power in all higher order modes can be approximated as the total power save what remains in the g_{00} mode and is calculated by taking the overlap integral between the g_{00} and the pilot beam (which is the g_{00} beam) over the surface defined by the aperture.

$$P_{g_{00}} = \int_0^{2\pi} \int_0^a g_{00}^* g_{00}\ r\ dr d\phi = 1 - e^{-2\left(\frac{a}{\omega(z)}\right)^2} \tag{3.7}$$

where it's abundantly clear that if the integral is taken over all space the overlap is unity and all power continues to be in the g_{00} mode. Here a is the aperture radius, and $\omega(z)$ is the beam waist. If the beam is constrained by a lens, aperture stop, or finite sized window then the overlap is not unity and some power is lost to higher order modes. For this application the exact modes which the light leaks into is not important. Instead this formalism can be used to provide an easy to calculate upper bound on the cross-talk noise due to diffraction by assuming all power not contained in the g_{00} is cross-talk on the adjacent ion. This overestimates the cornstalk but is a useful bound nonetheless.

The optimal IA telescope would maximize transmitted power at all apertures. Usually this is a matter of course; anywhere the beam clips a larger lens should be used. There are two locations where the clear aperture can not be increased. At the vacuum window the geometry is fixed. The magnification of the IA telescope is likewise fixed based on the VGA to ion pitch ratio, which makes the diameter of the MLA a second aperture that can not be increased. The size of the beam at these two locations is linked by the total magnification

$$\omega_{vacuum} = M_s(\omega_{MLA}) = \frac{\lambda}{\pi M_T \omega_{MLA}} f_{ob} \tag{3.8}$$

Since the second aperture is at the vacuum system M_s is the magnification to the viewport, not the total magnification, this parameter is still constrained by the total magnification and objective focal length (f_{ob}) though.

With this relation in mind the total cross-talk from diffraction is the sum of that at

the two apertures,

$$C = e^{-2(\frac{a_1}{\omega_{MLA}})^2} + e^{-2(\frac{a_2}{\omega_{vacuum}})^2} = e^{-2(\frac{a_1}{\omega_{MLA}})^2} + e^{-2(\frac{a_2 \pi M_T \omega_{MLA}}{\lambda f_{ob}})^2} \tag{3.9}$$

where the first term is from the MLA aperture and the second term is from the vacuum aperture. Again there is a trade-off between where the diffraction is minimized. This maps directly to an uncertainty relationship akin to that between position and momentum which is fascinating! But the up-shot is that somewhat unsurprisingly the diffraction-fringes are minimized when the beam waist covers the same ratio of the total aperture at both constrictions.

For the QuantumION system a value of 0.47 for the ratio of beam waist to clear aperture was found. This means that at the objective 47% of the clear aperture (radius) is within a beam waist and likewise at the MLA 47% of the clear aperture is within a beam waist. Therefore the MLA should be designed to magnify the VGA beam waist to 58.8μm. There is some wiggle room here so the target is nominally a beam waist of 60μm. An addendum to this statement is that an ideal Gaussian will have a tail at adjacent ion locations which if the beam is large enough will begin to contribute to cross-talk. Using 60μm as the waist at the MLA leads to a waist of $\approx$1μm at the ions which makes diffraction the primary contributor to cross-talk at the ions.

3.4.2 MLA Design

An aspheric lens was designed to achieve the required magnification in Zemax[5] with simple optimization, where a set of free parameters are given to Zemax and it finds ideal values for these parameters based on a user specified figure of merit (FOM). For the simple optimization the FOM was the output beam waist and minimizing aberrations. A flowchart for simple optimization in Zemax is shown in Figure 3.8a and the result of this optimization is shown in the adjacent figure. For simplicity a single lenslet of the whole MLA was designed then copied 20 times when manufacture was required.

The MLA is manufactured using a high power pulsed laser which writes a pattern into a piece of glass. The extreme power of this laser permanently modifies some properties of the glass which allows selective chemical etching of the material at the locations which have been exposed to the laser. After the MLA is shaped with this technology an optical finish can be made through localized thermal polishing. This technology allows for near arbitrary surface profiles and so an aspheric MLA surface can be designed within the constraints of the technology.

[5]Zemax is a full design suite for optical engineering, it's use is ubiquitous though-out the industry.

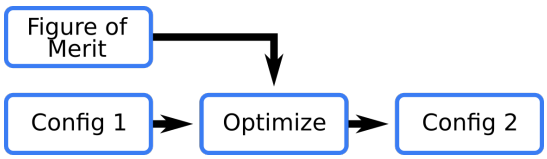

(a) Simple optimization scheme in Zemax where a figure of merit is defined and the initial configuration is optimized with this singular FOM into the final configuration.

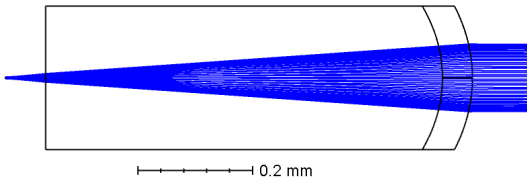

(b) Side view of a single lenslet in the MLA after simple optimization in Zemax.

Figure 3.8

Advanced Optimization

The simple procedure used above is straightforward enough but does not make use of all features Zemax has to offer. A more involved optimization scheme would take into account manufacturing tolerances in both the custom MLA, VGA, commercial optics, and the accuracy to which lenses can be placed. Zemax can test a system through specified tolerances and this is used to characterize the telescopes in isolation in Sections 3.4.3 and 3.7.1. A more sophisticated use of the tolerancing features is to optimize based on the tolerancing results. Doing this finds the configuration which most robustly performs well within the specified tolerances.

The full scheme is then to do simple optimization to a nominal configuration, then optimize over expected manufacturing tolerances to produce a robust final configuration. Figure 3.9 can be used to visualize this process.

To find the MLA profile this tolerancing feature was combined with a custom figure of merit written in the Zemax ZPL macro language. Because ion-ion cross-talk is not a common optical problem Zemax does not have a built in operand for calculating cross-talk. Metrics with surface similarity exist like encircled energy, but these don't do exactly what is needed in one way or another. For example the encircled energy is hard coded to be a circle, which does not work well for elliptical beams, further it has no way to encode that only cross-talk in the ion chain direction is important, and finally it is a ray optics method. The macro would perform a physical optics propagation (POP) analysis and take the greatest intensity outside a box with user definable width and height to be the intensity cross-talk number. The box could then be configured as needed, by making the box fill the whole direction perpendicular to the ion direction considers only the intensity at adjacent

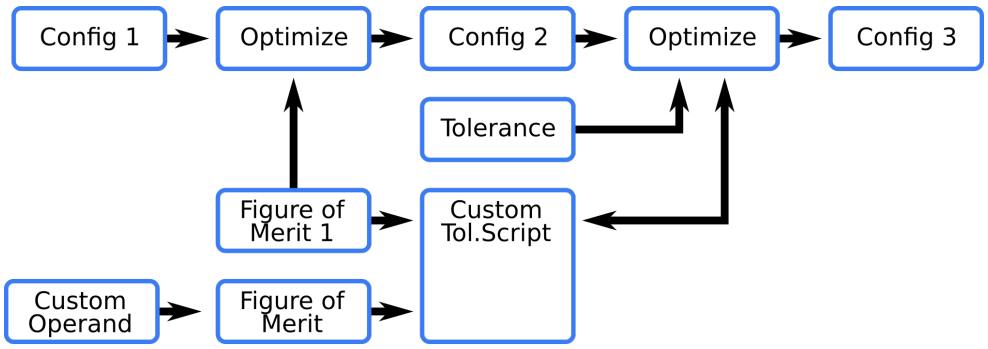

Figure 3.9: Advanced optimization scheme. An initial configuration is optimized with simple optimization to produce Config 2. This nominally optimized configuration is further refined by including tolerancing information and making use of multi-step optimization; where a custom tolerancing script sequentially loads different merit functions and free parameters then performs simple optimization on each new merit function.

ion positions. The only catch is that this figure of merit takes a long time to compute. So a secondary merit function which uses the fast built in methods and no POP was written.

A common way to design complex optical systems for production is to have a technician align the system after assembly in parts, using different feed backs for different sections. For instance fibre coupling an elliptical beam from a laser diode. The technician may first optimize cylindrical beam shaping on a camera, then optimize fibre coupling with a power meter at the output facet. For production an optical engineer using Zemax would like to know if the specified tolerance produces sufficient yield with this procedure. Zemax supports multi-step optimizations using different variables and different figures of merit to simulate this process. This is achieved in a Zemax scripting language, and this was used to quickly optimize the IA system with the fast figure of merit, then measure the system performance using the slow figure of merit. This is what the "Custom Tol. Script" represents in Figure 3.9.

The MLA was optimized for robustness using this multi-step alignment procedure, where the expected tolerances on MLA manufacture and IA telescope were included and the free parameters were all the controls which are built into the IA beam path. The result was not dramatically different from the simple optimization and primarily adjusted the higher order terms in the aspheric surface. Of particular concern and the imputis for this optimization scheme was to determine if the uncertainty in VGA core position would introduce significant aberrations, and it was found to be a non-issue.

3.4.3 The IA Telescope

In addition to minimizing cross-talk by adjusting the object at the VGA with a MLA, there is a bulk telescope which simply images the MLA output onto the ion chain. Aberrations in this telescope would be a primary source of cross-talk at the ion plane. This telescope is shown in Figure 3.10, and provides a 62.5 times de-magnification which set by taking the ratio of the pitch at the fibres to the pitch at the ions (4/250). However as Figure 3.3a shows the NA is not identical in X and Y. This means that while the axis parallel with the ion chain has sufficient NA for ≈1-2μm spot sizes, the direction perpendicular to this does not.

For this reason the IA telescope will have some cylindrical elements in one axis. Since the axis parallel with the ions, the Y axis by convention, is the high performance axis which determines cross-talk the telescope for Y was designed then magnification was adjusted in X with cylindrical lenses.

In addition to providing the correct magnification, the telescope must be telecentric. Technically this means that the chief ray is parallel to the optical axis at either the image or object space. In practice the IA system is "doubly" telecentric because the chief ray is parallel to the optical axis at both the object and image space.[55] By using a VGA where all the cores are parallel a telecentric object space is unavoidable, since the k-vector of the laser beam enters the Hamiltonian for Raman gates it's also useful to have a telecentric image space. There are also ancillary benefits: chief among them that motion in the object space is linearly mapped to motion in the image space. This is a huge boon for alignment since a 6 axis stage at the VGA side can be used to maneuver the IA beams in both angle and position to sub-nanometer accuracy (also aided by the telescope de-magnification). A doubly telecentric optical setup is also a 4f imaging system which gives convenient access to both image an Fourier planes, useful for system characterization. Notice however that the X direction is not quite telecentric. This is not a problem since in the X axis all beams are on-axis and have negligible height, meaning that the question of telecentricity in this axis is more a question of definition than a source of concern.

Zemax Simulation

To confirm this design and pick suitable lenses extensive simulations were done in Zemax of the IA telescope. Root mean squared (RMS) wavefront error as a function of object height (field) is calculated by propagating a grid of rays at each field point and calculating the RMS wavefront error for each point in the field. The wavefront is estimated by the optical path, the length of each ray, and computing the difference between the real length

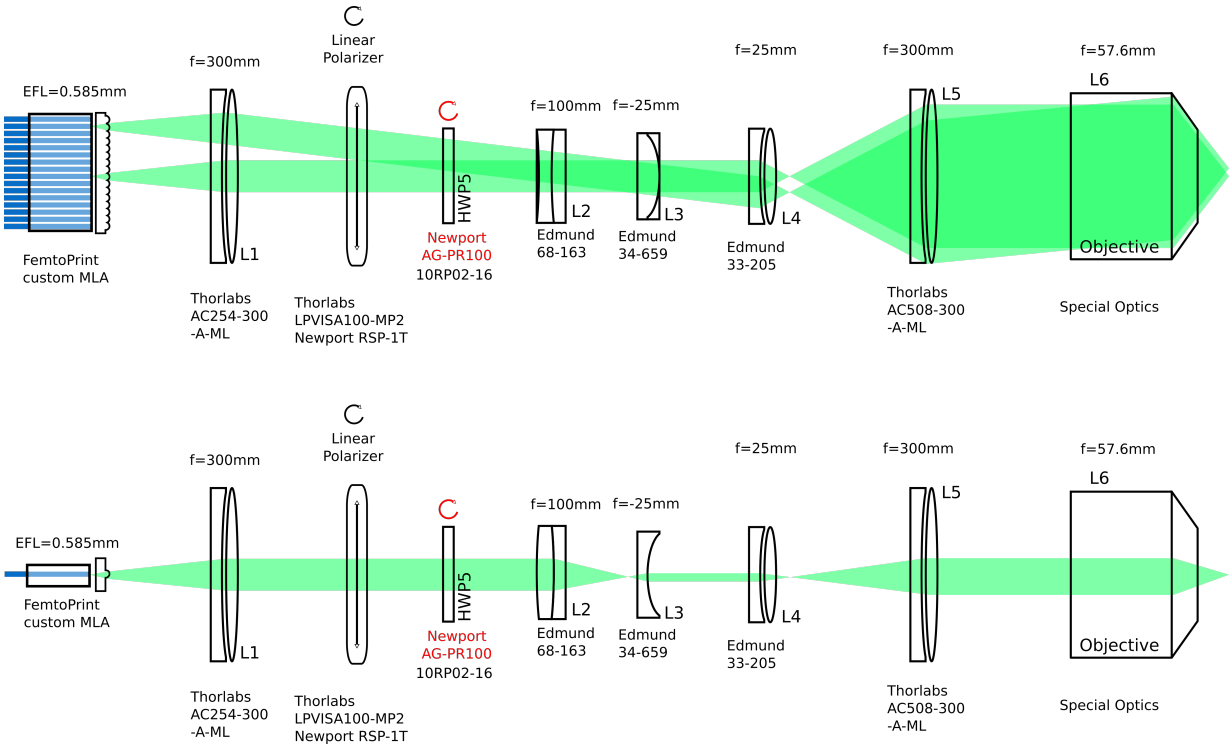

Figure 3.10: Individual addressing telescope with lenses and focal lengths listed.

and a "reference" surface. At the focus, a plane (without curvature) can be used, and at all other points an ideal spherical surface should be used. The RMS error is then the variance of the optical path difference (OPD) for all the rays in the grid.

$$W_{RMS}^2 = \frac{1}{n}\sum_{i=1}^{n} W_i^2 = \frac{1}{n}\sum_{i=1}^{n}(S_0 - S_{real})^2 \tag{3.10}$$

Where W_i is the error for each ray, and can be written as the difference between an "ideal" (S_0) surface and the real wavefront in the simulation (S_{real}). The trick to having an accurate measure of error is to find a good reference surface. This is the value of a software package like Zemax which implements the method described by M. Rimmer to calculate an optimal surface to compare with.[59]

$$W_{RMS}^2 = \sum_{i=1}^{n}\frac{1}{W_n} \times \left(\sum_{i=1}^{n}(W_n^2 \cdot w_n)\right) - \left(\sum_{i=1}^{n}\frac{1}{W_n} \times \sum_{i=1}^{n} W_n \cdot w_n\right)^2 \tag{3.11}$$

Where W_n is the optical path difference at a given point in the pupil and w_n is the weighting at that point in the pupil.

The field error was calculated for twice the necessary field of view (FOV). The simulation shows that the RMS error is less than the diffraction limit for the whole FOV which indicates that the designed telescope will perform adequately. This can be seen in Figure 3.11a. A curve for performance at 532nm and at 493nm is plotted. At the time of design there was an idea of sending 493nm light through the IA optics to allow for both individual addressing and individual readout. This idea proved to be excessive for the first version of QuantumION, but the IA telescope does accommodate this. Largely the performance at 493nm is "for free" since achromatic lenses perform better in terms of aberrations at 532nm making achromats a natural choice independent of any thoughts on 493nm performance. See Appendix E for more on chromatic performance.

In addition to measuring the ideal performance of the telescope, Zemax has a sophisticated tolerancing interface. This is typically used for ensuring adequate yield in mass production, but can be a good indication of which optical elements are prone to cause problems and likelihood of achieving ideal performance. Zemax performs this function by having a range of expected values for any parameter specified then doing a Monte Carlo simulation where a number is picked at random for each of the distributions, applied to the optical system, then the system has it's figure of merit evaluated. In this case the criterion is RMS wavefront error. Of course when assembling the optical system there are controls which are available to minimize aberrations due these tolerances. To account for this prior to calculating the figure of merit Zemax can optionally optimize a set of control parameters.

Every commercial lens had the manufacture specified tolerance on radius of curvature (ROC), thickness, surface tip-tilt, index of refraction, Abbe number, and spherical aberrations applied to it. In addition to the tolerance of the lenses, the positioning of the lenses was toleranced to 0.1mm which is a relatively loose manufacturing tolerance compared to the readily achievable 0.025mm dowel pin placement tolerance. See Chapter 4 for more on building optical systems to a tolerance. The optimization after applying the defects was over the VGA position in five axis, which is available since the VGA will be mounted on a Newport Ultra-Align stage, and inter-lens spacings which will have manual control. The result of tolerancing, pictured in Figure 3.11b, shows that taking account for these real-world considerations it's likely diffraction limited performance will be achieved however there is also a significant number of trials where diffraction limited performance is not achieved.

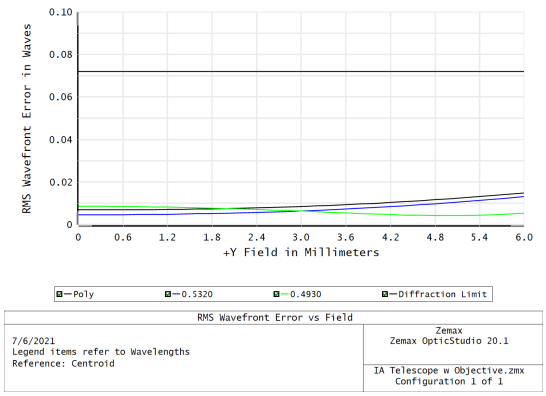

(a) RMS ray error at the ion plane as a function of field for the IA telescope. The VGA is 5mm in total length so the system should be diffraction limited at twice the needed FOV.

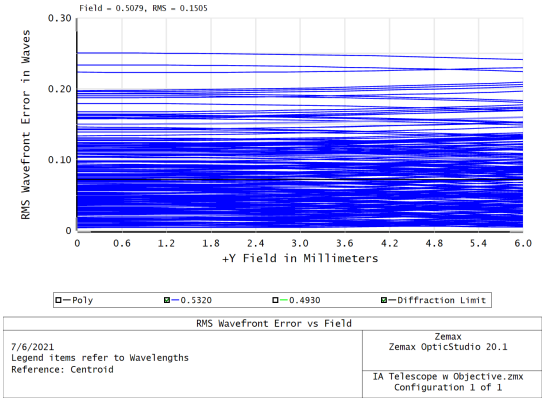

(b) Figure 3.11a with tolerancing results overlaid. The Edmund Optics tolerance preset with precision modifier was applied to the telescope. As well tolerance on lens positioning was added. A representative 200 trials are plotted.

Figure 3.11

To quantify these results into real numbers 8000 trials were run.[6] This is shown in Table 3.1, where in nearly 80% of configurations tested the system was diffraction limited. This shows that both the nominal and on average performance are diffraction limited.

A final benefit from tolerancing is gaining insight into what aspects of the design are most critical. It was found that the final two lenses have the most effect on the RMS error, this makes sense since they're a higher effective NA telescope with larger beams. Unfortunately the aspects which are most critical are inherent to the lenses and can not easily be corrected for: the refractive indices, total thicknesses, and surface aberrations. Note that achromats have more than two surfaces and it was found that errors in any of the surfaces in the final two lenses would contribute most significantly to system performance. This is why L5 and L4 appear twice for the same type of error in Table 3.1.

In addition to ray tracing Zemax is able to perform physical optics propagation (POP) by solving for the propagation of the electromagnetic field. This is achieved through a number of clever tricks. Mainly the software splits the propagation into two regions, in free space and at a surface. In free space the software determines whether diffraction effects

[6]It's recommended for accurate simulation to run $> n^2$ trials where n is the number of parameters being toleranced. This looks daunting but Zemax ran through the trials in a couple minutes.

Nominal	0.00364331
Mean	0.04674426
Std Dev	0.03328354
98%	$<$ 0.12682980
90%	$<$ 0.09486197
80%	$<$ 0.07571799
50%	$<$ 0.04036595
20%	$<$ 0.01546681
10%	$<$ 0.00840576
2%	$<$ 0.00383470

(a) Results of 8000 trials tolerancing the IA telescope. For reference diffraction limited performance would produce an RMS error of 0.072%

Type	Lens
Refractive Index	L5
Refractive Index	L5
Aberration	L5
Aberration	L5
Total Thickness	L4
Total Thickness	L5
Refractive Index	L4
Total Thickness	L5
Aberration	L5
Total Thickness	L4

(b) The most critical dimensions in the tolerance stack for the IA telescope. These sensitivities are calculated by measuring the system change at the extremes of the allowed tolerance. Sensitivity is listed from most to least top to bottom.

Table 3.1

contribute significantly or not and chooses a free space propagation integral based on this. This approach propagates the beam between surfaces. At surfaces the software converts the wavefront into a series of "probing" rays which model how the beam will propagate through the surface. This is a ray based method at the surface. After which free space propagation integrals are again calculated to the next surface. While this method is clearly approximate, it does generally produce accurate results, and, especially important, is well suited to modeling diffraction. So much so that POP can not be used with vendor provided black box files as that would allow customers to re-create the contents of black box files leaking any protected information hidden within.

POP analysis was performed on the full IA beam path including the MLA. The black box file for the objective was replaced with a paraxial lens and aperture. The simulation used the 16^{th} core on the VGA as the launching point. By doing this any aberrations due to the beam being off axis would appear in the final result, shown in Figure 3.12. Pictured is a false color image of the beam intensity and a cross section along the optical axis. Both

show a Gaussian profile with 10^{-5} cross-talk at the adjacent ion position.

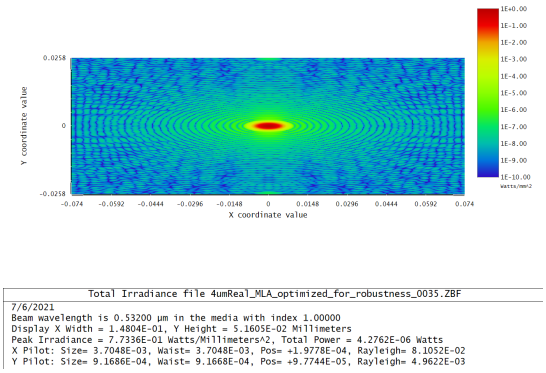

(a) Color-map of a single IA beam intensity at the ion image plane. Figure was produced through POP simulation of the full IA system shown in Figure 3.10

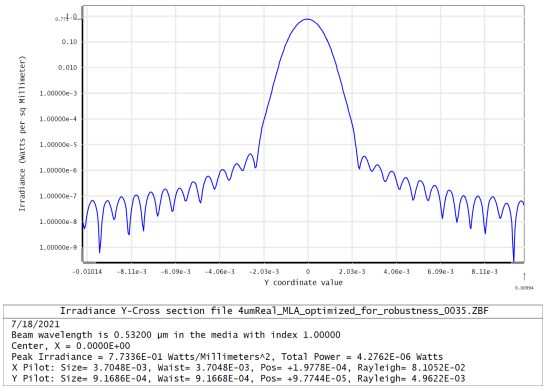

(b) Cross section of Figure 3.12a across the ion axis. Figure shows better than 10^{-5} cross-talk at the adjacent ion position.

Figure 3.12

3.4.4 Summary

A design for optical individual addressing was presented which in POP simulation achieved 10^{-5} intensity cross-talk. This is an order of magnitude better than the target cross-talk figure, and was achieved using a MLA in conjunction with a bulk telescope. The MLA was designed following a sophisticated multi-step optimization. The bulk telescope was characterized in terms of RMS wavefront error across the field of view subject to expected tolerancing of optical components. In the tolerancing simulation the IA telescope performed at the diffraction limit for nearly 80% of trials, with the final two lenses being the most sensitive elements. This performance is suitable for progressing into real-world testing of the system by purchasing the optical elements.

3.5 MLA Characterization

Having spent considerable time optimizing the MLA design a set was manufactured by FEMTOprint. An open question was whether polishing was necessary. This was asked

Figure 3.13: Microscope image of MLA manufactured by FEMTOprint. The left portion shows the polished MLA and the right end shows the unpolished MLA.

since polishing would reduce the accuracy of the printed surface to the benefit of surface finish. To answer this both polished and unpolished were purchased. An image of both is shown in Figure 3.13 and from this first image it looked unlikely that the unpolished lens would have a surface finish sufficient for optical use. However testing was needed to make founded conclusions.

3.5.1 MLA Testing Setup

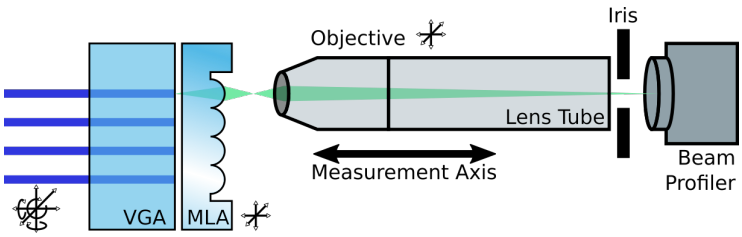

(a) MLA testing setup diagram, in reality the VGA has 16 fibre cores and the MLA has 20 lenslets. At the far left is the VGA which was mounted in a ThorLabs NanoMax NanoPositioning flexture 6 axis stage. The MLA and objective were mounted in ThorLabs 3 axis stages.

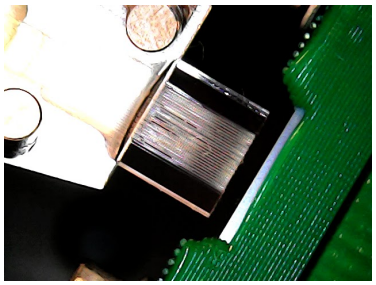

(b) Overhead vision system image of the MLA testing setup. Top left of the figure is the VGA and bottom right is the MLA in a 3D printed holder.

Figure 3.14

To test the MLA performance it was mounted in a 3D printed holder which slotted onto a 3 axis micrometer stage. The VGA was mounted onto a ThorLabs NanoMax 6 axis stage. The alignment of such a small optic is extremely sensitive, however this issue could easily be accounted for by precision placement and permanent epoxying into place (for the final system). Finally an objective which forms an image onto a beam profiler

is mounted into a second 3 axis micrometer stage. This setup is shown as a diagram in Figure 3.14a and an image of the VGA and MLA in their mounting solutions is shown in Figure 3.14b which was taken from the overhead imaging system. The objective and beam profiler have their magnification calibrated by sending light down adjacent cores on the VGA and working out the pixel distance between images of the core. Since VGA cores are placed to tens of nanometer accuracy the magnification can be worked out very accurately by averaging over a number of inter core spacings.

After magnification has been established the MLA can be moved in front of the VGA and a position which has optimal performance searched for. The VGA also provides a Gaussian light source with known beam waist. From this the effect of the MLA on the laser beam can be deduced, any aberrations would be from the MLA. The magnification of the MLA is worked out by scanning the objective position and looking for the smallest waist on the beam profiler.

3.5.2 First MLA

Portions of the polished and unpolished MLAs are shown in Figure 3.13. Both types were loaded into the test setup and characterized. The unpolished MLA was immediately determined to have insufficient surface finish for use in an optical system. This can be seen in Figure 3.15a, where it could be said there is a Gaussian envelope to the intensity profile, but the surface roughness produced a very ugly beam. The polished MLA on the other hand showed promise. At the very least the surface quality was sufficient to produce a mostly Gaussian beam.

To investigate the performance of the polished MLA further high dynamic range (HDR) images were taken at multiple objective Z positions moving through the focus of the beam. The series of images produced are shown in Figure 3.16. The edge of the MLA can be seen in the second sub-figure where the objective is focusing onto the surface of the MLA. The MLA is constrained by the adjacent lenses to have a diameter of 250μm in the ion axis but in the perpendicular axis the lens was made larger at 320μm and it can be seen that the beam does not clip at all in this axis. After exiting the lens, the beam begins to focus and forms a minimum waist at -25thou.

The image formed at the focus is shown again as two cross sections across the X and Y directions in Figure 3.17. From this figure and the Gaussian fit to the data it's clear that the MLA does not have the correct focal length. As well there are significant aberrations. A primary aberration identified is astigmatism where the X and Y directions focus at different depths. The appearance of aberrations are magnified by the logarithmic scale,

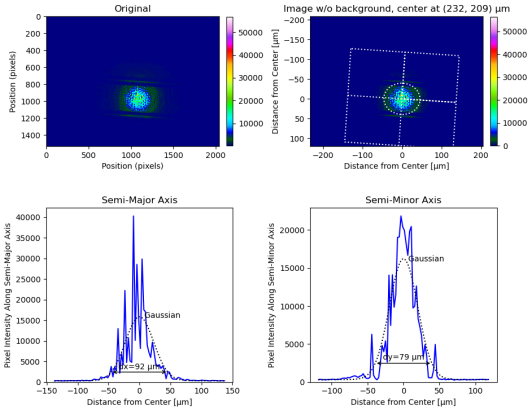

(a) Output of the unpolished MLA pictured in Figure 3.13. Of note is the visible pitting in the surface of the MLA contributing to poor image quality.

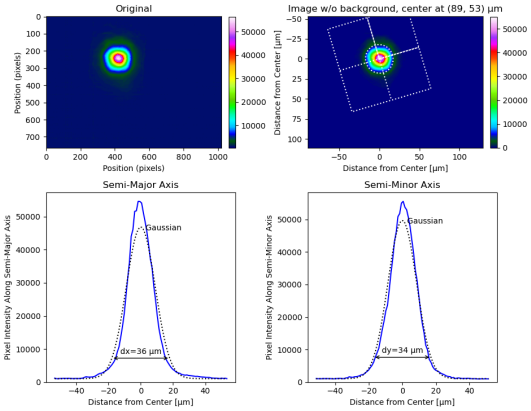

(b) Output of the polished MLA. Alignment has not been optimized for in this image, however the surface finish shows a marked improvement after polishing.

Figure 3.15

and the alignment between the three optical elements was not ideal because the MLA and objective have no tip-tilt control. Looking at how the beam center moves through the series of images it's clear that the objective was not co-linear with the beam. This is a challenge of using a 3D printed holder as the parallelism of the mount is called into question; the optic is so small that printing resolution becomes an issue. Figure 3.15b which has a linear scale was taken on a previous alignment and shows fewer aberrations.

The final and most important issue in these images is that the beam waist at the focus is far too small. The MLA was not able to colimate the light from the fibre at any VGA location, and this observation indicates that the focus of the MLA is recessed into the lens. The surface quality of the polished MLA is suitable but does not match the designed surface profile.

To further investigate the surface profile was measured using a "Bruker Contour Profiler" commercial optical profiler. This is a device which sends a laser beam onto a sample and makes an interference pattern between the reflected light and a reference beam. The interference pattern will be strongly dependent on the shape of the sample, and from this a nanometer accurate surface profile can be reconstructed. The area over which a measurement can be taken in a single shot is just larger than one lens—≈400x600μm—to avoid painstakingly measuring each lens individually the machine has an automatic stitching

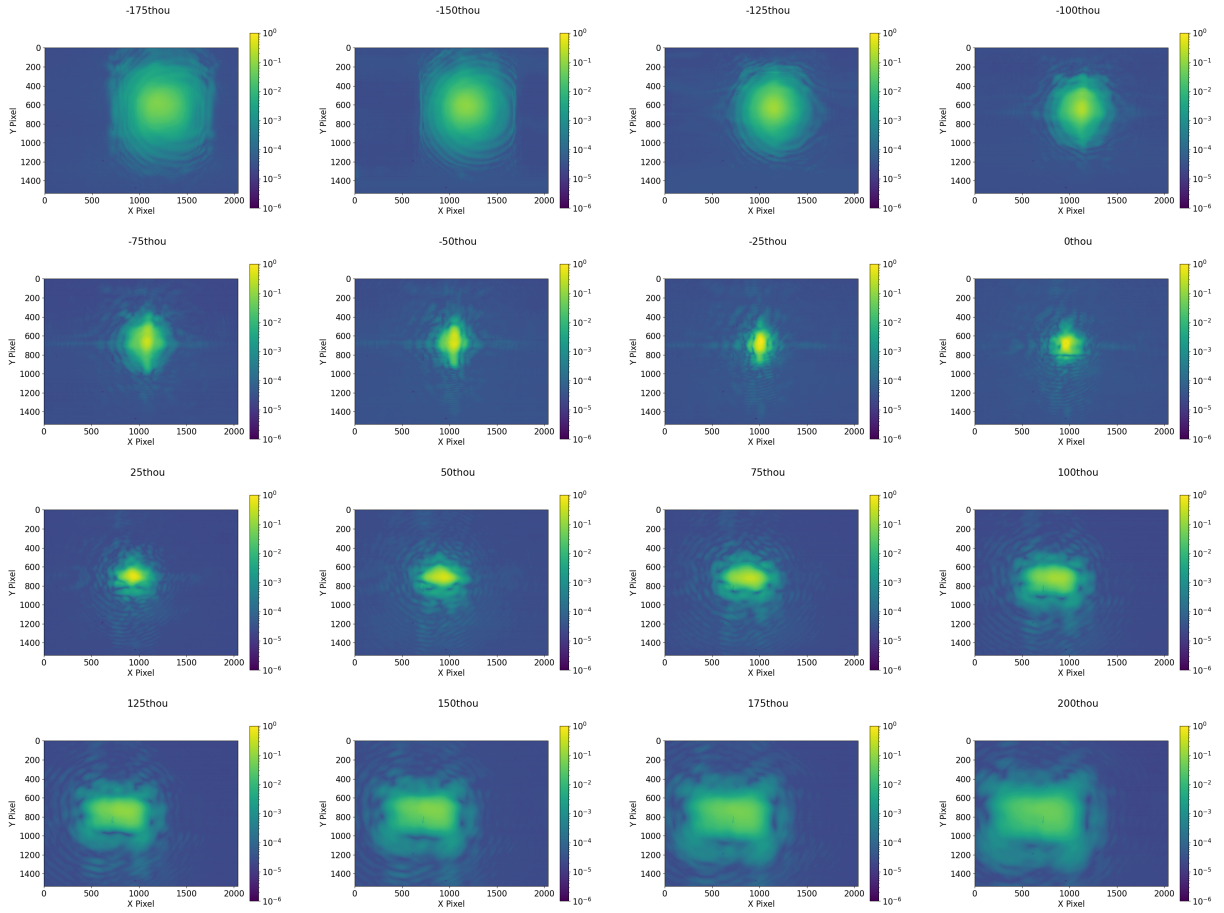

Figure 3.16: A series of HRD images moving through the focus of the MLA output. The Z position of each image is printed at the top of the figure in thousandths of an inch abbreviated as "thou" (1thou = 25.4μm). This data is akin to a PSF however the light source is not a point source. The main aberration visible is astigmatism where the x and y directions form a focus at different locations.

routine which makes a composite of multiple images.

A limitation of the device is the NA of the objective used to image the device under test. The finite NA limits the angles over which reflections will be collected. This meant that the extremities of the lenses could not be profiled. Another limitation is excessively rough surfaces produce a diffuse reflection which can not be used to measure the surface profile. The roughness limitation prevented measurement of the surface profile for the

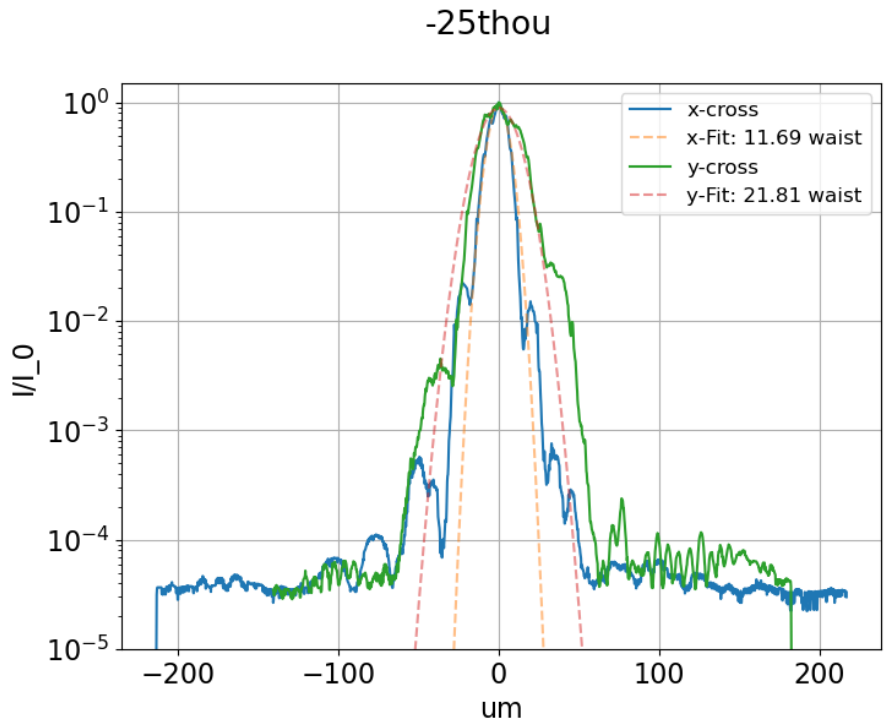

Figure 3.17: Cross section view of image three across two down from Figure 3.16.

unpolished MLA further confirming it's poor optical quality. The angular limitation was not a problem as a large part of the polished MLA was measurable, interestingly the NA was not the same for the horizontal and vertical direction so a larger portion of the lens could be imaged by rotating the MLA.[7]

Direct measurement of the surface profile revealed that both in X and in Y the manufactured lens profile is sharper than the design profile. Another note-able feature is that the two directions do not have the same profile. These measurements explain the observations in the MLA output. Having the lens be sharper than designed is the cause of the smaller than expected output beam waist, and the astigmatism in the measured beam is directly observed in the surface profile of the lens. This result is shown in Figure 3.18a.

It appears that while FEMTOprint was able to produce very near the ideal profile, the demands of the profile in the addressing axis shortened the EFF. This shortening was

[7]The difference between the two directions was noticed after measurement and more data was taken in the other configuration, however not all lenses were re-imaged. See Appendix F for more details.

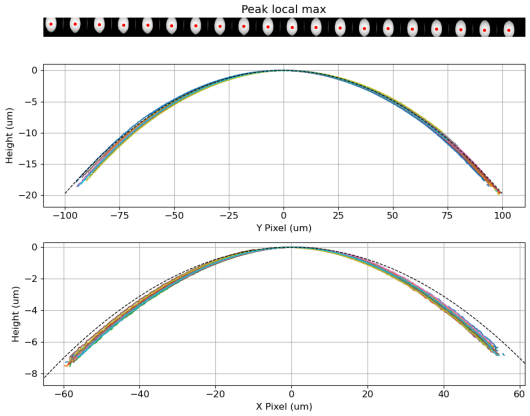

(a) MLA surface profile. In color are all 20 lenslets translated to have the apex of each lens overlap. In black is the analytical form of the intended lens profile.

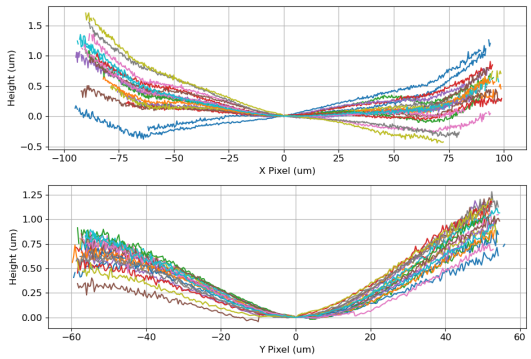

(b) The difference between (intended) design and measured profile for both directions.

Figure 3.18: Optical surface profiler measurement of the MLA. Each lenslet has it's peak located indicated with a red dot, shown in the top left insert. Cross sections were taken along both axis. There is a small tilt across the image since the MLA was aligned to the camera axis by eye without feedback, but this should not dramatically affect the results.

enough to make the MLA ineffective in it's intended role and a second MLA was commissioned. Looking at the difference between the measured and design profiles, Figure 3.18b, it appears that in X the measured profile is primarily tilted from the design profile with some shortening at the extremities. In Y however it's clear that the profile for all lenses is significantly sharper than designed for, with a small tilt contribution. The tilt term could be from the alignment of the MLA in the profiler as the profiler was aligned to the front surface of the MLA which is not a controlled surface in the MLA. FEMTOprint took cake to manufacture the lens in relation to the back surface of the MLA.

3.5.3 Second MLA

Instead of depending on ideal manufacturing the second optic included a series of 20 MLAs with increasing effective focal length. By having a wide range of focal lengths any systematic error in manufacturing could be "calibrated out" and the lens with the ideal profile after shortening would be used for the final configuration. This came out more expensive since effectively 20 MLAs are being manufactured each needing checking and technical

attention at FEMTOprint. To design 20 MLAs a further feature of Zemax was employed. In addition to the interfaces discussed in Section 3.4.2 Zemax offers an API interface which can be accessed through Python (also MATLAB, C, and C++). Through the API MLA profiles were optimized following the same procedure for each. This was done by first setting up the Zemax file in a way that minimal changes were required between lenslets and then performing the minimal changes with the API. Each optimized lenslet was saved as a Zemax file for inspection and as a CAD file appropriate for manipulation in Autodesk Inventor. The 20 lenslets were built out into 20 MLAs and arranged in a way suitable for manufacture in Inventor (also with a little aid from the Inventor API).

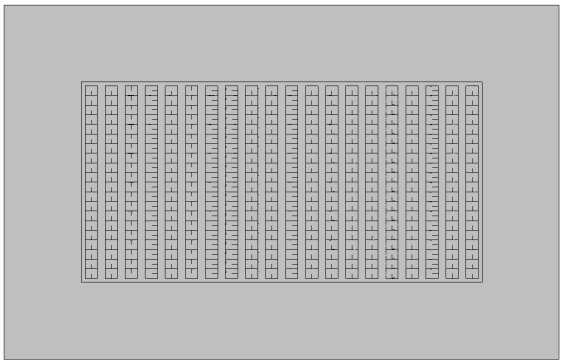

Figure 3.19: Render of the MLA which includes a series of different EFLs which should allow finding a set which has the correct EFL after systematic focal length shortening.

3.6 Summary

The optical demands of a trapped ion IA system were investigated. Application of the optical invariant was used to eliminate the possibility of using a FLDW pitch reducing array as the needed pitch reduction showed significant evanescent coupling between channels in simulation. Instead a MLA was designed to reduce fibre NA. The MLA was designed by optimizing cross-talk due to diffraction fringes and an optimal beam size was found. Using sophisticated optimization in Zemax a MLA profile was designed which in simulation performed excellently achieving 10^{-5} intensity cross-talk.

This profile was manufactured and in practice showed some limitations of the fabrication technique. The manufactured MLA was characterized using direct measurement

of the output beam and with an optical profiler, both measurements confirmed that the manufactured optic had a shorter focal length than designed for along the key axis. To account for this a series of MLAs with increasing focal lengths were commissioned which should allow systematic errors to be overcome by post-selecting a lens.

3.7 Global Beam Telescope

The global telescope is far less demanding than the IA telescope. While the latter has to resolve individual ions with a 2μm spot size the former simply has to evenly illuminate all ions. A flat-top beam is challenging to produce from a Gaussian beam so instead a very broad Gaussian will be used to achieve the target intensity "flatness". For a Gaussian beam with k vector perpendicular to an ion chain the intensity mismatch between the center pair of ions and the outer-most pair of ions is given by

$$P_r = \frac{I(x_{16}, \omega)}{I(x_8, \omega)} = e^{-2\frac{x_{16}^2 - x_8^2}{\omega^2}} \tag{3.12}$$

This formula can be re-arranged to solve for the beam waist needed to achieve any mismatch,

$$\omega^2 = \frac{2(x_{16}^2 - x_8^2)}{\ln(1/P_r)} \tag{3.13}$$

where P_r is the intensity error, x_r is the distance to the r$^{\text{th}}$ ion, and ω is the beam waist.

Simultaneously the beam can not be too wide because the QuantumION system will take full advantage of the Sandia trap by sectioning it into three zones. There is a loading zone where atom photo-ionization, trapping, and initial cooling will take place. It's preferable to do the trapping separate from the quantum zone as this location will be bombarded by the atomic source and can become dirty, contributing to external heating rates.[33] At the trap center there is the quantum zone where experiments will be conducted, and finally there is a memory zone where ions can be shuttled to seek refuge from all lasers. Figure 3.20 shows these zones and their relative locations. To maintain the distinction between these zones the global beam should not have significant intensity at 1mm away from the quantum zone.

To give an idea of scale a handful of values are listed in Table 3.2. Since intensity mismatches can be corrected in the IA beams with a straightforward calibration a 4% mismatch between center and outer ion is tolerable. This freedom allowed choosing lenses from the limited selection of commercially available cylindrical lenses.

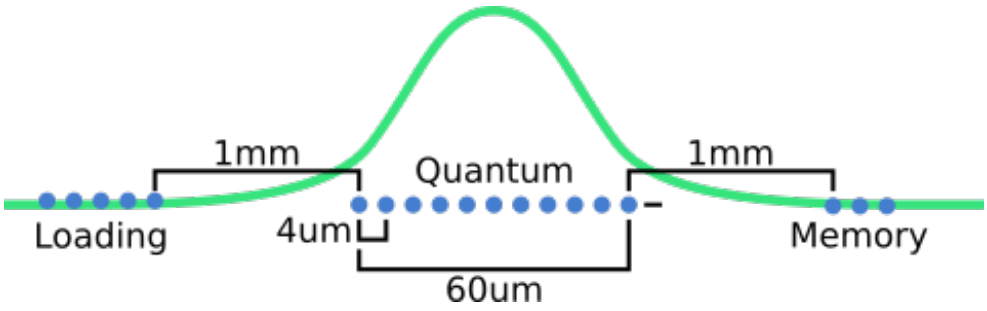

Figure 3.20: The three zones in the QuantumION trap. The loading and quantum zones are fixed at 1mm separation since optics have been designed specifically with this spacing in mind. The "memory" zone is an arbitrary distance away but would have to be at *least* 1mm away to avoid the tail of various beams.

ω (μm)	I(32μm)/I(2μm)	I(1000μm)/I(0μm)
187	0.95	1.45e-25
243	0.97	1.95e-15
422	0.99	1.33e-5

Table 3.2

A telescope which achieves the target magnification was designed and is shown in Figure 3.21. This design was chosen based on being the most compact option using only commercial lenses. The idea is to have two cylindrical telescopes each off-set from one another to produce the correct beam waist at the trap in each direction. In this configuration the expected intensity mismatch would be 3.7%.

3.7.1 Zemax Simulation

The design was again validated in Zemax. In this case there is only one field because there is only one beam which makes a FOV analysis inconsequential. Instead the modulation transfer function (MTF) is used as the figure of merit. An optical system can be fully characterized by how a point light source propagates through the system. This is the point spread function (PSF), and it's intuitive that the way an arbitrary object looks at the image plane is the convolution of the PSF with the object. The intuition is that any object is a collection of points and so how the object propagates is determined by some combination of how a point propagates scaled by the full object. Convolutions are

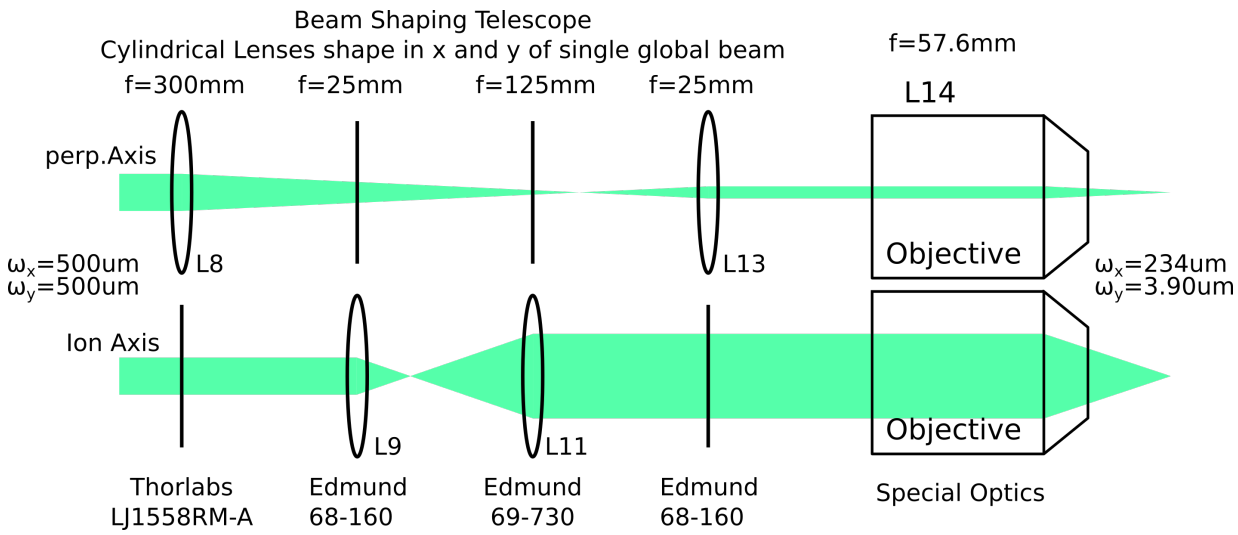

Figure 3.21: QuantumION global telescope. Two cylindrical telescopes are interleaved with one another to save space, both telescopes are 2f away from the objective making a telecentric imaging setup. The object plane in each axis is shifted by 50mm from one another.

computationally expensive, so in signal processing it's useful to move to the frequency domain where convolutions can be written as multiplications.[8] The modulation transfer function (MTF) is just the Fourier transform of the PSF and can equally be used to determine how light propagates through the system.[60]

A more intuitive understanding of the MTF is that it is a function which describes how different spatial frequencies at the object plane propagate through the system to the image plane. This can be measured by imaging regularly spaced lines of different spacings through the system effectively measuring how these different spatial frequencies propagate through. Then any image can be decomposed by Fourier transform into a series of frequencies and amplitudes which propagate according to the MTF.

Figure 3.22a shows the MTF in the ion chain and perpendicular directions for the global telescope. Since the two directions have different NA they have different MTF curves, in all cases it looks like the beam should propagate sufficiently well. The diffraction limited MTF has a cutoff around 160mm so the performance is not dramatically diminished despite tolerancing.

To investigate why the MTF is changing through a tolerancing run it's instructive

[8] As described by the convolution theorem.

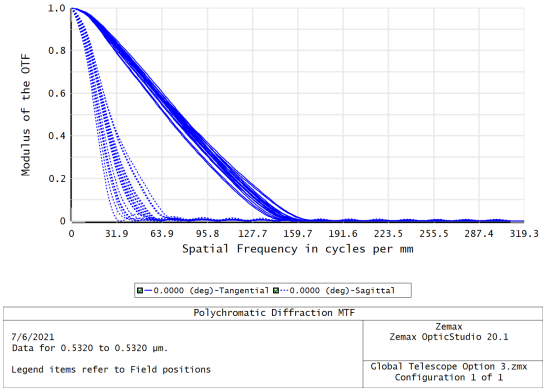

(a) Modulation transfer function calculated using a Huygen's direct integration algorithm. Superimposed are 20 curves which are representative of the tolerancing on the global telescope.

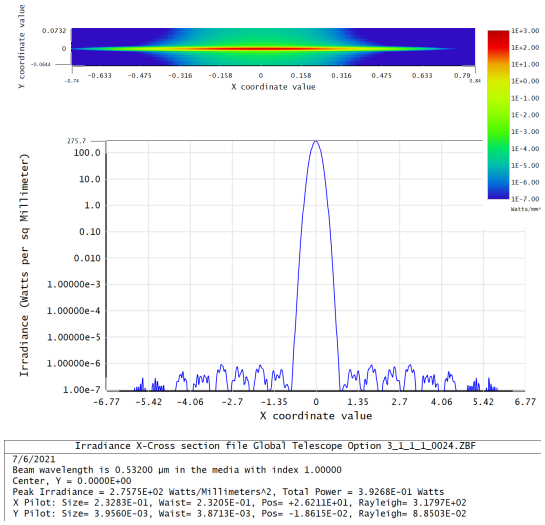

(b) POP simulation of the global telescope. At the top is the false color image of the beam and at the bottom is a cross section along the ion chain.

Figure 3.22: Zemax analysis of the optical system shown in Figure 3.21.

to look at which aberrations are being introduced. Checking the optical path difference (OPD) for the beam is a suitable way to gauge if any major aberrations are being excited. An ideal OPD plot would be a flat line through the origin, which corresponds to a flat phase front at the ion chain. Deviations from this are aberrations and the functional form of the aberrations gives insight into which type dominates.

For the global telescope it was found that without any compensators the dominant term was defocus. This is an easy to fix aberration, the beam is just out of focus. Adding a compensator for focus produced a plot where the dominant terms were comma and to a lesser extent spherical aberrations. Results with and without compensator can be seen in Figures 3.23a and 3.23b respectively. With compensator the error across the pupil is less than $\lambda/10$ in the perpendicular direction, and even better along the ion chain. This indicates aberrations will not significantly contribute to intensity miss-match and is adequate for the application.

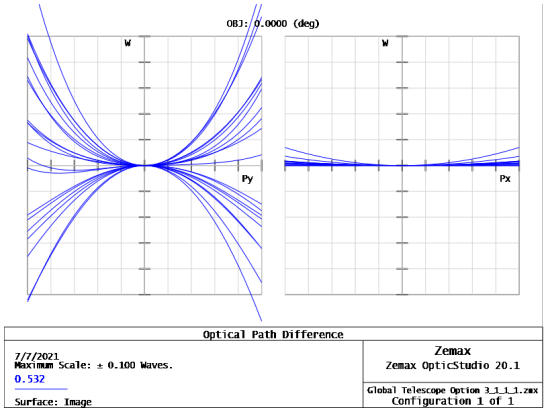

(a) OPD plot across the pupil in both axis. This plot shows the optical path length in wavelengths (532nm) for rays launched from every point across the entrance pupil.

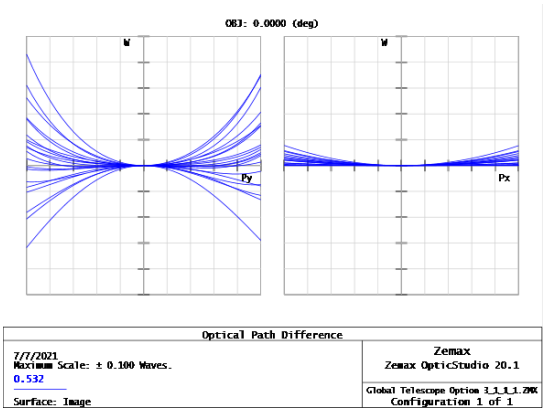

(b) Same as adjacent figure with focus corrections enabled. notice the x^2 terms are diminished.

Figure 3.23: OPD analysis of the optical system shown in Figure 3.21.

3.7.2 Summary

A compact telescope was designed for imaging the global Raman laser beam onto the ions. The telescope had the appropriate magnification along both axis, shrinking perpendicular to the ions and expanding along the ion chain. The intensity mismatch between center and outer-most ions was characterized and found to be appropriate. Lastly the design was toleranced by investigating the effect on MTF and OPD with both showing the telescope was likely to perform to specification.

Chapter 4

Optical Pegboards

For the experimental portion of the QuantumION vacuum chamber there are 10 available ports. One is an electrical feedthrough, one is the pumping feedthrough, and the remaining 8 are being used for laser viewports. There are around a dozen beam paths which have to be designed and built, each with up to a hundred optical components. For the full system to come together harmoniously there must be an overarching design philosophy which guides decisions. The following section describes the QuantumION design approach and the subsequent section shows implementation of the QuantumION approach.

4.1 Design Approach

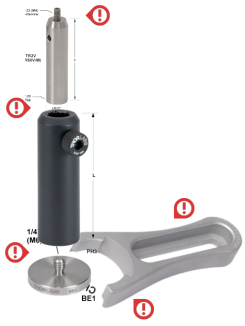

Figure 4.1: Sub-optimal mounting with 5 points of failure

There are two guiding principles used in QuantumION for designing the opto-mechanical assemblies. The first is to remove points of failure, and the second to reference all optical components. Simply applying these principles to a conventional post-mounted optical setup produces the pegboard approach. The conventional method of building a beam path would be to use optical posts which sit in post holders, and are clamped to the optics table using a clamping fork, pictured in Figure 4.1. The issue with this approach is that there can be up to 5 connecting points between the table and the optic. This dramatically increases the points of failure, and makes it impossible to reference one optic to another. Using optical pedestals is an improvement with 3 points of failure, but is still difficult to reference.

In QuantumION the approach is to straightforwardly eliminate the post, holder, and clamping fork assembly. Instead mounting the optic directly onto an aluminium board. This board houses all the optics for a section of beam path. There is now only one point of failure for mounting the optic, and by using precision dowel

pins a mirror mount can be placed to 1 thousandth of an inch accuracy.[1] This is the pegboard approach; CAD up all the components to work out the nominally correct positions, design in needed adjustment controls, then have the pegboard machined.

The advantages of this approach are primarily improved robustness and reduced assembly time. A solid block of aluminium is remarkably stable and this is transferred to the optical system when optics are mounted directly onto the block. Having known intended locations for each of the optical components and dowel pins which the optics can slot into makes initial assembly straightforward; components just slot into their intended spots. The accuracy of optic placement also makes control system integration easier. Especially the fibre optic coupling feedback loop requires knowledge of the 3D positions of the fibre coupling mirrors[2] and this information would be hard to measure in a post-mounted approach but for the pegboard approach it can just be read off the CAD. Finally the pegboards are far more space efficient. This last point will be hammered home by the built pegboard discussed in the following section.

There are also some drawbacks to the pegboard approach; primarily design time and in-flexibility. Making an accurate model of the beam path in CAD and transferring this into a hole pattern on a pegboard by hand is quite tedious. The Quantum Information with Trapped Ions (QITI) group also supervised by Professor Islam is working on generating pegboards pragmatically but for the time being all the QuantumION boards are being hand designed and this is a significant time investment. The in-flexibility comes from having every component only be able to mount in one location. Any mistakes in CAD will require costly and time consuming re-machining of the board, as will modifying the beam path even with relatively simple changes.

Minimizing Points of Failure

The benefit of removing points of failure is quantified in this section. It's not uncommon during assembly of a conventional optical system to miss tightening one bolt and find a component has "dropped" out of the beam path unexpectedly requiring considerable time re-aligning it into the system. By reducing the points of failure robustness is dramatically improved. The correct mounting of a joint can be modeled as an independent event with some likelihood,

$$P_{total} = p^n \tag{4.1}$$

[1] The Polaris series from ThorLabs are the mount of choice since they have dowel pin holes for this purpose.

[2] The fibre coupling feedback controller is a Multiple Input Multiple Output (MIMO) controller which incorporates a model of beam propagation necessitating knowledge of mirror positions.

where n is the number of parts and the total likelihood of having a successful assembly is the probability of a single success raised to the number of joints. By reducing n in design the total likelihood of having an error is improved by the reduction achieved. The absolute worst mounting approach used in some labs has 5 points of failure, see Figure 4.1, which corresponds to a 1/5th improvement in points of failure when using pegboards,

$$\frac{P_{pegboard}}{P_{post}} = \frac{p^{n/5}}{p^n} = p^{-4n/5} \tag{4.2}$$

thus it's clear that as system size grows the benefit of the pegboard approach is emphasized. There are no estimates for the failure rate of properly clamping all the elements in a beam path, however since every graduate student seems to have an anecdote about a mirror mount falling into the post holder requiring re-alignment it's clear that the rate isn't so small as to make this improvement inconsequential.

4.2 1107nm Laser Pegboard

To design a beam path from scratch a standardized procedure is followed. First the intended function of a beam is described. This one-line application is broken into a series of functional blocks, the needed blocks are informed by the application. These blocks are nice because the pattern can be re-used across laser beams and the controls team finds it easier to design variations on a theme rather than totally unique feedback loops each time. The functional blocks are then broken out further into specific parts which is where the details get fleshed out. Correct anti-reflective coatings, lenses, mirrors, etc. and this is what defines the specifics of each beam path.

As an example consider the first pegboard in the 553nm beam path. The light source is an 1107nm cat-eye configuration diode laser from MogLabs which is frequency doubled to 553nm. The top-level function is to provide 553nm light in fibre to the optical table.[3] The functional blocks are then the laser head, diode health monitoring, coarse power control, and fibre coupling. In fibre there are additional elements for controlling power, phase, and frequency using AOMs/EOMs. See Figure 4.2 for the functional blocks as diagrams in the laser rack drawer. Next real components are chosen and the full optical schematic with part numbers for optics and mounts can be made, see Figure 4.3. These parts are built up as a CAD model and the pegboard is designed off of the CAD model, shown after construction

[3] 553nm is used for photo-ionizing barium atoms. However the length of an example detailing all the functional blocks for this application would work against providing clarification of the method.

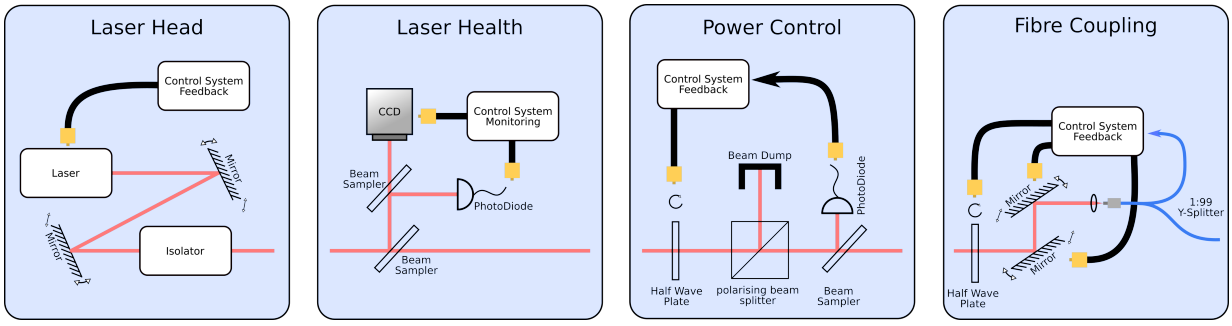

Figure 4.2: Block diagram showing the key functions for fibre coupling a laser head. From left to right there is the laser head which is operated by the control system. Next is monitoring the laser health, both the power over time and the mode quality. Next there is a power control section with active feedback. This section uses a half wave-plate to vary the amount of power which is dumped vs transmitted providing coarse power control for the whole system. Finally on the far right there is the fibre coupling setup which allows easy routing from the rack to the table and the use of fibre EOM and AOM (housed in a different laser rack drawer).

in Figure 4.4. There are three other wavelengths that need the same pre-conditioning and fibre coupling so the same functional blocks are used for all wavelengths differing in the specific part numbers.

All the functional blocks can be seen in the detailed schematic. First the laser head has some input alignment mirrors, isolator, and cylindrical beam shaping with the latter two provided by MogLabs. Next the monitoring section samples some light to keep a constant eye on laser health. The coarse power control is done in a standard way, this functional block is repeated about a dozen times throughout the QuantumION schematics. Lastly the fibre coupling block which additionally has a quadrant photo diode (QPD) to provide additional information to the MIMO controller.

The manufactured pegboard for the 1107nm laser is the second manufactured version of a laser pegboard. The first version while still in use to couple laser light for testing would not work in the final configuration since the MogLabs provided CAD model of the laser did not match the real laser. As a result the laser beam missed the first alignment mirrors which forced mounting the laser separate from the pegboard which is not an option in the final configuration. The second version however is an improvement in space and has large mirrors for catching light out of the laser beyond what the CAD indicates would be sufficient.

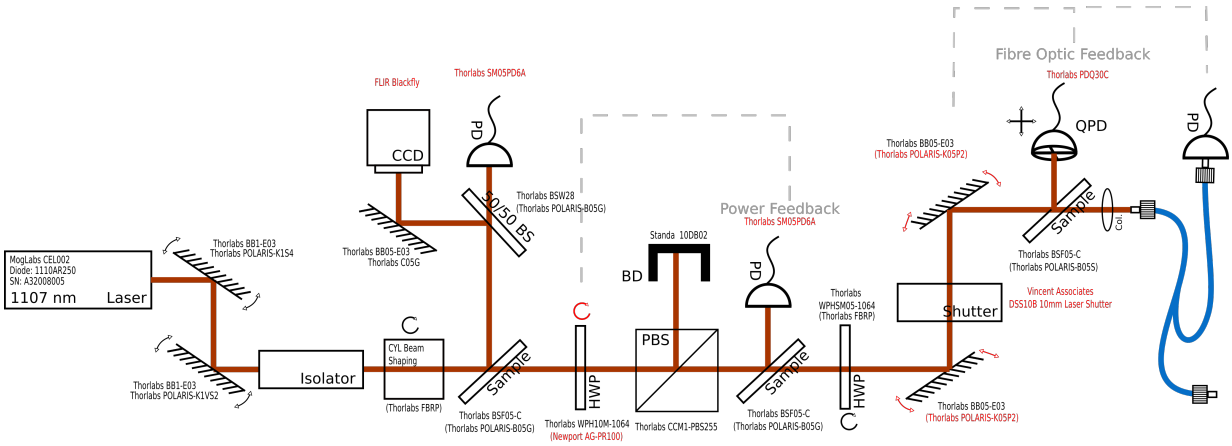

Figure 4.3: Detailed optical schematic of the 1107nm Laser pegboard. Note that most components have part numbers specified. Red labels are parts which interact with the control system, feedback loops are dashed grey lines, while black labels are static.

The reduction in pegboard size was reaped by making full use of the three dimensional freedom of the pegboard. The laser health monitoring functional block is rotated along the optical axis by 10° which gives just enough clearance for the fibre optic cable. Testing was done on the stability of this pegboard. Due to the preliminary nature of these tests they are only summarized in Appendix G, but all tests look promising, and the 1107nm pegboard is being used for conducting ablation testing experiments at this moment without any issue.

4.2.1 Laser Drawer

The drive to make the laser pegboards maximally compact comes from the intention to house four laser pegboards in a single 19" rack drawer. By using a pegboard design which takes full advantage of the vertical and even horizontal direction four pegboards can fit into a single drawer. This is shown in Figure 4.5. Also the optics are made robust enough to take off of the optics table where space is at a premium. Approaches like this are becoming more common as experiments begin to scale to many ions requiring many lasers. See the paper by Pogorelov *et al.* for excellent concurrent work demonstrating the trajectory of the optics rack approach.[61]

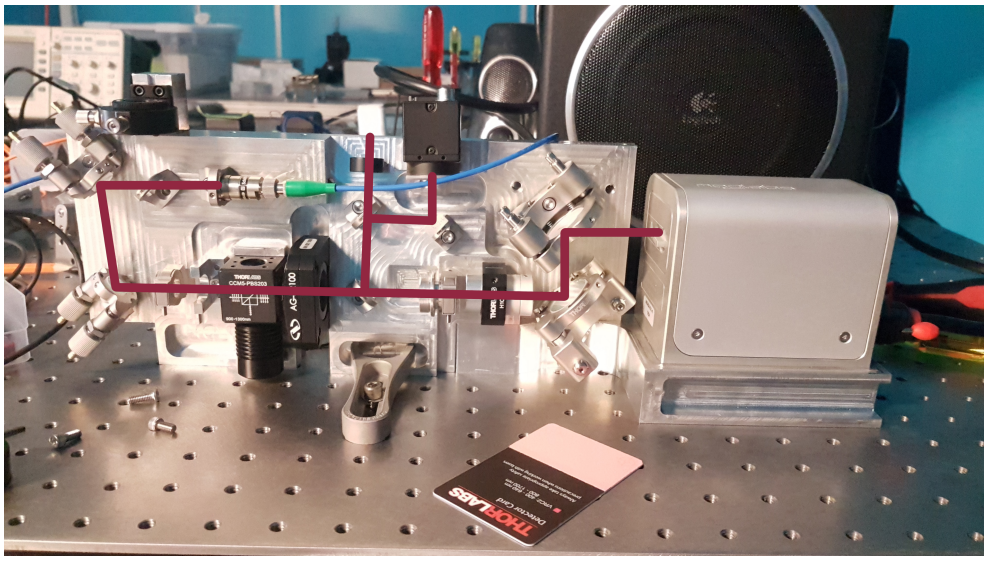

Figure 4.4: Manufactured 1107nm fibre coupling pegboard with optical components mounted. Overlaid is the primary beam path.

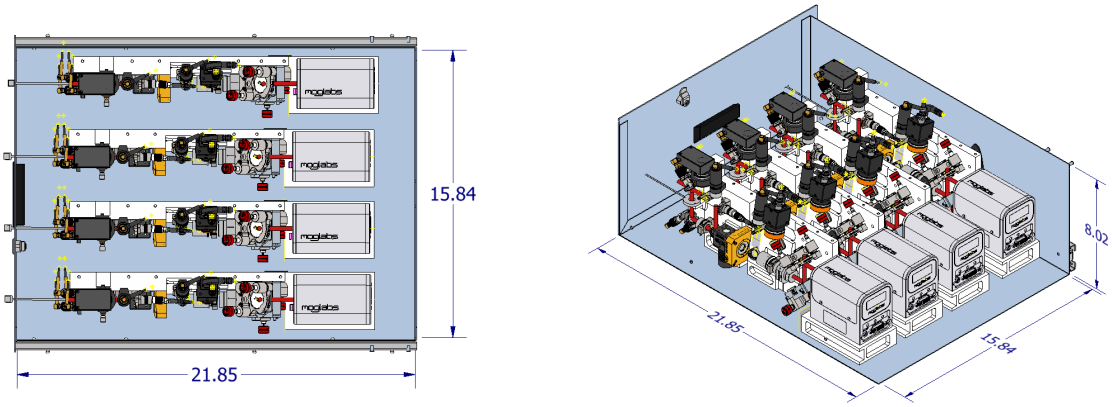

(a) (b)

Figure 4.5: Top and quarter views of the optics rack drawer which will house 4 CW laser heads. This drawer will provide monitoring, coarse power control, and fibre couple all four laser heads.

Chapter 5

Conclusion and Outlook

Before any quantum experiments can be conducted the ions must be sufficiently cold. A detailed study of how cooling is achieved was conducted in Chapter 2. A highly utilitarian framework for performing cooling simulations was presented and code to perform these calculations was written. This investigation centered real world effects like external heating rates, laser linewidths, and laser direction. Considering these effects gave worse performance but much greater confidence experiment would match simulation. Two sub-Doppler cooling methods were simulated, QRSC and EIT cooling, and both were found to achieve suitable temperatures for their intended cooling directions. Special care was paid to cooling direction to acknowledge recent concerns about hot axial modes. Suitable parameters for QRSC were found. Using these parameters all axial modes could be cooled to <0.014 quanta in the presence of 2000q/s external heating. Meanwhile a single parameter set which can cool all of the radial modes simultaneously with EIT cooling was found achieving a final average temperature of <0.17 quanta in the presence of 100q/s external heating. The EIT figures could be further improved by cooling the two radial directions sequentially. In short cooling was thoroughly investigated and suitable laser parameters which produce a "cold enough" system were found.

Having found that the ion system can be cooled a method of controlling the individual quantum state of ions through individually addressable Raman transitions was discussed in Chapter 3. The fundamental limitations on fidelity when addressing ions optically was investigated in detail. These considerations were applied to a FLDW pitch reducing array and found it would not satisfy the optical requirements. Instead a MLA based approach was chosen. Extensive simulations in Zemax showed 10^{-5} intensity cross talk limited by diffraction, an order of magnitude better than contemporary systems. The only barrier to reaching this figure was the accuracy of optic manufacturing. A MLA was manufactured and tested. The surface profile of this optic was found to not match design and a second optic which allows greater error during manufacture was designed.

Chapter 4 discussed the opto-mechanical assembly design philosophy for QuantumION. This approach is painfully aware of real world problems and takes every precaution to make the assemblies robust. The two main principles were to remove points of failure and maintain a tolerance across the assembly through referencing all optical parts relative to

each other. A pegboard for preconditioning and fibre coupling 1107nm light was presented, built in line with the design philosophy.

The near term work which has to be done is characterization of the second MLA following the procedure and methods presented in this thesis. Quantifying pegboard stability is also an outstanding measurement. There is still much work to be done before QuantumION comes online, but the exciting breadth of possibilities afforded by such a system serves as ample motivation.

References

[1] K. Wright et al. "Benchmarking an 11-qubit quantum computer". In: *Nature Communications* 10.1 (2019), pp. 1–6. ISSN: 20411723. DOI: 10.1038/s41467-019-13534-2. arXiv: 1903.08181. URL: http://dx.doi.org/10.1038/s41467-019-13534-2.

[2] J. Zhang et al. "Observation of a many-body dynamical phase transition with a 53-qubit quantum simulator". In: *Nature* 551.7682 (2017), pp. 601–604. ISSN: 14764687. DOI: 10.1038/nature24654. arXiv: 1708.01044.

[3] C. L. Degen, F. Reinhard, and P. Cappellaro. "Quantum sensing". In: *Reviews of Modern Physics* 89.3 (2017), pp. 1–39. ISSN: 15390756. DOI: 10.1103/RevModPhys.89.035002. arXiv: 1611.02427.

[4] T. P. Harty et al. "High-fidelity preparation, gates, memory, and readout of a trapped-ion quantum bit". In: *Physical Review Letters* 113.22 (2014), pp. 2–6. ISSN: 10797114. DOI: 10.1103/PhysRevLett.113.220501. arXiv: 1403.1524.

[5] Ye Wang et al. "Single-qubit quantum memory exceeding ten-minute coherence time". In: *Nature Photonics* 11.10 (2017), pp. 646–650. ISSN: 17494893. DOI: 10.1038/s41566-017-0007-1. arXiv: 1701.04195. URL: http://dx.doi.org/10.1038/s41566-017-0007-1.

[6] C. J. Ballance et al. "High-Fidelity Quantum Logic Gates Using Trapped-Ion Hyperfine Qubits". In: *Physical Review Letters* 117.6 (2016), pp. 1–6. ISSN: 10797114. DOI: 10.1103/PhysRevLett.117.060504. arXiv: 1512.04600.

[7] V. M. Schäfer et al. "Fast quantum logic gates with trapped-ion qubits". In: *Nature* 555.7694 (2018), pp. 75–78. ISSN: 14764687. DOI: 10.1038/nature25737. arXiv: 1709.06952.

[8] Norbert M. Linke et al. "Experimental comparison of two quantum computing architectures". In: *Proceedings of the National Academy of Sciences of the United States of America* 114.13 (2017), pp. 3305–3310. ISSN: 10916490. DOI: 10.1073/pnas.1618020114. arXiv: 1702.01852.

[9] S. Blinov, B. Wu, and C. Monroe. "Comparison of Cloud-Based Ion Trap and Superconducting Quantum Computer Architectures". In: *Preprint* (2021). arXiv: 2102.00371. URL: http://arxiv.org/abs/2102.00371.

[10] Ivan Kassal et al. "Simulating chemistry using quantum computers". In: *Annual Review of Physical Chemistry* 62 (2011), pp. 185–207. ISSN: 0066426X. DOI: 10.1146/annurev-physchem-032210-103512. arXiv: 1007.2648.

[11] Toru Fujimura. "Quantum algorithm for traveling salesman problem by numbering method". In: *Global Journal of Pure and Applied Mathematics* 9.6 (2013), pp. 545–551. ISSN: 09731768.

[12] Peter W. Shor. "Polynomial-time algorithms for prime factorization and discrete logarithms on a quantum computer". In: *SIAM Journal on Computing* 26.5 (1997), pp. 1484–1509. ISSN: 00975397. DOI: 10.1137/S0097539795293172. arXiv: 9508027 [quant-ph].

[13] Charles H Bennett and Gilles Brassard. "Quantum cryptography: Public key distribution and coin tossing". In: *Theoretical Computer Science* 560.(Part 1) (2014), pp. 7–11.

[14] Wlodzimierz Lewandowski and Claudine Thomas. "GPS Time Transfer". In: *Proceedings of the IEEE* 79.7 (1991), pp. 991–1000. ISSN: 15582256. DOI: 10.1109/5.84976.

[15] David J. Griffiths. *Introduction to Quantum Mechanics (2nd Edition)*. 2nd. Pearson Prentice Hall, 2004. ISBN: 0131118927.

[16] D. F.V. James. "Quantum dynamics of cold trapped ions with application to quantum computation". In: *Applied Physics B: Lasers and Optics* 66.2 (1998), pp. 181–190. ISSN: 09462171. DOI: 10.1007/s003400050373. arXiv: 9702053 [quant-ph].

[17] C. Ospelkaus et al. "Microwave quantum logic gates for trapped ions". In: *Nature* 476.7359 (2011), pp. 181–184. ISSN: 00280836. DOI: 10.1038/nature10290. arXiv: 1104.3573.

[18] Brendan Bramman. "Measuring Trapped Ion Qudits". Master's Thesis. University of Waterloo, 2019.

[19] D. Leibfried et al. "Quantum dynamics of single trapped ions". In: *Reviews of Modern Physics* 75.1 (2003), pp. 281–324. ISSN: 00346861. DOI: 10.1103/RevModPhys.75.281.

[20] D.J. Wineland et al. "Optical pumping of stored atomic ions". In: *Annales de Physique* 10.6 (1985), pp. 737–748. ISSN: 0003-4169. DOI: 10.1051/anphys:01985001006073700.

[21] J. I. Cirac and P. Zoller. "Quantum computations with cold trapped ions". In: *Physical Review Letters* 74.20 (1995), pp. 4091–4094. ISSN: 00319007. DOI: 10.1103/PhysRevLett.74.4091.

[22] Klaus Mølmer and Anders Sørensen. "Multiparticle entanglement of hot trapped ions". In: *Physical Review Letters* 82.9 (1999), pp. 1835–1838. ISSN: 10797114. DOI: 10.1103/PhysRevLett.82.1835. arXiv: 9810040 [quant-ph].

[23] John Preskill. "Quantum computing in the NISQ era and beyond". In: *Quantum* 2 (2018), p. 79. ISSN: 2521327X. DOI: 10.22331/q-2018-08-06-79. arXiv: 1801.00862.

[24] Virginia Frey et al. "Programming the full stack of an open-access quantum computer". In: *Preprint* (2021). arXiv: 2106.06549. URL: http://arxiv.org/abs/2106.06549.

[25] James D. Siverns and Qudsia Quraishi. "Ion trap architectures and new directions". In: *Quantum Information Processing* 16.12 (2017), pp. 1–42. ISSN: 15700755. DOI: 10.1007/s11128-017-1760-2. arXiv: 1708.04689.

[26] Peter Maunz. *High Optical Access Trap 2.0 Manual*. Tech. rep. 2016, p. 618951. URL: http://prod.sandia.gov/techlib/access-control.cgi/2016/160796r.pdf.

[27] Dirk Reiß, Albrecht Lindner, and Rainer Blatt. "Cooling of trapped multilevel ions: A numerical analysis". In: *Physical Review A - Atomic, Molecular, and Optical Physics* 54.6 (1996), pp. 5133–5140. ISSN: 10941622. DOI: 10.1103/PhysRevA.54.5133.

[28] H. Sawamura et al. "Optimum parameters for sideband cooling of a $^{40}Ca^{+}$ ion". In: *Applied Physics B: Lasers and Optics* 93.2-3 (2008), pp. 381–388. ISSN: 09462171. DOI: 10.1007/s00340-008-3162-8.

[29] K. Sheridan, W. Lange, and M. Keller. "All-optical ion generation for ion trap loading". In: *Applied Physics B: Lasers and Optics* 104.4 (2011), pp. 755–761. ISSN: 09462171. DOI: 10.1007/s00340-011-4563-7.

[30] Stig Stenholm. "The semiclassical theory of laser cooling". In: *Reviews of Modern Physics* 58.3 (1986), pp. 699–739. ISSN: 00346861. DOI: 10.1103/RevModPhys.58.699.

[31] M. Cetina et al. "Quantum Gates on Individually-Addressed Atomic Qubits Subject to Noisy Transverse Motion". In: *Preprint* (2020). arXiv: 2007.06768. URL: http://arxiv.org/abs/2007.06768.

[32] Adam D. West et al. "Tunable transverse spin–motion coupling for quantum information processing". In: *Quantum Science and Technology* 6.2 (2021). ISSN: 20589565. DOI: 10.1088/2058-9565/abcb5d. arXiv: 2007.10437.

[33] M. Brownnutt et al. "Ion-trap measurements of electric-field noise near surfaces". In: *Reviews of Modern Physics* 87.4 (2015). ISSN: 15390756. DOI: 10.1103/RevModPhys.87.1419. arXiv: 1409.6572.

[34] Laird Nicholas Egan. "Scaling Quantum Computers with Long Chains of Trapped Ions". PhD Thesis. University of Maryland, 2021, pp. 145–146.

[35] Peter Maunz et al. *Characterization of a High-Optical-Access surface trap optimized for quantum information processing*. Tech. rep. Sandia National Laboratories, 2015.

[36] Daniel Lobser et al. *Quantum and Classical Control of Ions in Sandia's HOA Trap*. Tech. rep. Sandia National Lab.(SNL-NM), Albuquerque, NM (United States), 2017.

[37] M. Ivory et al. "Integrated optical addressing of a trapped ytterbium ion". In: *Preprint* (2020). arXiv: 2011.12376. URL: http://arxiv.org/abs/2011.12376.

[38] C. D. Bruzewicz, J. M. Sage, and J. Chiaverini. "Measurement of ion motional heating rates over a range of trap frequencies and temperatures". In: *Physical Review A - Atomic, Molecular, and Optical Physics* 91.4 (2015), pp. 1–6. ISSN: 10941622. DOI: 10.1103/PhysRevA.91.041402. arXiv: 1412.5119.

[39] Daniel Adam Stech. *Quantum and Atom Optics*. 2007, pp. 143–147, 283–293. URL: http://www.opencontent.org/openpub/%0Ahttp://steck.us/teaching.

[40] Claudiu Genes. *Quantum Physics of Light-Matter Interactions*. Max Planck Institute for the Science of Light, 2019. URL: https://www.mpl.mpg.de/fileadmin/user_upload/LectureNotes.pdf.

[41] Christopher J. Foot. *Atomic Physics*. New York: Oxford University Press, 2005, p. 30.

[42] I. Marzoli et al. "Laser cooling of trapped three-level ions: designing two-level systems for sideband cooling". In: *Proceedings of the International Quantum Electronics Conference (IQEC'94)* 49.4 (1994), pp. 179–180.

[43] L. Windholz. "Coherent population trapping in multi-level atomic systems". In: *Physica Scripta T* 95 (2001), pp. 81–91. ISSN: 02811847. DOI: 10.1238/Physica.Topical.095a00081.

[44] E. Arimondo and G. Orriols. "Nonabsorbing atomic coherences by coherent two-photon transitions in a three-level optical pumping". In: *Lettere Al Nuovo Cimento Series 2* 17.10 (1976), pp. 333–338. ISSN: 0375930X. DOI: 10.1007/BF02746514.

[45] Regina Lechner. "Multi-mode cooling techniques for trapped ions". PhD Thesis. Leopold-Franzens-Universität Innsbruck, 2016.

[46] Mu Qiao et al. "Double-EIT Ground-State Cooling of Stationary Two-Dimensional Ion Lattices". In: *Preprint* (2020). arXiv: 2003.10276. URL: http://arxiv.org/abs/2003.10276.

[47] Phillip Kaye, Raymond Laflamme, and Michele Mosca. *An Introduction to Quantum Computing*. Oxford University Press, 2007, p. 69. ISBN: 9780198570004.

[48] Shantanu Debnath. "A Programmable Five Qubit Quantum Computer Using Trapped Atomic Ions". PhD Thesis. University of Maryland, 2016.

[49] D. J. Wineland et al. "Experimental Issues in Coherent Quantum-State Manipulation of Trapped Atomic Ions". In: *Journal of Research of the National Institute of Standards and Technology* 103.3 (1998), pp. 259–328. ISSN: 1044677X. DOI: 10.6028/jres.103.019. arXiv: 9710025 [quant-ph].

[50] Chung-you Shih et al. "Reprogrammable and high-precision holographic optical addressing of trapped ions for scalable quantum control". In: *npj Quantum Information* 7.57 (2021). ISSN: 2056-6387. DOI: 10.1038/s41534-021-00396-0. URL: http://dx.doi.org/10.1038/s41534-021-00396-0.

[51] Krysta M Svore et al. "A flow-map model for analyzing pseudothresholds in fault-tolerant quantum computing". In: *Quantum Information and Computation* 6.3 (2006). arXiv: 0508176v2 [arXiv:quant-ph].

[52] D Leibfried et al. "Laser addressing of individual ions in a linear ion trap ¨". In: 60.1 (1999), pp. 145–148.

[53] Chung-You Shih. "Holographic Optical manipulation of Trapped Ions for Quantum Simulation". Master's Thesis. University of Waterloo, 2019, p. 63.

[54] Noah Greenberg. "Vacuum and Optical Designs for an Open-access Trapped Ion Quantum Processor". Master's Thesis. University of Waterloo, 2020.

[55] John E Greivenkamp. *Field Guide to Geometrical Optics*. SPIE—The International Society for Optical Engineering P.O., 2004. ISBN: 0819452947.

[56] Matthew L. Day et al. "A micro-optical module for multi-wavelength addressing of trapped ions". In: *Quantum Science and Technology* 6.2 (2021). ISSN: 20589565. DOI: 10.1088/2058-9565/abdf38.

[57] Matthew L. Day. "Microfabricated optics for quantum control of trapped ions". PhD Thesis. University of Bristol, 2018.

[58] Zhihao Xiao et al. "An analytically simple and computationally efficient Gaussian beam mode-decomposition approach to classical diffraction theory". In: *Preprint* (2018). arXiv: 1810.06757. URL: http://arxiv.org/abs/1810.06757.

[59] M. Rimmer. "Analysis of Perturbed Lens Systems". In: *Applied Optics* 9.3 (1970), p. 533. ISSN: 0003-6935. DOI: 10.1364/ao.9.000533.

[60] Glendd D. Boreman. *Modulation Transfer Function in Optical and Electro-Optical Systems*. Bellingham, Washington USA: SPIE—The International Society for Optical Engineering, 2001.

[61] I. Pogorelov et al. “Compact Ion-Trap Quantum Computing Demonstrator”. In: *PRX Quantum* 2.2 (2021), p. 1. ISSN: 2331-7019. DOI: 10.1103/prxquantum.2.020343. arXiv: 2101.11390. URL: https://doi.org/10.1103/PRXQuantum.2.020343.

APPENDICES
Appendix A

Spectroscopic Notation

$$n^{2S+1}L_J \tag{A.1}$$

This notation simply takes the quantum numbers used to distinguish different atomic energy levels and maps them to the above notation. The first number is the principle quantum number n. Within a given principle quantum number there are different energy levels distinguished by orbital angular momentum, L, where L=0 is the S shell, L=1 is the P shell, and L=2 is the D shell. The letters keep going but beyond D is not used in this thesis. The superscript is the total spin quantum number, but for $^{133}Ba^{+}$ this number is 2 and does not change therefore is omitted. Finally J is the total angular momentum which could be any valid combination of spin and orbital angular momentum. The different available combinations is why there are two P manifolds and two D manifolds.[15]

Appendix B

Axial and Radial Directions

Throughout this thesis the terms axial and radial direction are used. The axial direction is along the ion direction, and the radial is perpendicular to the ion chain. To fully describe the ion motion there are two radial directions perpendicular to each other. The axial direction necessarily has weaker trapping strength than the radial direction, and confinement along this axis is typically done with only DC fields while a combination of DC and RF are used to trap in the radial direction. An illustrative diagram is shown in Figure B.1. The Sandia trap has additional electrodes which can be used to rotate the radial trapping directions. For cooling to be effective the principle axis must be rotated so both directions make 45° to the trap normal, as shown at the bottom of the two options in the figure.

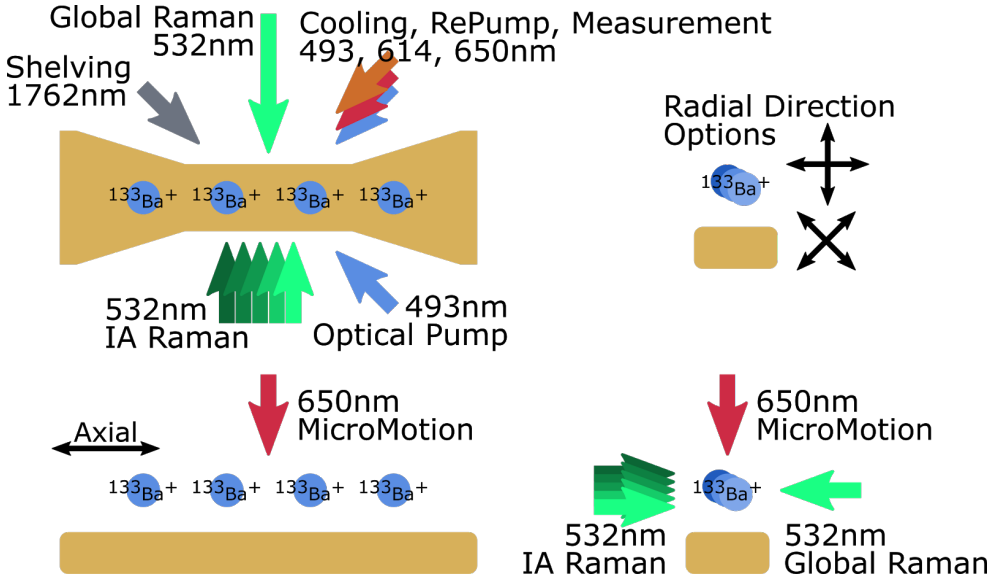

Figure B.1: Sandia HOA 2.0 trap with QuantumION beam geometry and trapping directions annotated.

Appendix C

Trap Frequencies

For Chapter 2 many calculations involved the expected motional mode frequencies. These are key parameters since the motional modes *are* the quantum objects which are being cooled, thus their structure is critical to the efficacy of cooling.

The method presented in the chapter is general and can accommodate any trapping frequency, but to produce useful results accurate input parameters are necessary. The Sandia trap can support a fairly wide range of trapping strengths, however the individual addressing approach discussed in Chapter 3 requires uniform spacing of the ions. This is an advantage of a segmented chip-trap, that there should be enough controls to make the ions nearly equispaced.

Using code developed by Yi Hong Teoh, a fellow MSc student in Professor Islam's Quantum Simulation with Trapped Ions (QITI) group, the expected trapping strengths were converted into motional mode frequencies. This was done for two trapping configurations; harmonic trapping where the confining potential is a quadratic potential, and an-harmonic trapping where the confining potential has a quartic term. Both were optimized for uniform spacing, constrained by the requirements of the individual addressing scheme.

In the harmonic case the average ion spacing was $4.00 \pm 0.4 \mu$m while making use of an an-harmonic potential allowed the spacing to be improved to $4.00 \pm 0.08 \mu$m. In both cases four additional "bumper" ions were added, two on each side, which help make the spacing of the remaining ions more uniform. These are shown in red in the figure below and their spacing does not factor into the optimization. The ion configuration which was used throughout the cooling calculations was the an-harmonic trapping potential.

finally notice that an-harmonic trapping modifies the spacing of the motional modes for all directions. In the axial this is easily understood as a different confining potential leading to different eigenvalues. In the radial direction this is more surprising, however explained by the new equilibrium ion positions. The confining potential remains the same in the radial direction, however the coulomb potential which is a function of the ion positions altered due to the new spacing. This is the source of the changes in the radial direction.

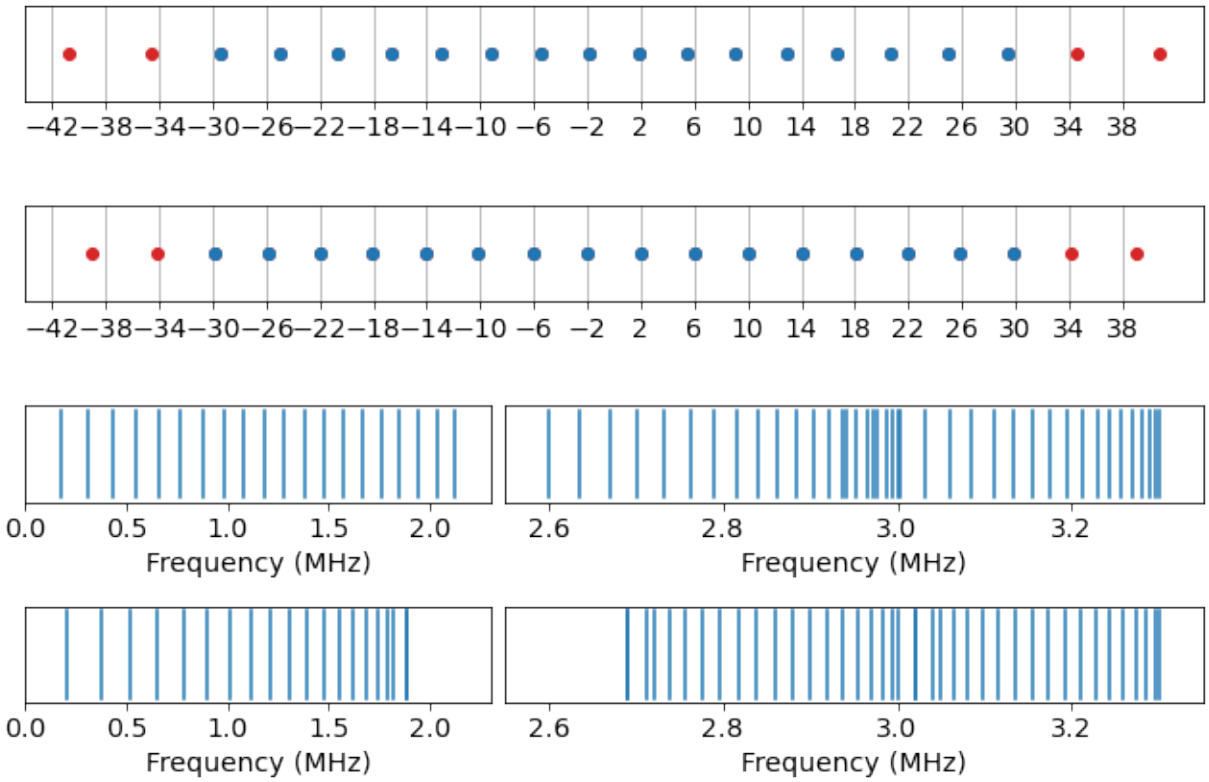

Figure C.1: Expected motional mode frequencies for the QuantumION trap. The very top figure has the result of optimizing for 4μm spacing between ions in a harmonic trap and just below has the same optimization for an an-harmonic trap. Grid lines are spaced by 4μm to aid visualization. Below the two ion position plots are the motional modes plotted as frequencies, again for harmonic and an-harmonic trapping, again the top plot is for harmonic and the bottom is for an-harmonic.

Appendix D

Common Optical Terms

Chapter 3 assumes some knowledge of optical nomenclature. This appendix clarifies these terms with the aid of Figure D.1. The light pattern which is being transmitted through the optical system is called the object, at some point all the rays from the object will come together to re-from the object with scaling dictated by the optical system, this happens at the image. An object will have some height, the maximum height which can be imaged is the field of view, defined by some aperture stop, either a purposeful stop or the diameter of the lenses used. The chief ray runs through the center of the entrance pupil (the first aperture stop), and the marginal ray begins at the optical axis and hits the extremity of the aperture stop. The angle of the marginal ray defines the numerical aperture (NA) of the system. These two rays tend to define the parameters of an optical system. See any introductory optical textbook for more details on these definitions.[55]

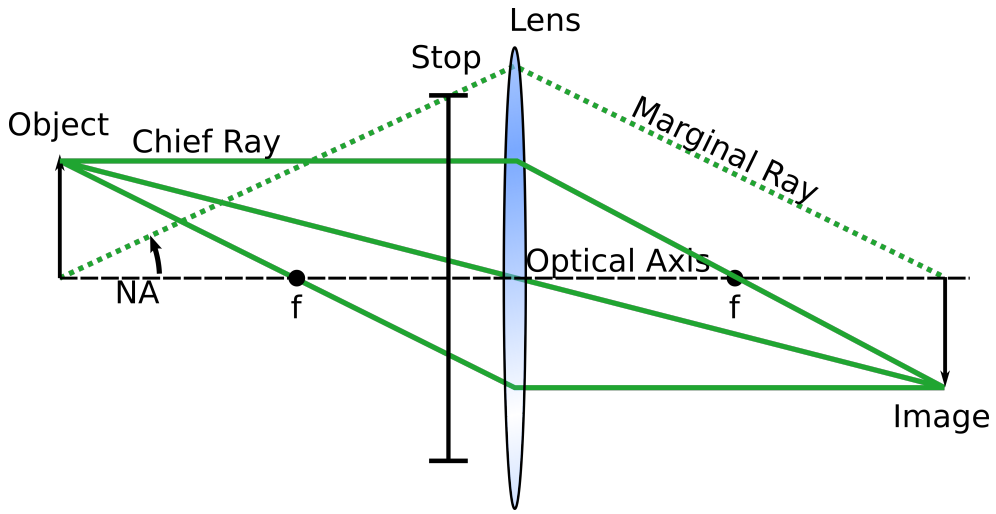

Figure D.1: Diagram to aid understanding of the optical terms used.

Appendix E

IA Telescope Chromatic Performance

The prospect of individual state readout in addition to addressing was briefly considered for the QuantumION system. The unique guided light approach to splitting light in the FLDW wave-guide, as opposed to using a diffractive optical element for example, made state readout achievable with a nominal increase in complexity. For this reason the IA telescope was characterized for chromatic aberrations in addition to the mono-chromatic aberrations. It was later determined that the use of FLDW wave-guides will produce anti-Stokes scattering in the wave-guide at 493nm. Due to the extra time which would be required to engineer around this the idea was shelved.

In Figure E.1 the focal shift as a function of wavelength is plotted without the MLA to the left and with the MLA to the right. As a fortunate coincidence the MLA's chromatic shift acts counter to the shift seen without the MLA leaving a final axial color of 4μm. This would be nearly within the Rayleigh range of the blue laser and so the power loss and cross-talk due to de-focus would be wholly manageable. The lateral color, or change in magnification due to chromatic effects, was also characterized but found to be negligible. For more on chromatic aberrations see the SPIE Field Guide to Geometrical Optics.[55]

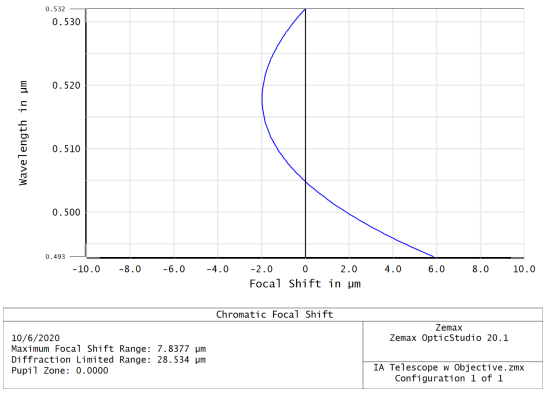

(a) Axial color as a function of wavelength for the ion direction. Performance is of just the IA telescope without the MLA.

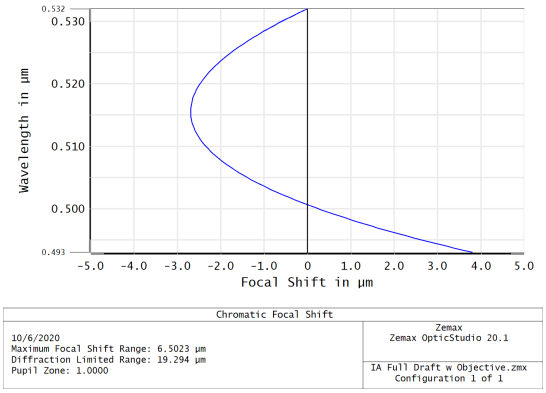

(b) Axial color as a function of wavelength for the ion direction. Performance is of the full system including the MLA.

Figure E.1

Appendix F

MLA Surface Profile In Vertical Direction

Since it was noticed that the optical profiler has a preferred direction after taking the first set of stitched measurements a second set was taken to confirm that the difference is only the collection angle and not the accuracy of the measurement. This view also shows where two lenses meet, and there is a radius as a zero ROC angle is not possible with this method of manufacture. The stitching image method takes a long time on a shared device so only a handful of lenses were re-imaged in this direction.

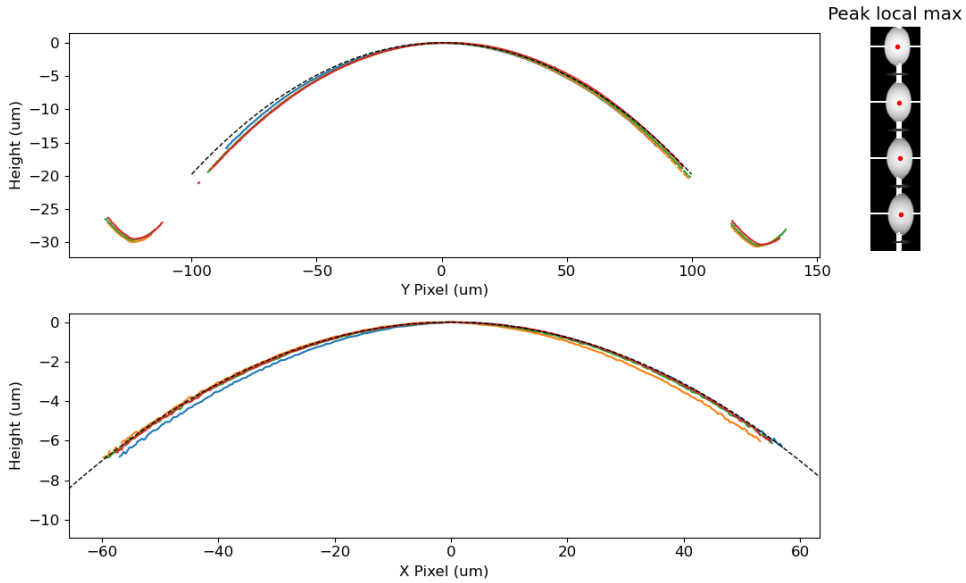

Figure F.1

Appendix G

Preliminary Pegboard Stability Testing

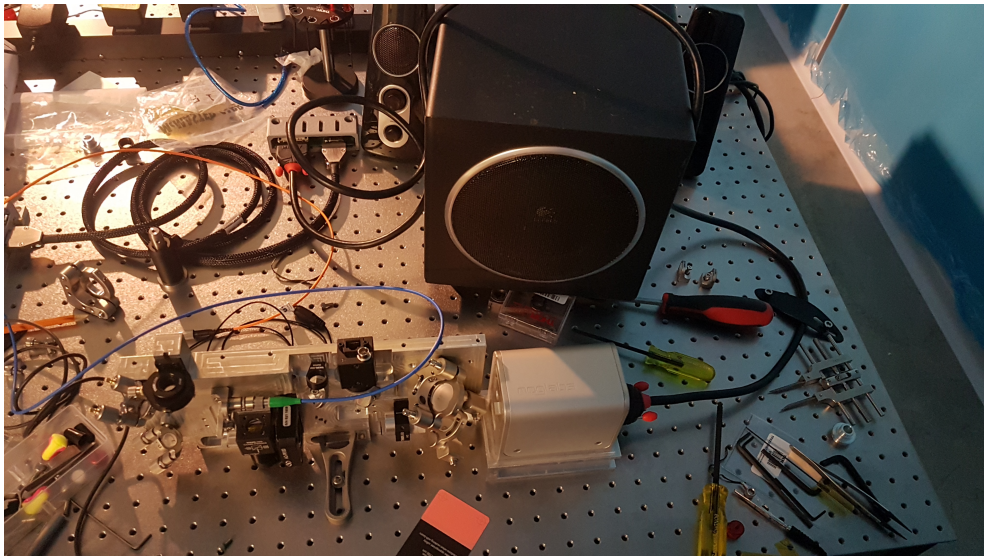

Figure G.1: Acoustic testing setup. Center top of figure is a Logitech Speaker System Z523 placed about 3-4" from the pegboard being tested. The fibre coupling cable is run off to a ThorLabs SM05PD6A photodiode with a ThorLabs AMP130 trans impedance amplifier. The voltage was plotted on a Rigol oscilloscope and data was collected via the USB programming interface.

One major claim of using a pegboard approach to assembling optics is improved robustness against acoustic and temperature fluctuations. These claims need to be quantified and some work to that end has been undertaken however the results are very preliminary. For this reason the results of testing stability are described in this appendix. Further testing is needed to conclusively make any claims, testing in relation to the conventional approach is also needed as a control test.

G.1 Acoustic Testing

To test resilience against acoustic vibrations a large speaker was placed ≈3" from the pegboard and a pure tone was played on the speaker. The speaker volume was around 90dB which is greater than the occupational health and safety exposure limit, so hearing protection was necessary. The tone was played for 10s over which the PD current was monitored and saved as a time series for that frequency. This was repeated for a sweep from 10Hz to 12kHz, and the standard deviation of the voltage for each time series was plotted, seen in Figure G.2.

The result however is that no note-able features are resolved and most of the data looks to be at the noise floor of the photodiode. Knocking directly on the fibre coupler or alignment mirrors does show a response on the photodiode so at some frequency a resonance should be observable but it's clear that this test does not show that.

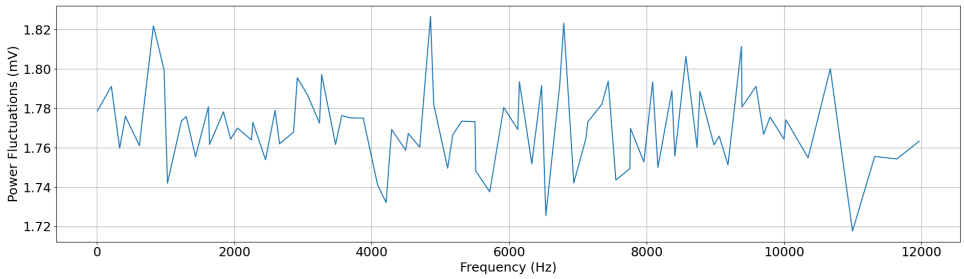

Figure G.2

Further testing is required. Coupling the speaker rigidly to the pegboard would be one way of increasing the amplitude of the oscillations, such strong coupling is not expected in the final configuration but would improve signal. The fibre coupling in this experiment was not fully optimized. The designed for fibre coupler had not arrived in the lab so a coupler for 1550nm light was instead used. Fibre coupling is most sensitive when the laser exactly matches the MFD of the fibre, if the lase beam overfills or under-fills the alignment becomes less sensitive and diminishes the response. Finally this test was done at a safe <5mW laser power, because of COVID scheduling a time with a buddy was difficult and the signal would have benefited from higher laser power to push the photodiode farther away from the noise floor. Correcting for these issues would produce better results and this can be done in the future. For the time being the pegboard is being used in ablation testing and is proving to be robust enough for those experiments!

G.2 Temperature Response

Thermal variations are another primary source of coupling drift. The lab climate was characterized however power monitoring of the pegboard was not monitored throughout the climate monitoring. Temperature stabilized clean room construction was ongoing during construction of the pegboard and required frequent tarping of optics which would have been further complicated by a "live" laser. The performance of the lab in the absence of the clean room is included as a curiosity. Coupling stability in the pegboard between different days was found anecdotally to not be an issue which lends some credibility to the statement that pegboards are robust to temperature variations but true testing is needed.

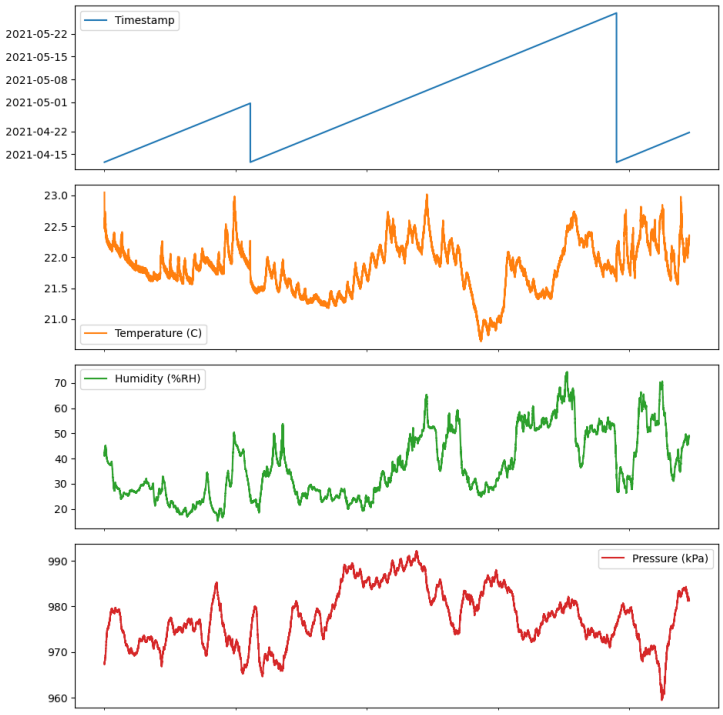

Figure G.3: Lab climate recorded using a custom PCB which polled data from a Sensirion SHT35-DIS and STMicroelectronics LMS22 every 30s. The real time clock meant to keep time even during power outages broke and so every time the circuit was unplugged the date was re-started.